Space Charge Induced Beam Loss on a High Intensity Proton Synchrotron.

Ben Pine
Lady Margaret Hall, Oxford

Thesis submitted in fulfilment of the requirements for the degree of Doctor of Philosophy at the University of Oxford

Trinity Term, 2016

Abstract

High intensity proton synchrotrons provide beams for several types of facility around the world, including spallation neutron sources and high energy physics experiments. The defining feature of these particle accelerators, that of intense beams, is tightly coupled to what limits the intensity, which is the controlled loss of beam particles.

Many different factors contribute to beam loss. Beam will be lost on injection to a synchrotron and may be lost on extraction or in transfer lines. Non-linearities in the accelerator lattice can introduce driving terms for resonant beam behaviour. Collective effects between the beam particles and with the beam environment modify the single particle behaviour considerably.

High intensity loss that occurs in the transverse plane, due to space charge and image fields, was investigated. The rapid cycling synchrotron at the ISIS Spallation Neutron Source in the UK was the focus for all of the work. The ISIS Synchrotron has many particular features which were described. One such feature is the conformal rectangular vacuum vessel, which takes the shape of the design beam envelope with certain modifications. This vacuum vessel has a complex effect on beam image fields.

Numerical tools to study the space charge and image fields at ISIS were created and reported. The tools included two Poisson solvers to study space charge and images which were benchmarked against commercially available algorithms. A two dimensional particle-in-cell tracking code was created using the space charge solvers in combination with either a smooth focusing lattice model or one which generated Twiss matrices. A variety of diagnostic tools were available.

A survey of existing analyses for pencil beams in parallel plate and rectangular geometry was made. Results from the analysis were then compared with two dimensional simulations with round uniform beams in rectangular geometry. Differences and extensions to the analysis were summarised. Coefficients for higher order image terms were defined and tabulated. The two dimensional nature of the image field was discussed and values for the coefficients for certain higher order terms identified in the plane orthogonal to the beam offset.

Solutions for closed orbits produced with single and harmonic kicks at low and high intensity were discussed and simulated. A model was proposed which included the higher order image coefficients produced by the closed orbits. A single particle model was then explored which obtained resonance conditions from the closed orbits and image coefficients. The effect of self-consistent coherent motion on the results was discussed.

Particle-in-cell beam tracking simulations were used to explore the results of this analysis numerically. Image resonances were found and described for a variety of simulation parameters starting with a smooth focusing lattice and uniform density beam, then progressing to more realistic cases including waterbag beams, alternating gradient lattices and conformal vacuum vessels. Image resonances described by the models were reported as were others that needed further explanation. Their possible impact for ISIS was discussed.

New experiments with coasting beams at ISIS were carried out to explore the relationship between tune and beam loss at low intensity. Such experiments are a vital first step to

understanding high intensity behaviour. It was shown that ISIS has existing lattice non-linearities (some known, some unknown) which will need to be taken into account for high intensity experiments and simulations.

Finally this work was put into context by examing specific transverse space charge effects for a proposed ISIS upgrade and including ideas developed throughout the thesis. Estimates were made of the strength of space charge effects and emittance scaling using conventional methods. The particle tracking tools developed for the thesis were then used to study beam behaviour with lattice gradient errors, the effects of closed orbits and changes to the working point. The transverse calculations and simulations suggested that the upgrade was feasible.

Dedication

This thesis has taken a little over 9 years to come into being. During that time I have gone through periods of great joy and great sadness. My grandfather, David Pine, and my step-father, Gordon Molsom, both passed away in the first few years. They were huge figures in my life and I owe them a great debt. My grandfather in particular nurtured my love of science.

My sister, Melissa Yeager, has always been a huge inspiration for me and will always be so. My mother, Christina McEwen, has tirelessly supported and encouraged me, especially when I was filled with doubt.

I could not have finished the thesis without the love and support of my wife, Stephanie. Together we welcomed our daughter, Georgiana, into the world last year. Going through the final draft of the thesis at home, with them popping in and out, has been delightful.

Acknowledgements

There are many people I owe a great debt to in getting to this stage:
John Adams Institute and the Science and Technology Facilities Council.
The ISIS Facility, Accelerator Division and Synchrotron Group.
The Diagnostics Section, Accelerator Physics Section and ISIS Crew.
Dean Adams, John Thomason, Alan Letchford, Tim Nicholls for directly supporting me in many ways.
My supervisors Ken Peach and Chris Warsop.
Ken for providing insight into the Oxford process, sage advice, huge experience and sticking with me well past his retirement.
Chris for his patience, persistence, drive, belief, many, many meetings, copious draft notes, worry, fear and always humour and friendship.

Contents

List of Figures

List of Tables

List of Abbreviations

1RF Fundamental RF system.

2RF 2^{nd} harmonic RF system.

AG Alternating gradient.

BLM Beam loss monitor.

CERN European Organisation for Nuclear Research.

CIC Cloud-in-cell.

CSNS Chinese Spallation Neutron Source.

ESS European Spallation Source.

FEA Finite element analysis.

FFAG Fixed field alternating gradient.

FFT Fast Fourier Transform.

HEDS High energy drift space.

IM Intensity monitor.

JPARC Japan Proton Accelerator Research Complex.

KV Kapchinskij-Vladimirskij distribution.

LEBT Low energy beam transport.

LHC Large Hadron Collider.

MICE Muon Ionization Cooling Experiment.

PIC Particle-in-cell.

ppp Protons per pulse.

pps Pulses per second.

RAL Rutherford Appleton Laboratory.

RCS Rapid cycling synchrotron.

RF Radio frequency.

RFQ Radio frequency quadrupole.

RMS Root mean square.

SNS Spallation Neutron Source.

SRM Storage ring mode.

TS Target station.

WB Waterbag.

Chapter 1

Introduction

Historically, particle accelerators were developed as tools to enable other kinds of science. Whether it was studying atomic structure or anti-matter, surveying the botany of Standard Model particles, generating beams of photons and neutrons, or the discovery of the Higgs Boson and neutrino oscillations, accelerators have allowed vast quantities of new science to be produced.

However particle accelerators are of interest in their own right. They operate at the threshold of challenging scientific and engineering disciplines. They are often pushed by innovation, invention and empirical optimisation to regimes beyond what was predicted in their design. The mathematics that underpins high intensity accelerators does not fully describe their behaviour, as it does not include the self consistent way that particle beams behave.

The existence of stable solutions to beam transmission is taken for granted, but with high intensity beams those solutions are not guaranteed. Fully self consistent analytical solutions for high intensity beams exist for only a handful of cases. These involve solving Maxwell's equations simultaneously with calculation of the beam density distribution or phase fluid, which when combined are known as the Vlasov-Maxwell system of equations. Solutions for other cases are extremely challenging and instead numerical methods must be used to compute how particles move.

This thesis bridges analytical models that exist in one area of accelerator science, that of space charge and images, to particle tracking simulations that are more realistic models of an accelerator. Progress will be reported determining space charge and image contributions to beam loss for high intensity accelerators.

In this introductory chapter, concepts that will be referred to later in the thesis are summarised. In Section 1.1 the rationale for accelerating high intensity beams, the relationship between intensity and beam loss and some of the main causes of beam loss are explained. Section 1.2 goes into the topic of space charge and images in more depth. These phenomena are the subject of much of the rest of the thesis. Particle accelerators that operate at the high intensity frontier, existing and under construction, are introduced and summarised in Section 1.3. Finally, an outline of the rest of the thesis is made in Section 1.4.

High Intensity Accelerators and Beam Loss

Why High Intensity?

High intensity particle beams are useful in a variety of contexts. They are used as drivers for spallation neutron sources. They can serve as the front end for high energy physics facilities such as particle colliders or factories for exotic particles. They have been proposed as drivers for the beams for nuclear transmutation, thorium reactors or heavy ion driven nuclear fusion.

Different kinds of facility can be used to provide high intensity beams. Normal or superconducting linacs and cylcotrons can provide very intense beams that are DC or high repetition rate. Such facilities are ideal for long pulse spallation sources and nuclear facilities. Accumulator rings can take the DC beam from a linac and bunch it to make a sharp pulse on target. Rapid cycling synchrotrons (RCS) are used for short pulse spallation sources and high energy physics facility front ends. Fixed field alternating gradient (FFAG) accelerators can fulfil many of the requirements for high intensity beams, and are an active area of research for new facilities.

Of existing facilities, RCS accelerators are versatile and well tested. They can provide beams of different elements, charge state, intensity and repetition rate, often all from the same machine. The limits of RCS accelerators have not yet been reached and they are the subject of much ongoing research.

High Intensity and Beam Loss

The challenges of providing high intensity beams are nearly all connected with controlling and minimising beam loss. At medium to high particle energies, beam loss causes activation of accelerator components, damaging equipment and limiting hands on maintenance. Uncontrolled beam loss should be kept below $1\,\mathrm{Wm}^{-1}$ to keep activation at acceptable levels. At lower energies, particles are less ionising, so it better to lose particles before they have been accelerated.

Beam loss is controlled through the use of accelerator systems to direct particles exiting the machine on to specially designed collimators, ideally at low energy. Collimation systems localise loss in one well shielded region of the machine, thereby reducing activation and protecting hardware over the rest of the machine. Collimators are made of beam loss tolerant materials such as graphite and copper which are positioned so that they intercept beam particles which are likely to otherwise be lost against the machine aperture. In this way lost particles can be relatively safely channelled away from more sensitive equipment. Carefully optimised use of programmable magnets, RF and diagnostic systems allows most loss to occur at low energy and in the correct locations.

Causes of Beam Loss

There are many processes that can contribute to beam loss in an RCS. Injection of beam from a transfer line into the synchrotron is very complicated whether it is direct transfer of particles or charge exchange injection. For machines with high energy injection, beam loss due to injection processes can be the dominant contributor to activation.

Once the beam is injected it must be captured longitudinally, and this can also provide challenges. Some gains can be made by utilising a beam chopper so that the beam is matched with the RF buckets. If not then some loss at the edges of the buckets is likely.

To a first approximation, synchrotron magnet lattices are designed to be linear. If this is true, the horizontal and vertical planes can be treated separately and therefore beam optics can be easily calculated (ignoring space charge and other high intensity effects). However dipole and quadrupole magnets contain higher order field components which mean that the effective lattice will always be non-linear. In addition, magnet errors and misalignments, as well as higher order multipole magnets used to correct dispersion and chromaticity, all add non-linear fields. Linear field errors mean that the transverse betatron tunes must avoid integer and half integer values. Higher order field errors mean that the tunes must additionally avoid other rational values. Understanding the relationship between magnet and error driving terms and beam resonances that may result from them will be discussed further in the thesis.

Collective effects, including space charge, images and instabilities, can be a major contribution to beam loss. Collective effects can be partially separated into those that occur in the longitudinal and transverse planes. The dominant effect in the transverse plane is space charge; the combined electromagnetic interaction force felt by the beam particles. Beam fields also interact with the vacuum chamber and magnet poles to add electric and magnetic image forces. Space charge and electric image forces are the main topic of this thesis.

Space charge is also encountered longitudinally. However in the longitudinal plane most collective effects are treated via impedances. In addition to space charge there are impedances due to the beam current passing through the vacuum chamber or RF screens, interaction with the RF cavities and other narrowband sources. Instabilities can occur where the beam creates an electron cloud in the beam-pipe which then limits beam transmission and in colliders the two beams can interact, disrupting each other as they pass. There are also transverse instabilities where the longitudinal fields of the beam can lead to unstable motion in the transverse plane.

Finally beam extraction from the synchrotron, which may occur in 1 turn with the use of a fast extraction system, or multiple turns with a septum magnet or resonant extraction can also contribute to beam loss. At extraction the beam will be at full energy and power and such losses must be carefully minimised.

Space Charge and Images

Following Hofmann [1], the electric field $\bar{E}$ and magnetic field $\bar{B}$ inside a continuous, uniform, circular beam of radius a moving at velocity βc in the longitudinal direction with charge density λ are

$$\bar{E}_r = \frac{\lambda}{2\pi\epsilon_0 a^2}\bar{r} \qquad (1.1)$$

$$\bar{B}_\phi = \frac{\beta\lambda}{2\pi\epsilon_0 c a^2}\bar{r} \qquad (1.2)$$

where ϵ_0 is the permittivity of free space, β is the relativistic factor, c is the speed of light in vacuum, $\bar{r}$ is a radial vector and ϕ is the radial angle. These fields are combined in the Lorentz Force Law

$$\bar{F} = e\left(\bar{E} + \bar{v} \times \bar{B}\right) = \frac{e\lambda}{2\pi\epsilon_0 a^2}\left(1 - \beta^2\right)\bar{r} \qquad (1.3)$$

where e is the elementary electric charge. Using the relativistic factor $\gamma = \frac{1}{\sqrt{1-\beta^2}}$, this becomes

$$\bar{F} = \frac{e\lambda}{2\pi\epsilon_0 a^2 \gamma^2}\bar{r}. \qquad (1.4)$$

The combined electromagnetic forces between the particles are inversely dependent on γ^2. The forces approach zero as the particle velocity approaches c. At particle velocities lower than c, these forces oppose the transverse focusing provided by the quadrupole magnets in the accelerator and modify the beam envelope around the accelerator.

A uniform beam distribution has linear space charge forces and leads to a single value for the transverse particle frequencies or tunes. Other beam distributions mean that each particle is affected by different forces, and therefore lead to a spread in the particle tunes.

Space charge forces change the way the beam is affected by lattice driving terms. For realistic beam distributions which add tune spread to the beam, particles will experience different forces and therefore react to driving terms differently. This means that the beam can respond coherently and incoherently to driving terms, which can then lead to collective oscillations or single particle emittance growth respectively. Either of these processes - beating of beam moments or emittance growth - may lead to beam loss if they cause particles to impinge upon the vacuum chamber or collimators. In addition space charge may lead to new driving terms which would not be present otherwise.

Space charge forces also interact with the accelerator components around the beam. Chiefly the vacuum vessel, RF screens inside AC magnets, magnet poles and resonant cavities. Metallic components impose a boundary condition on the electric fields of the beam. The resulting fields can be solved using a superposition of the free space fields and image fields which combine at the boundary to satisfy the boundary condition. When the beam is off-centred there are additional forces which can act as driving terms for new resonances, particularly when the closed orbit of the machine meets specific criteria. In a similar manner, ferromagnetic components impose a boundary condition on the magnetic fields of the beam.

Figure 1.1: The Harwell Campus, including Rutherford Appleton Laboratory and the ISIS Facility

High Intensity Facilities

Neutron Sources

ISIS Spallation Neutron Source

ISIS is a spallation neutron source based at Rutherford Appleton Laboratory (Figures 1.1 and 1.2) in the UK, [2]. It has been operating since 1985. Operation is based on a 50 Hz 800 MeV proton synchrotron which provides 40 pulses per second (pps) to one target station (TS1) and 10 pps to another (TS2). Beam power is a little under 200 kW. The ISIS Facility, in particular the accelerators, will be covered in some depth in Chapter 2.

The main causes of beam loss for ISIS are charge exchange injection of H^- ions, where unstripped, partially stripped and scattered ions and protons are lost (1-2%), the non-adiabatic beam trapping process where another ~ 2 % are lost, transverse space charge and image contributions which increase the beam emittance and a head-tail instability during the acceleration ramp [3]. Both of the latter two loss mechanisms are the subject of ongoing research, some of it reported in this thesis.

Spallation Neutron Source

The Spallation Neutron Source or SNS, [4], operating since 2007, is currently the most intense pulsed spallation neutron source in the world, Figure 1.3. The design is based on a

Figure 1.2: The ISIS Facility

super-conducting linac which accelerates H$^-$ ions to 1 GeV. This beam is injected into an accumulator ring over 1200 turns where it is bunched to produce a sharp pulse of protons that is then sent to the liquid mercury target. The facility operates at 60 Hz and overall beam power is 1.3 MW.

High intensity loss mechanisms have included intra-beam scattering in the linac, causing a significant departure from the design optic, and beam dynamics in the injection region including transport of unstripped and partially stripped H$^-$ to the beam dump as well as stripped electrons [5]. Important design features that have mitigated beam loss are the large transverse aperture, independent injection beam painting and the robust collimation system. Losses have been carefully studied with 3D particle-in-cell (PIC) simulations, including all relevant physics.

Japan Proton Accelerator Research Complex

JPARC, the Japan Proton Accelerator Research Complex [6], is a multi-disciplinary research complex consisting of several combined facilities. A 400 MeV H$^-$ linac injects beam into a 3.2 GeV proton RCS operating at 25 Hz. The facility is capable of beam powers of 1 MW, which is being targeted using a staged approach. About 90% of the beam is sent to the Materials and Life Sciences Facility for neutron and muon production. The remaining 10% is further accelerated to 50 GeV in a larger synchrotron for hadron physics and neutrino studies.

Beam loss contributions at JPARC have been mitigated by careful control of injection painting, control of beta beating due to the injection dipoles and upgrades to the RF systems [7, 8]. Some losses are directly dependent on beam intensity, but have not limited performance. Loss improvements have depended on comparison with detailed simulation models.

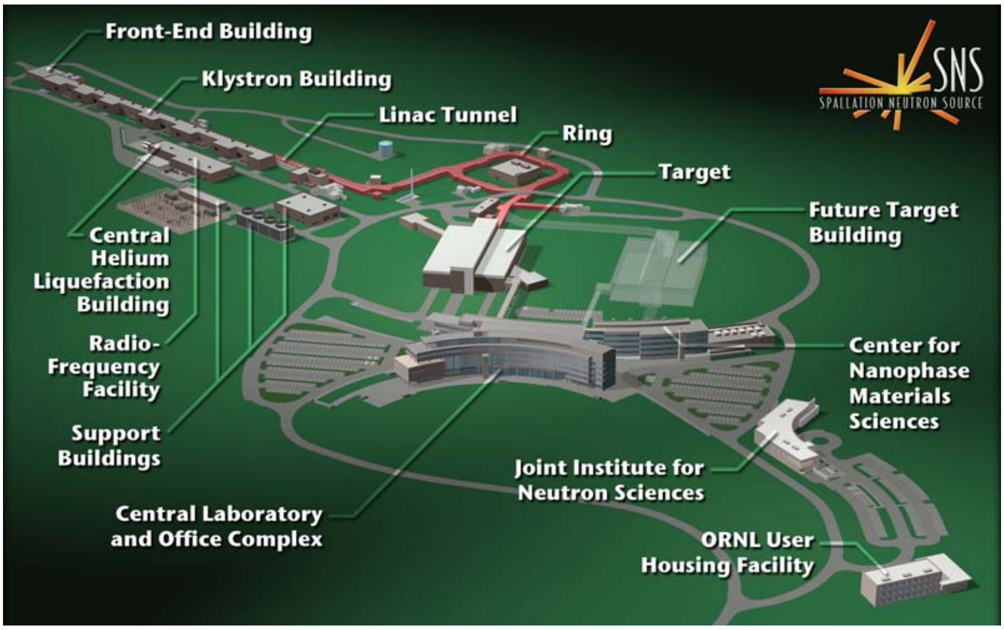

Figure 1.3: Site layout of the Spallation Neutron Source at Oak Ridge National Laboratory, USA. Source: SNS website.

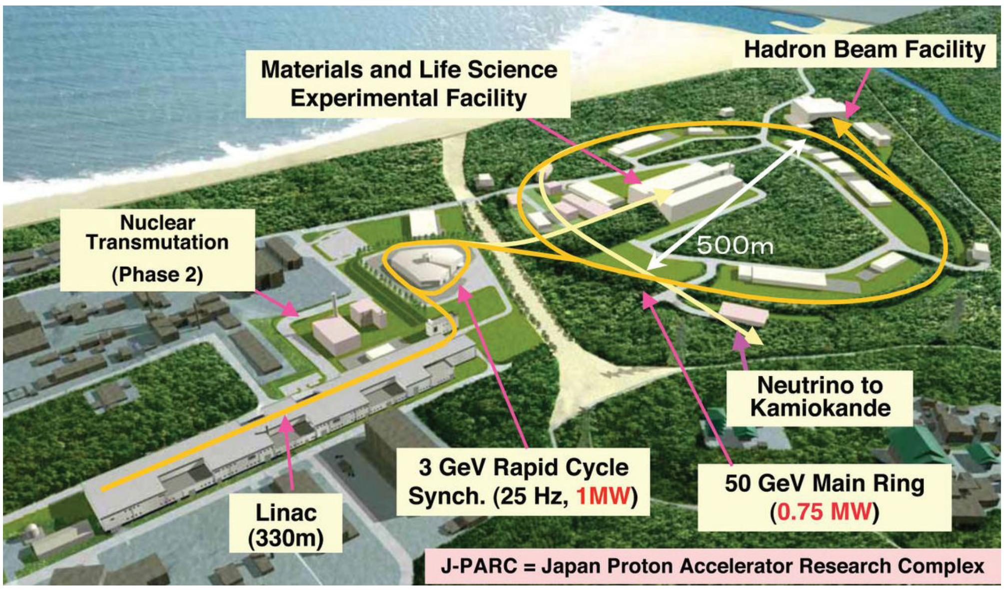

Figure 1.4: Site layout of the JPARC facility in Japan. Source: John Thomason, ISIS.

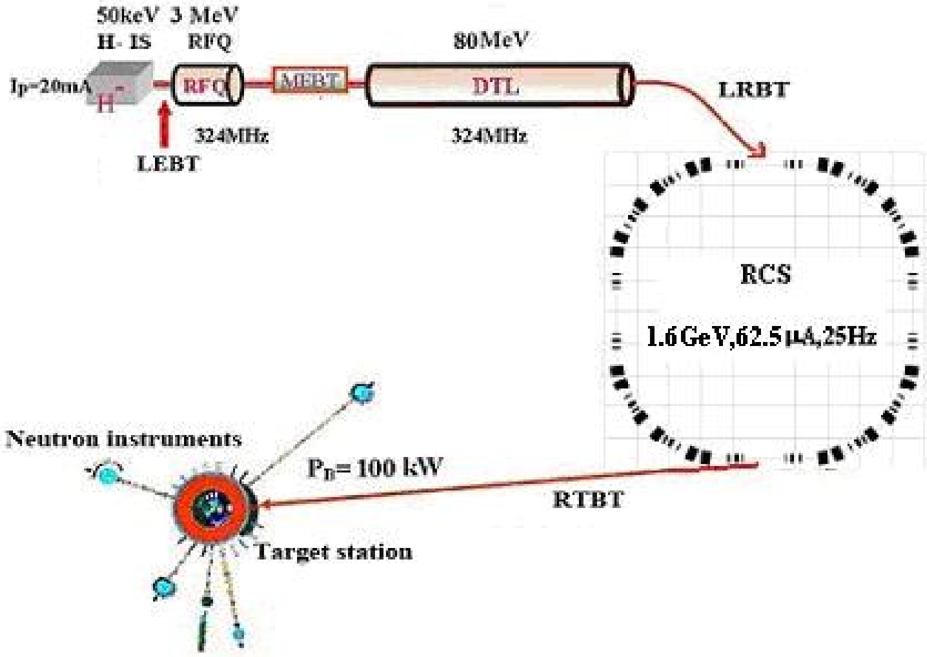

Figure 1.5: Schematic of the Chinese Spallation Neutron Source. Source: CSNS website.

Chinese Spallation Neutron Source

CSNS, the Chinese Spallation Neutron Source [9] is under construction at Dongguan, Guangdong province. Operation is due to begin in 2018. The facility consists of an 80 MeV H^- linac and a 25 Hz 1.6 GeV proton synchrotron which will provide an average beam power of 100 kW. There is the capability to increase the beam power to 0.5 MW by increasing the linac energy and beam intensity.

European Spallation Source

The European Spallation Source, ESS [10], is a long pulse spallation source being constructed in Lund, Sweden, Figure 1.6. It consists of a 2.5 GeV super-conducting proton linac which fires beam directly to target. First neutrons are due to be generated by 2019, with the user programme beginning in 2023 and overall contruction finished in 2025. The overall beam power is 5 MW.

Other Proton Drivers

European Organisation for Nuclear Research

The European Organisation for Nuclear Research, or CERN [11], is the world's largest particle physics laboratory. A chain of accelerators operate together, Figure 1.7, in order to provide beam to many different experiments, most notably the Large Hadron Collider

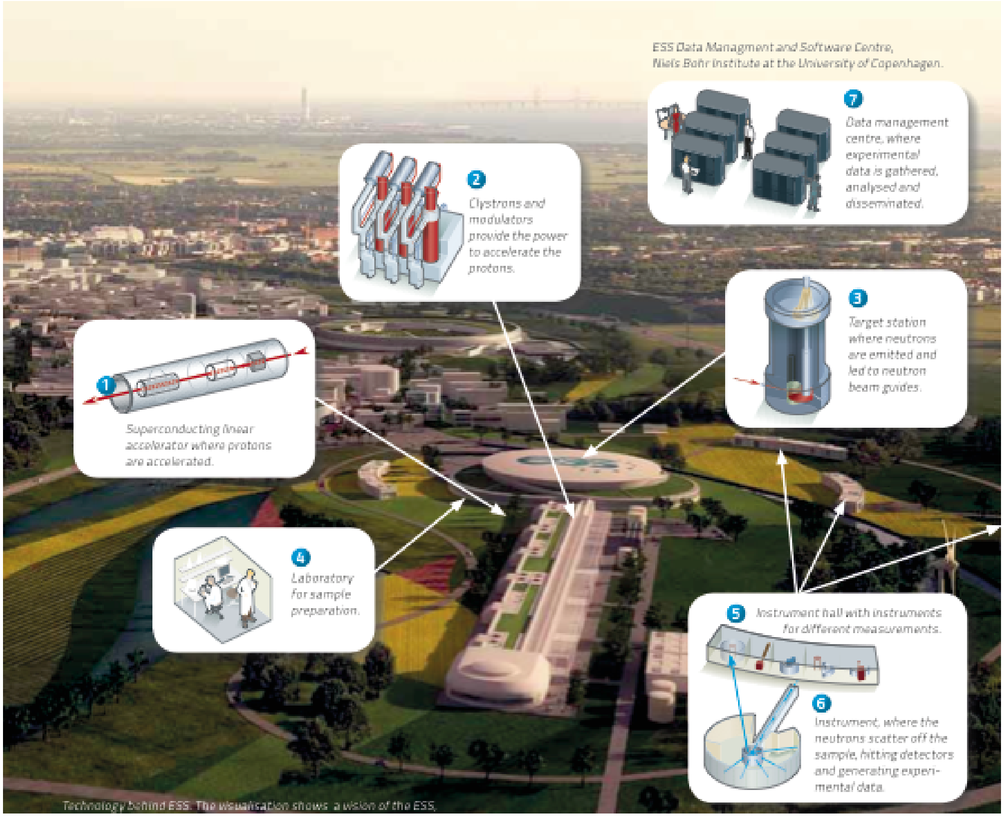

Figure 1.6: European Spallation Source site overview. Source ESS website.

(LHC), the world's highest energy collider. While the LHC operates at a high enough energy for space charge not to be a concern, the Proton Synchrotron Booster (PSB), Proton Synchrotron (PS) and Super Proton Synchrotron (SPS) will have challenging intensity levels for LHC operation at its design luminosity. Of these synchrotrons, the PSB is most similar to ISIS, consisting of 4 stacked rings with an intensity of 1×10^{13} protons per pulse (ppp) per ring.

Paul Scherrer Institute

The high intensity cyclotron at the Paul Scherrer Institute in Switzerland operates at 590 MeV with a continous 2.2 mA extracted beam, leading to a beam power of 1.3 MW. It was commisioned in 1974. It is mainly used as a driver for the spallation neutron source SINQ [12].

FFAGs

Fixed field alternating gradient accelerators are an area of active research for high intensity beams [13]. It is possible they could overcome some of the disadvantages of synchrotrons, while providing the option of higher repetition rates and beam powers. A novel test ring has been proposed at RAL which would include direct proton injection to a scaling 3 - 10 MeV

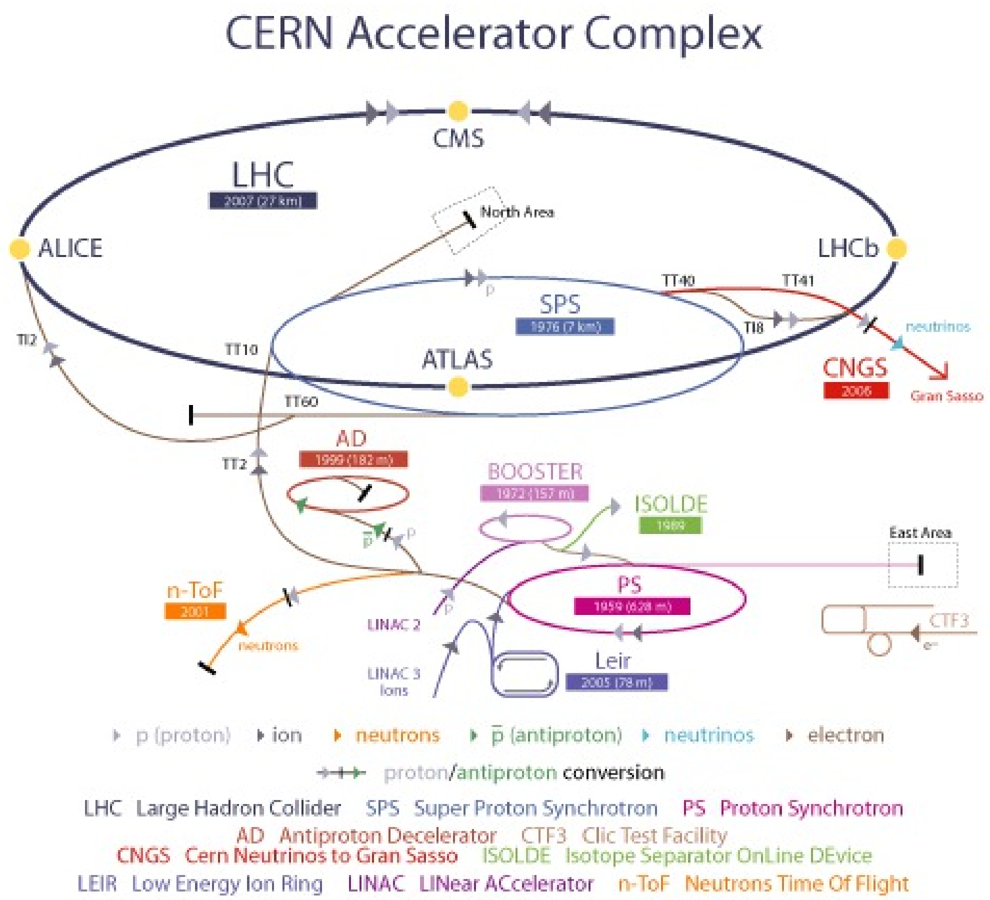

Figure 1.7: Schematic for chain of accelerators at the European Organisation for Nuclear Research Accelerator Complex. Source CERN website.

pumplet FFAG. Designs also exist for an 800 MeV - 3.2 GeV ring which would fit in the ISIS Synchrotron Hall.

Thesis Outline

The thesis is structured as follows.

Chapter 2 is an introduction to the ISIS Facility, especially the accelerators. Special attention is paid to the synchrotron, the focusing lattice, conformal vacuum vessels and to diagnostic devices. A brief introduction is made to the 180 MeV Injection Upgrade.

The simulation tools used throughout the thesis are explained and benchmarked in Chapter 3. Details of models for smooth focusing and alternating gradient lattices, including the conformal vacuum are covered. The space charge solvers, with options for Fast Fourier Transform or Finite Element Analysis based Poisson solvers, are explained with the use of algorithms, and benchmarked.

Chapter 4 begins with a survey of one dimensional image fields for pencil beams in parallel plate apertures. There is a brief look at solutions for rectangular geometry using elliptic functions with centred beams. Then the results of this analysis are compared with the output of simulations of round beams in rectangular geometry apertures. Both centred and off-centred beams are simulated. Modifications to image terms due to the more sophisticated treatment, as well as new image terms in the orthogonal plane, are identified. Results are given in similar form to those identified for one dimensional theory. Ideas for a two dimensional model are briefly explored.

These results are used in Chapter 5, along with the theory of closed orbits, to produce solutions for single particle resonance theory for image terms excited by harmonic closed orbits. Simple simulations are run to compare with the results. The simulations are then made successively more complex with more realistic beams, alternating gradient geometry and conformal vacuum vessels. It is shown that the image terms derived in Chapter 4 can drive beam loss under certain conditions. The simulations also identify other image driven loss mechanisms which are not explained by the theoretical framework constructed in the thesis, and require further research.

Experimental results exploring the relationship between tune and beam loss at low intensity on the ISIS Synchrotron are reported in Chapter 6. New resonances are found and resonance lines identified. These results form the basis for including measured non-linear components from the lattice with simulations. Further work exploring images and other high intensity effects will depend on them.

All of the previous results are incorporated in the transverse dynamics calculations made as part of the 180 MeV Injection Upgrade. This is an upgrade option for ISIS, replacing the aging linac with a new higher energy accelerator. Aspects including space charge tune shift, emittance scaling, simulations for half integer resonance, closed orbits and change of tune on envelope are all considered.

Finally the main results of the thesis are summarised and plans for further work outlined in the conclusion.

Chapter 2

ISIS and the Proposed 180 MeV Injection Upgrade

Introduction

ISIS is the spallation neutron and muon source located at Rutherford Appleton Laboratory (RAL) in the UK [2, 14], as shown in Figures 1.1, 1.2 and 2.1. The facility, which has been operating since 1985, serves an international community of more than 3000 scientists and provides data for around 600 publications per year.

Production of neutron and muon beams relies on a high power particle accelerator, which delivers intense proton beams to appropriate targets. Neutrons are produced by spallation in tungsten targets. The neutrons are cooled until they have the desired energy (0.1 to 10s of eV), then channeled down beam-lines to a number of neutron instruments divided between two target stations. Target Station 1 (TS1) runs at 40 Hz and contains 23 neutron and 4 muon instruments. Target Station 2 runs at 10 Hz and contains another 9 instruments, with 2 more under construction. TS2 is optimised for lower energy, longer wavelength neutrons. Muons are produced with a parasitic, graphite target in TS1 only.

Both neutrons and muons are used by the academic and industrial communities for a variety of materials research, including clean energy, pharmaceuticals, nanotechnology, catalysis and polymers as well as other fundamental physics, chemistry, biology, engineering and archaeology. The facility complements other research carried out at Diamond Light Source and the Central Laser Facility, also located at RAL.

ISIS Neutron Source

ISIS Facility

A multi stage particle accelerator is required to generate beams for ISIS. The beam is first produced in a H^- ion source, accelerated to 665 keV in a radio frequency quadrupole, then

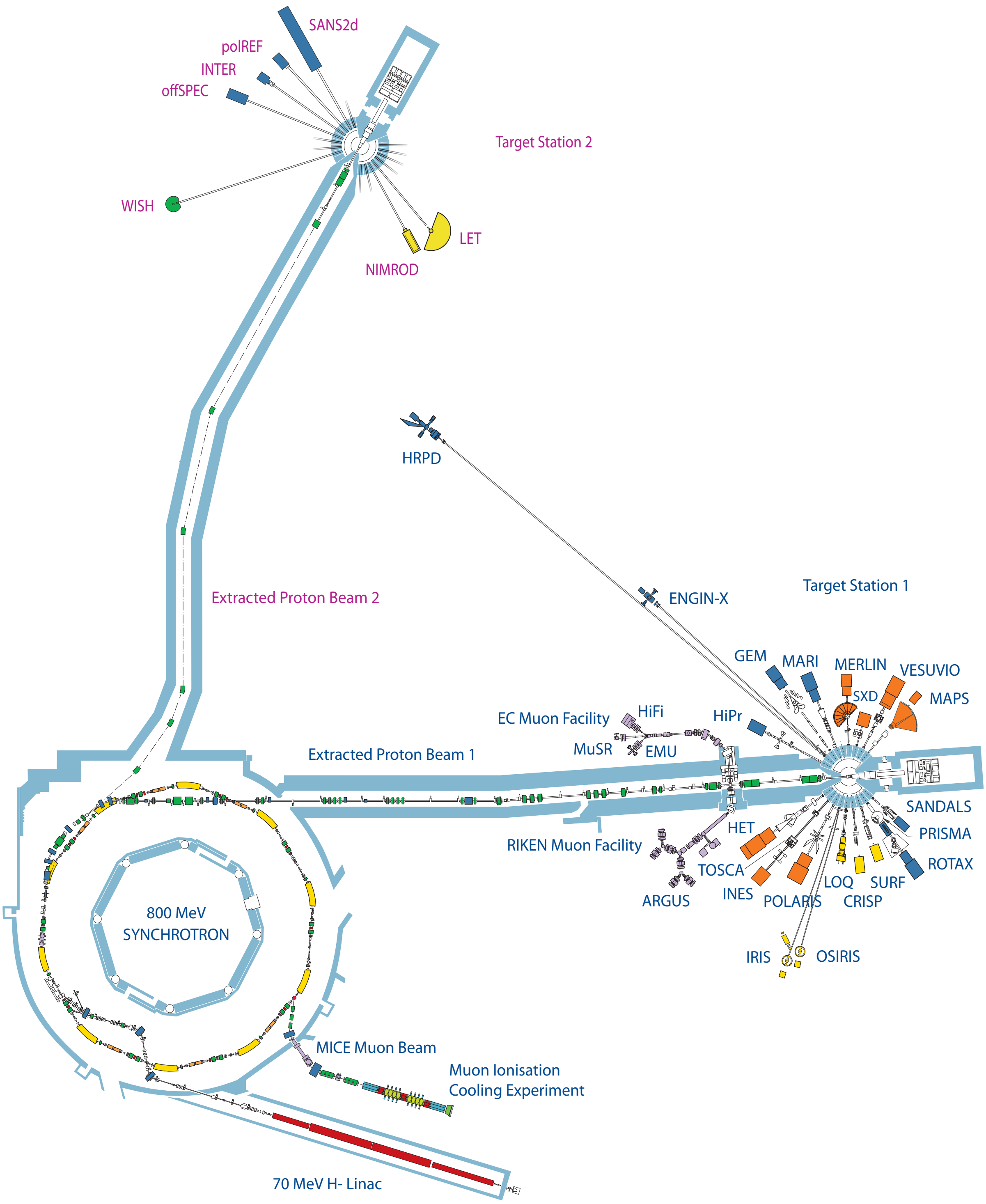

Figure 2.1: Schematic of ISIS Facility.

to 70 MeV in a H$^-$ linac. A high intensity proton beam is accumulated in the synchrotron via multi-turn charge exchange injection. The protons are accelerated in the ring from 70 to 800 MeV and beam is then extracted to one of the target stations. The acceleration cycle takes 20 ms: the machine operates at 50 Hz. ISIS accelerates 3×10^{13} protons-per-pulse (ppp) which equates to a maximum beam current of 240 µA or beam power of 192 kW.

ISIS Injector

Ion Source

Negative hydrogen ions are made in the ion source at the beginning of the linac, see Figure 2.2. H$^-$ ions are generated using a Penning-type ion source [15]. This type of source generates a hydrogen plasma where H$^-$ production is enhanced by caesium. The H$^-$ ions and electrons are extracted from the source, then a 90° sector magnet is used to select the H$^-$ ions. The resulting ions are accelerated to an energy of 35 keV across a DC acceleration gap.

LEBT and RFQ

The H$^-$ ions are then transported through a low energy beam transport (LEBT), Figure 2.2, before being accelerated to 665 keV in a 4 vane radio frequency quadrupole (RFQ) which also provides focusing [16]. The RFQ operates at a frequency of 202.5 MHz. The RFQ also bunches the beam before it passes into the first linac tank.

Linac

The beam is injected directly into the first tank of a 4 tank Alvarez-type linac, Figure 2.2. Tank 1 accelerates to 10 MeV, Tank 2 to 30, 3 to 50 and 4 to 71.44 MeV. All 4 linac tanks operate at 202.5 MHz with the radio frequency (RF) power provided by high power amplifiers. In total the linac delivers a 200 µs pulse of about 22 mA.

HEDS

After the linac, H$^-$ beam is transported through a beam-line or high energy drift space (HEDS). This consists of bending magnets, quadrupoles, diagnostics and a de-bunching cavity, as shown in Figure 2.2. The ions pass into the Synchrotron Hall, shown in schematic form in Figure 2.3, and over the synchrotron, before being injected from the inside radius of the synchrotron.

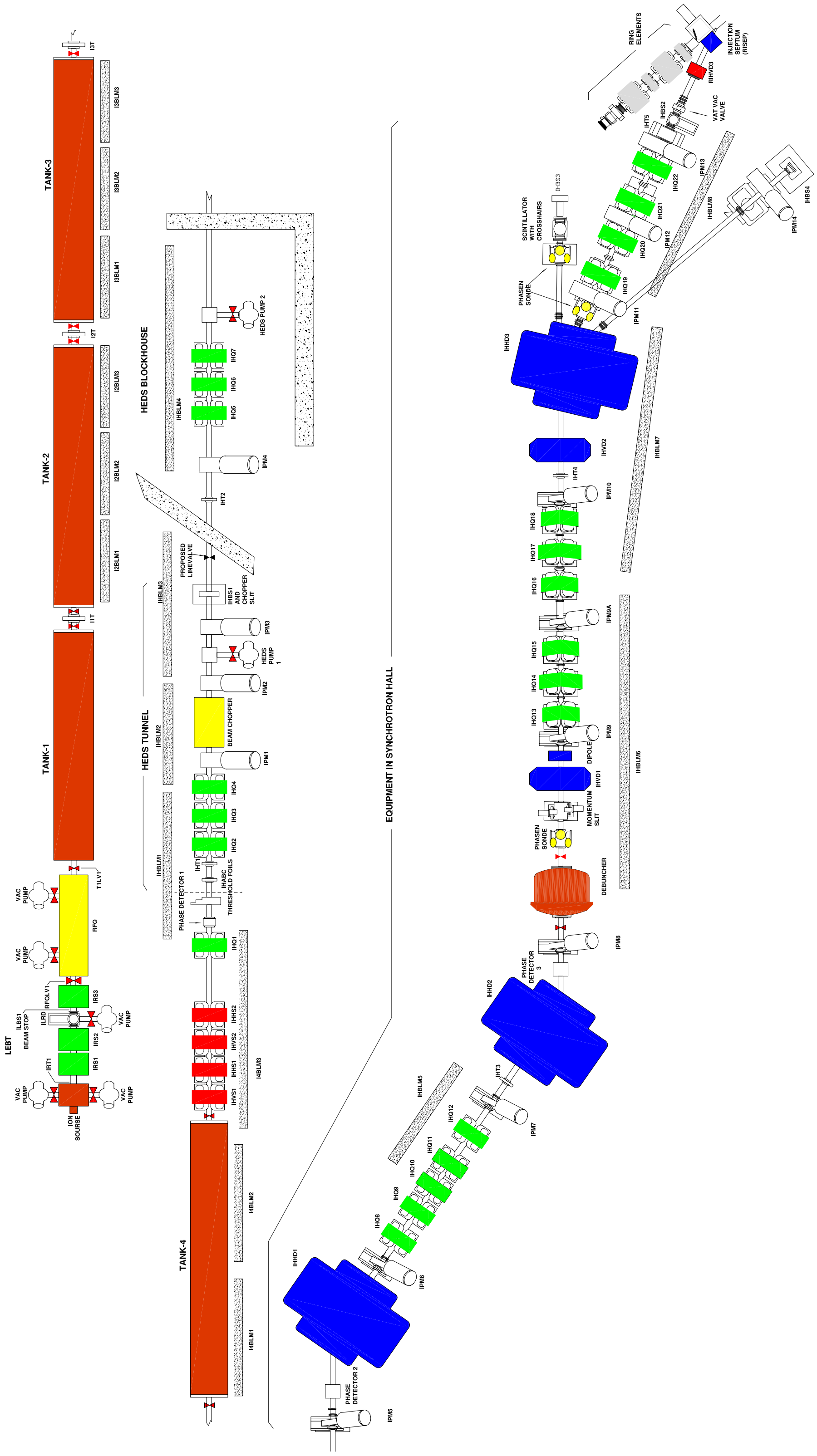

Figure 2.2: Schematic of ISIS Linac and High Energy Drift Space.

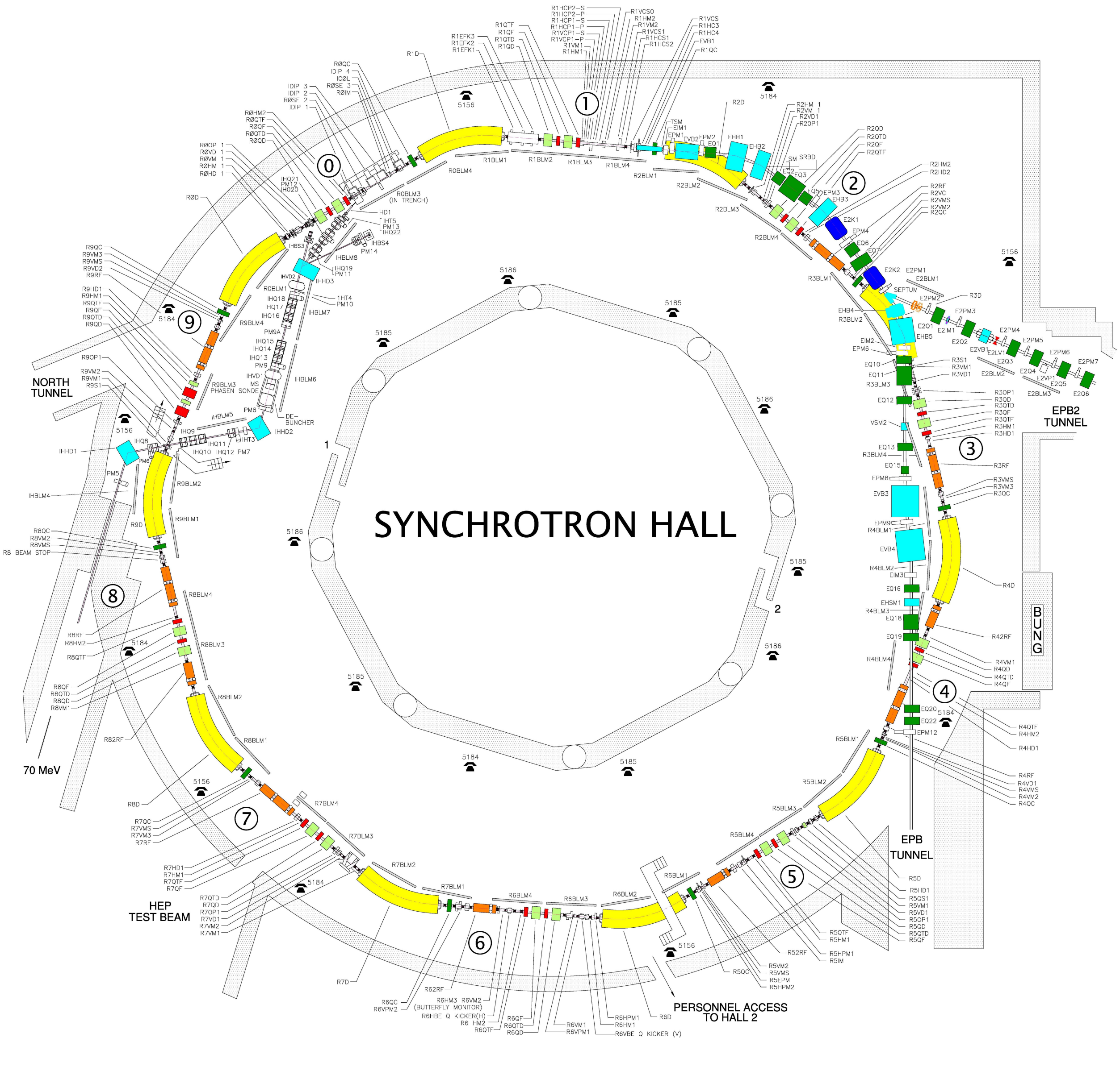

Figure 2.3: Schematic of ISIS Synchrotron.

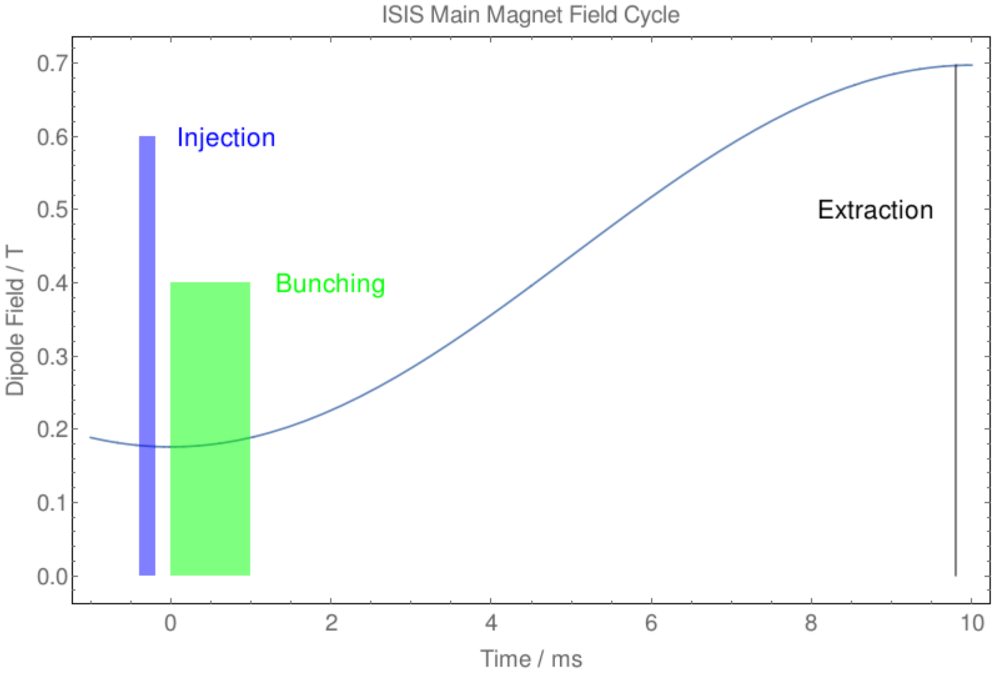

Figure 2.4: ISIS main magnet cycle and features.

ISIS Synchrotron

Machine Cycle Overview

Timing in the synchrotron is relative to the 50 Hz main magnet field, Figure 2.4. Injection starts at −0.4 ms and lasts for about 0.2 ms. Once the beam has been accumulated, RF cavities are used to bunch and then accelerate it. The bunching process occurs over the first millisecond. Beam is then accelerated to 800 MeV and extracted in a single turn at around 9.8 ms. These and other accelerator parameters are listed in Table 2.1.

Injection

The linac beam is injected in the middle of a symmetric 4 magnet horizontal dipole orbit bump (Figure 2.5). The H^- ions pass through a stripping foil as they enter the synchrotron, in the middle of the 4 magnets. The foil strips off both electrons from around 98% of the ions; the remaining unstripped ions and partially stripped hydrogen are directed to beam dumps in the injection straight.

The small injected beam is distributed over the acceptance of the synchrotron in a process known as painting. The objective of painting for a high intensity machine is to minimise the transverse space charge forces the beam experiences as it circulates i.e. to create a smooth distribution which occupies as much of the aperture as possible. Beam is painted horizontally over the course of injection using the falling main magnet field. As the beam is at constant energy the closed orbit moves dispersively away from the stripping foil during injection. Beam is painted vertically with dipole magnets in the HEDS. A hollow beam is

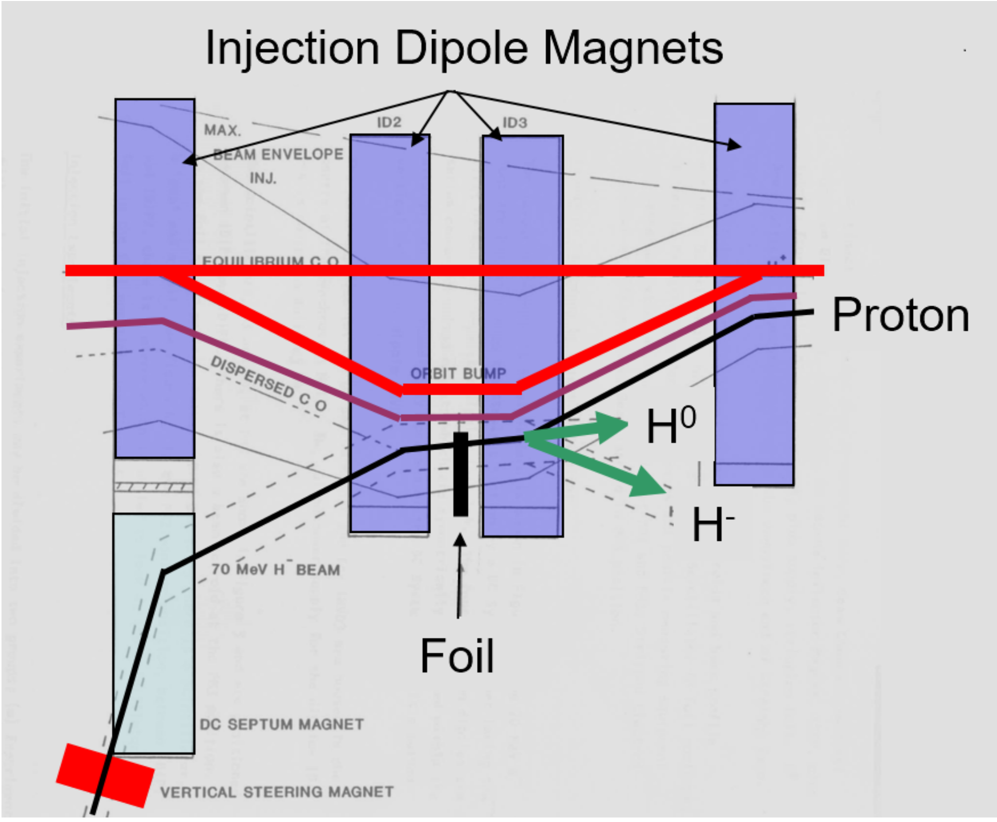

Figure 2.5: Diagram showing H^- injection.

painted both horizontally and vertically, which then fills in during injection as space charge re-distributes the beam. If a low intensity beam is injected the hollow distribution can be clearly seen. Painting is anti-correlated, with beam painted from inside to out horizontally, and top to middle vertically.

Superperiod Structure

The synchrotron is made of 10 superperiods, numbered from 0 - 9 (R0 - R9), as shown in Figure 2.3. Each superperiod is composed of a combined function bending magnet, a short straight, a quadrupole doublet, a long straight and a quadrupole singlet. The magnet strengths and lengths are shown in Table 2.1. These are all driven from the 50 Hz main magnet White circuit, a resonant system which stores magnetic energy in an LC circuit when not driving the magnets. Two sets of trim quadrupoles located at high beta values in the doublet allow independent control of the betatron tunes as well as correction of harmonic errors. The trim quadrupoles and steering magnets can be fully programmed over the acceleration cycle to optimise injection, trapping, acceleration and extraction as well as to minimise beam loss.

Superperiod 0, or R0, is specialised for injection. R1 contains the extraction and collimation systems. R2 - 9 contain the RF systems. Correction dipoles are present at optimised

Table 2.1: Parameter list for ISIS

Parameter	**Symbol**	**ISIS**
Design intensity	N_0	2.3×10^{13} ppp
Repetition frequency	f	50 Hz
Injection energy	E_I	70.44 MeV
Extraction energy	E_F	800 MeV
Gamma transition	γ_T	5.034
Relativistic beta at peak ΔQ	β_0	0.3885
Relativistic gamma at peak ΔQ	γ_0	1.085
Bunching factor at peak ΔQ	B_F	0.35
Machine mean radius	R	26.0 m
Dipole bend radius	ρ	7.0028 m
No. of superperiods		10
Superperiod length		16.3363 m
Dipole length		4.4 m
Dipole sinusoidal AC field	B_{AC}	0.2606 T
Dipole DC field	B_{DC}	0.4364 T
Dipole normalised quadrupole field strength		-0.06875
No. doublet quadrupoles		20
Doublet quadrupole length (Q_D, Q_F)		0.6086, 0.5898 m
Doublet quadrupole normalised field strength (Q_D, Q_F)		$0.6377,\ -0.6377\,\mathrm{m}^{-2}$
No. singlet quadrupoles		10
Singlet quadrupole length		0.314 m
Singlet quadrupole normalised field strength		0.7262
Nominal betatron tune values	Q_h, Q_v	4.31, 3.83
No. trim quadrupoles		20
Trim quadrupole length		0.2034 m
Short straight length		3.106 m
Long straight length		5.938 m
Number of RF cavities (1^{st} harmonic, 2^{nd})		6, 4
Machine acceptance (H, V)	$(A_H,\ A_V)$	540, 430 π mm mrad
Injection scheme		H^- charge exchange
Extraction scheme		Fast, kicked, single turn

positions for closed orbit correction. There are six in the horizontal and seven in the vertical plane. There were originally a family of sextupoles and a family of octupoles in the ring for the correction of dispersion and chromaticity, however only one of each is presently powered, and they are not used in routine operations.

Diagnostics systems are distributed around the injector, ring and extracted proton beamlines. R5 and R6 contain dedicated space for diagnostic devices in the synchrotron. There is an additional parasitic target in R7 for the Muon Ionization Cooling Experiment, or MICE, which generates pions from the ISIS proton beam halo and transports them for further study [17].

ISIS Vacuum Vessel Profile and RF Screens

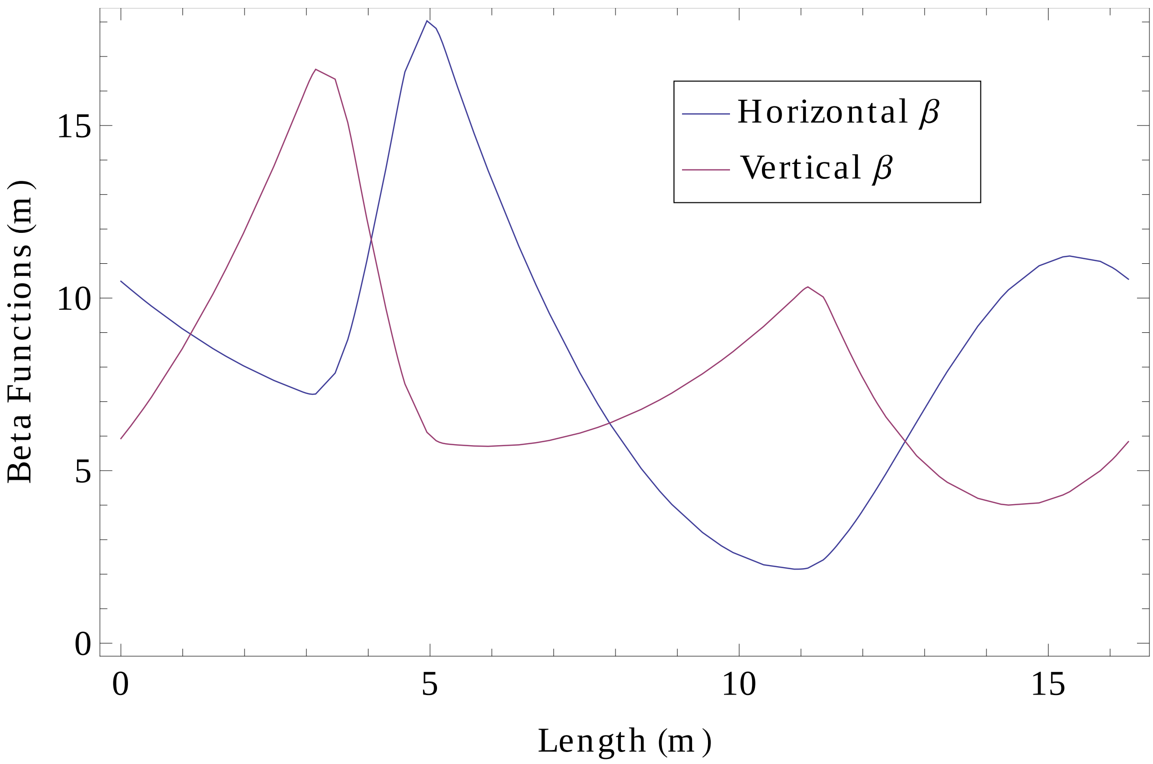

Figure 2.6: Lattice beta functions for one superperiod of the ISIS RCS.

Most of the ISIS vacuum vessels are rectangular and made of stainless steel. In the main dipoles and quadrupoles the vacuum chamber is made of ceramic, with RF screens constructed inside to conduct the beam current, while preventing eddy currents due to the magnetic fields. The optic for one superperiod of the ISIS lattice is displayed in Figure 2.6.

The vacuum vessel was designed to follow the shape of the design beam envelope which the optic describes, with the RF screens maintaining this shape inside the magnets. The precise formula uses the beta functions calculated at high intensity, includes momentum spread and dispersion, and in the horizontal plane there is an additional allowance for variability in the main dipole magnets. The apertures and envelopes are shown in Figure 2.7.

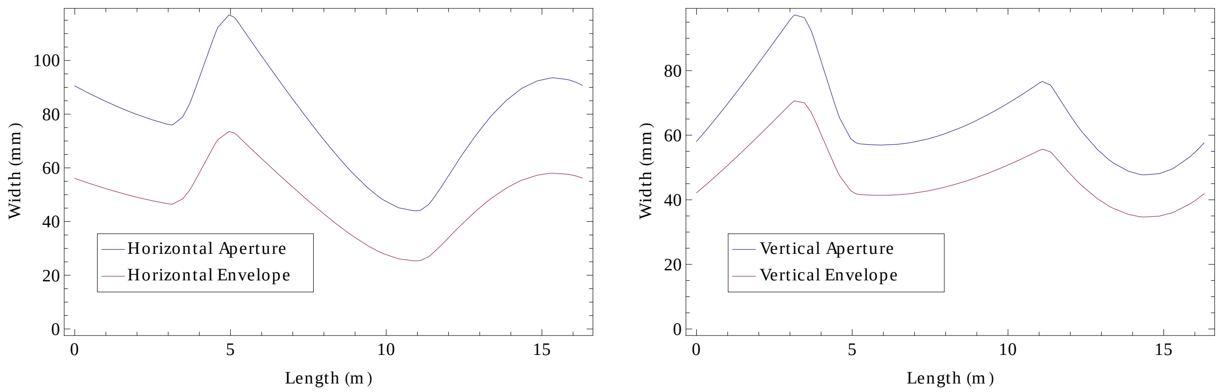

Figure 2.7: Apertures and envelopes for one super period of the ISIS RCS (a) horizontal, (b) vertical.

The vacuum vessel was designed in this way to reduce the transverse reactive space charge impedance and the longitudinal space charge impedance, improve RF containment, reduce external betatron tune spread, create a lower potential for e-p interactions, allow easier escape for electrons to the walls and reduced the number of prompt secondary electrons [18]. The disadvantages are the increased complexity of the vacuum chamber and RF shield as well as the increase in the reactive component of the transverse impedance.

Profiled vacuum vessels also limit the range of tunes accessible in the transverse plane, as changing the betatron tune modifies the beam envelope inside the vacuum vessel. The space charge interaction of the beam with the vacuum vessel, and resonances which can result from it, provide the subject matter for much of this thesis.

RF Systems

There are ten dual-gap, ferrite-loaded RF cavities [19] in the synchrotron. Six of them operate at harmonic number 2 (known as the 1RF cavities), i.e. they run at twice the revolution frequency of the protons, which causes two bunches of protons to form in the ring. Control of the current in the ferrite allows the harmonic frequency of the cavities to be scanned as the protons are accelerated, from 1.3 to 3.1 MHz. The 1RF cavities are located in superperiods 2, 3, 4, 7, 8 and 9. There are also four RF cavities which run at four times the revolution frequency (known as the second harmonic or 2RF cavities) [20]. These are mainly used to shape the bunches of protons as they are formed to reduce non-adiabatic losses. They are located in superperiods 4, 5, 6 and 8. Beam is accelerated in the synchrotron from field minimum at 0 ms to extraction at about 9.8 ms, on the rising edge of the main magnet field, Figure 2.4.

Collimation

Collimation is used to localise beam loss in one well shielded region, thereby reducing uncontrolled loss and activation elsewhere. A collimation system is installed in R1. The collimation system is composed of a number of primary and secondary copper and graphite blocks in

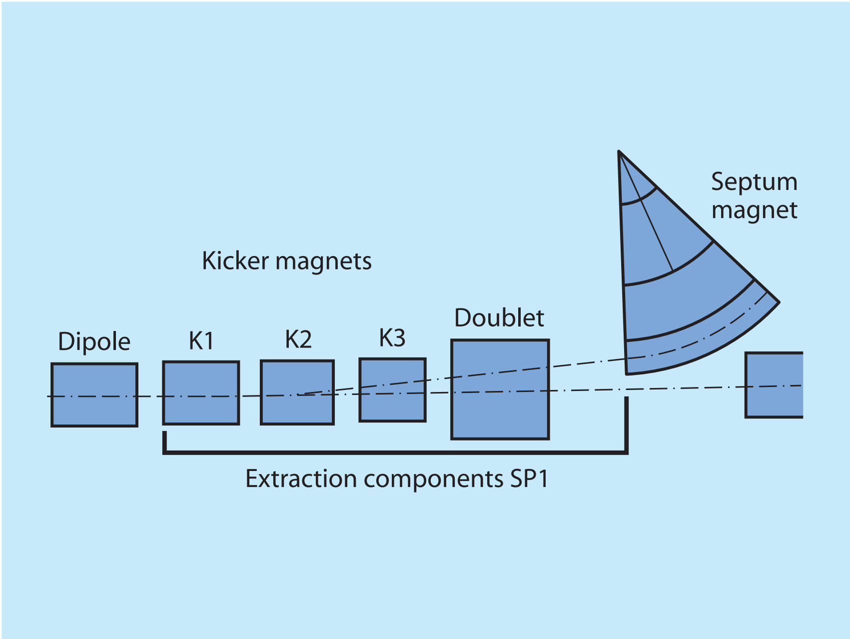

Figure 2.8: Diagram of the ISIS extraction system.

the horizontal and vertical planes. It is designed to deflect and absorb particles safely. One of the principle methods of achieving minimal beam loss is to lose large emittance particles early on in the machine cycle, while they still have a relatively low energy. The primary collimators on ISIS are set at about 85% of the machine acceptance.

Extraction

Beam is extracted vertically from the synchrotron in a single turn using a combination of elements. During the last few milli-seconds of acceleration an orbit bump in R1 is created in the vertical plane using the steering magnets. In normal operation the exact timing of extraction is set by user demand, in order to synchronise with instruments. On the penultimate turn, in between the two bunches, the three extraction kicker magnets are fired, Figure 2.8. These have a single winding for each coil polarity, and are pulsed to 5000 A in less than 200 ns, at a voltage of 35 kV. The kicker magnets divert the beam into the extraction septum magnet. A specialised dipole with one very thin plate below, this bends the beam out of the synchroton altogether and into the extracted proton beam-line, or EPB. From here it can be sent to TS1, TS2, or into a beam-dump within the Synchrotron Hall.

Repetition Rate

The facility repetition rate is 50 Hz. During normal operation, TS1 receives four pulses out of five and TS2 one pulse out of five. It is possible to run each target station independently, though TS2 cannot be run above 10 Hz. It is also possible to pulse at lower rates down to 50 Hz/128.

Diagnostics

A comprehensive set of diagnostics is necessary to operate a high intensity machine and to achieve the required low and controlled levels of beam loss. Most of the diagnostics in the synchrotron need to be non-intrusive. The beam makes about 12000 revolutions during the 10 ms it is in the synchrotron, and any diagnostic would be severely damaged if it were to impinge on the beam. Instead diagnostics detect the beam field or secondary particles.

Loss Monitor

An important diagnostic for operations is the beam loss monitor or BLM. In the synchrotron there are 39 of these 3 m long, argon filled ionisation chambers. These are located around the inside radius of the ring. They give a fast response to beam loss and are part of the machine protection system which can switch off the beam and help prevent damage to the accelerator components. They provide both spatial and temporal information about beam loss. Beam particles that hit the vacuum chamber may activate atomic nuclei as they do so. As these nuclei relax they will produce isotropic neutrons which can be detected in the BLMs. While the absolute calibration of the monitors is imprecise, they are very sensitive and can detect as little as 0.01% of the beam. Similar monitors are also used in the injection line and extracted proton beam-lines.

An additional beam loss detection system uses scintillator based devices. These provide similar information to the BLMs but are smaller and therefore more localised. As they do not contain metallic components they can also be placed inside the iron yoke of fast cycling magnet systems. They are used extensively on ISIS in regions where beam loss has caused damage that was not observed with the BLMs.

Together, the beam loss monitor systems are used to concentrate unavoidable beam loss on the collector systems as early as possible in the machine cycle.

Intensity Monitor

A key part of the machine protection system are the beam intensity monitors. These are inductive toroids around the beam pipe which act as the secondary winding of a transformer, with the beam as the primary. They are easily calibrated and accurate to about 0.1%. They enable the calculation of machine efficiencies for injected, accelerated and extracted beam. There are several in the injection and extraction lines, and two in the synchrotron.

Position Monitor

Beam position monitors are used to detect the beam's position in either the horizontal or vertical plane. They are split-electrode capacitative detectors, which are sensitive to the AC part of the beam field. They do not provide any signal before the beam is bunched. The difference over sum of the two electrodes is directly proportional to the beam position. There is at least one horizontal and one vertical monitor in each superperiod of the synchrotron. The monitors are placed at locations where the betatron motion is large. They have an accuracy of around 0.5 mm.

Residual Gas Ionisation Profile Monitor

The transverse beam profile can be measured using residual gas ionisation profile monitors. There are 5 of these in the synchrotron in R5 and R6. There is also one in the extracted proton beam-line and a modified version in the HEDS. In the imperfect vacuum (10^{-7} Torr) the beam may ionise residual gas ions it encounters. The profile monitor works by directing these ions to a detector with a transverse linear electric field in either the horizontal or vertical plane.

ISIS has both single detector monitors which take a few minutes for a scan as the detector is driven across the aperture - and hence averages many beam pulses, and also multi-channel arrays with 40 detectors which take a single measurement in a few microseconds [21]. There are other profile monitors in the HEDS which use intercepting flying wires, and the EPBs which use harp monitors. As these are both intercepting the machine must be run at low repetition rates when they are used.

Other Diagnostics

There is a beam chopper in the HEDS which can be used to generate short pulses of protons in the synchrotron for diagnostic purposes [22]. There is a betatron Q kicker for measurement of the transverse beam frequencies. Strip-line devices, which can measure beam position and envelope and also correct some beam instabilities, are under development [23]. The synchrotron contains an electron cloud monitor. Though it is slow, the rise of vacuum level in different areas of the accelerator is a distinct warning sign that beam is hitting the aperture nearby.

Pulsed Mode

ISIS has the capability to operate many of the correction elements in a pulsed mode. In this mode operating parameters may be switched between two sets of values: "Normal" and "Experimental". Whilst most 50 Hz pulses are "Normal", selected pulses (at a rate chosen by the user, typically either 1/32 or 1/128 of 50 Hz) have the "Experimental" values. These elements include the trim quadrupoles, steering magnets, RF functions and HEDS chopper. This enables both the investigation of special beam modes during routine operation and also the ability to pulse equipment temporarily at levels that would normally be untenable in routine operation.

Storage Ring Mode

The RF cavities can be turned off (1RF) or off-tune (2RF) to allow beam to be injected into the ring and stored for a short time. Storage ring mode (SRM) entails running the main magnets at constant currents and turning off the extraction system. It is also possible to run the RF systems at a constant frequency and so bunch but not accelerate the protons.

180 MeV Injection Upgrade for ISIS

ISIS Upgrade Scenarios

There are several options open to upgrade the accelerators at ISIS in order to provide more capability and capacity at the facility. These include upgrades to the linac which would reduce space charge in the synchrotron and enable a higher beam intensity to be accumulated; ISIS could be upgraded incrementally including modifications to the injector and synchrotron and still providing beam to both existing target stations as well as a new one. Alternatively a new stand-alone facility could be built whose performance exceeds that of the current facility.

These different upgrade paths are constrained financially, by conflict with ISIS operations and by a desire to keep the existing neutron and high intensity proton expertise in the UK. The cheapest option is to install new equipment in the existing ISIS buildings, though this must be done incrementally in order to minimise downtime for the ISIS instruments.

Overview

There are several designs for a replacement for the ISIS Linac [24], parts of which are over 60 years old. The design which has been considered most comprehensively (with regards to the synchrotron) is a 180 MeV normal-conducting linac which would be built next to the existing linac and thus minimise downtime [25]. Chapter 7 of this thesis focuses on the consequences the 180 MeV option would have for transverse dynamics in the ISIS Synchrotron. In particular the effect the upgrade would have on space charge, emittance scaling, half integer resonance, closed orbit driven image resonances and the location of the working point will be discussed.

Designs of appropriate 180 MeV linacs are well established and for the study that of JPARC was assumed [26]. The design would incorporate beam chopping to place beam into the synchrotron buckets for lossless RF trapping. During construction the existing ISIS Linac could continue to operate thus minimising facility downtime. Work has focused on several key areas for the upgrade: replacement of the ISIS injection straight to accommodate

180 MeV beams, space charge benefits and issues for the upgrade, longitudinal and transverse dynamics, 3D dynamics, diagnostics and instability control, RF and beam loss modelling.

Injection Straight

The injection straight, including the injection dipoles, septum, beam dumps and stripping foil, would all need to be replaced for operation at 180 MeV. The new linac would inject from the outside radius of the machine using an asymmetric, programmable 4 magnet bump. Injection painting would be provided by the variation of the bump magnets, control of the vertical beam angle at the foil spot, the changing main magnet field in the synchrotron and manipulation of the linac energy and beam chopping.

An outline physics design has been completed [27]. This includes new OPERA [28] models for the septum and dipoles which meet the required tolerances and show the paths of unstripped and partially stripped injected beam going to their respective beam dumps.

The carbon stripping foil required for 180 MeV injection has been studied extensively, including modelling in ANSYS and FLUKA. Expected stripping rates versus thickness and foil material, as well as predicted foil temperatures have been calculated [29].

Beam Dynamics

Detailed longitudinal simulations have been carried out optimising different injection schemes including linac energy ramping, beam chopping and the injection point relative to the main magnet field minimum (before, symmetric or after) [30]. These simulations have included calculations of the Keil-Schnell-Boussard stability criterion and minimised it for various designs.

Studies of transverse dynamics have focused on space charge, emittance scaling, half integer resonance, closed orbit driven image resonances and the location of the working point, and are dealt with elsewhere in this thesis (Chapter 7).

The upgrade dynamics have also been modelled in detail [31] with the 3D beam dynamics code ORBIT [32]. This has been used to study the complicated 3D nature of the injection painting process, in close collaboration with the injection straight design and longitudinal dynamics teams. Loss assessments from the initial simulations look promising, keeping overall beam loss below 0.1% and controlling that loss on the collector systems.

Other Key Topics

The resistive-wall head-tail instability is a known loss mechanism on ISIS, and may need to be mitigated for the upgrade. An R&D programme is underway to understand and control the instability [33]. Design and commissioning of a damper system using the strip line kickers / monitors (2.2.4) is in progress.

Upgrading of the RF valves in the synchrotron to TH558 valves [34], in addition to many upgrades and improvements to the low level RF systems, should address problems with beam loading at the higher circulating currents of the upgrade.

Chapter Summary

An overview of the ISIS Facility, in particular the accelerators which provide beam to its targets, was presented. Focus was mainly placed on the synchrotron and transverse plane, as that was relevant for this thesis. The diagnostic systems were also reported in some detail, as they will be referred to in Chapter 6.

A short overview of the 180 MeV Injection Upgrade for ISIS was presented. This forms necessary background for Chapter 7 where the transverse dynamics considerations for the upgrade will be considered.

Chapter 3

Simulations for Image Field Analysis and Investigation of 2D Beams in Smooth Focusing and Alternating Gradient Lattices

Introduction

Research in the thesis is supported by simulations in a variety of different ways. Theoretical ideas have been tested using simple models. Extensions to theory have been explored using more sophisticated models. Simulations have been used to perform experiments which bring insight into the behaviour of high intensity accelerators. Finally simulations have been used to test upgrade ideas, and select features and constraints on new accelerators.

A versatile, modifiable simulation tool has been created which can generate 2D space charge and image fields from particle distributions and also track particles through these fields as well as accelerator lattice elements. This tool, Set, has been used to study space charge, image fields and beam evolution with driving terms and resonances. The code is capable of representing the conformal vacuum vessel used on ISIS. This chapter describes some of the code's features.

While other more sophisticated tracking codes, such as ORBIT [32] exist, it has proved particularly useful to have an in-house code that can be reconfigured for different situations, as well as expanded with new tools as required.

Model

Set can track particles through either a smooth focusing model, where the beta functions and tunes are constant around the circumference of the simulated accelerator, or an alternating gradient (AG) model. If AG the lattice information can be read in directly from a file or from MAD output [35].

The 2D tracking code Set will be described in this section. This code was developed with the purpose of tracking particles within the ISIS conformal rectangular vacuum vessel, including space charge and the image forces generated from the beam. The code is written in C++. Its main components are classes describing the bunch, lattice and space charge calculations.

The Bunch class is responsible for keeping track of particles including coordinates, momenta and beam loss. It also records individual particle tunes and can print the bunch or a subset.

From the lattice input an array of transfer matrices is constructed. Twiss parameters and the single particle tunes are generated as well. The vacuum vessel can be set to a constant boundary, using aperture values read in a from file, or a conformal vessel generated from the lattice.

The Poisson class contains functions for binning the bunch into a discrete distribution with boundary conditions set either in the input file or by the lattice elements. A Fourier transform is then performed on the charge distribution, the potential is calculated and then transformed back. Other functions calculate the fields and transform the fields into particle velocities. If the smooth focusing option is enabled this class also moves the particles. There is an alternative class, Mesh, which solves for the potentials using finite element analysis, or FEA, but is otherwise comparable to the Fast Fourier Transform (FFT) based solver.

There are additional classes for input and for generating RMS beam moments from the bunch information.

Exploring Higher Order Image Coefficients

In Chapter 4, values for image coefficients are calculated for pencil beams in parallel plate geometry, and in rectangular geometry for limited cases. Simulations are used to explore how these coefficients change using fields generated with 2D round beams in rectangular geometry. Values are obtained for them for parameters comparable to those used in ISIS.

Space charge forces can be calculated for the particles using two solvers. One is an FFT based Poisson solver and the other is an FEA based solver. Both at present solve for a rectangular conducting boundary at ground potential, which is similar to the ISIS beam environment. The FFT solver is faster. The FEA solver works completely differently, and so is a good test of the FFT solver, and is also potentially more versatile. In the future it will be possible to develop it to use with other geometries. It will also be possible to make it faster using a direct matrix solver rather than the current method.

Poisson Solver

The main Poisson solver is based on a sine FFT solution for the potential. Macro-particle charge is binned to a grid bounded by the vacuum vessel, where the potential is zero. This can either be a brute force (nearest grid point) or a cloud-in-cell (CIC) model which distributes charge to the nearest 4 grid points. The charge distribution is then transformed to frequency space using an FFT library (FFTW - Fastest Fourier Transform in the West [36]), which uses a comprehensive and advanced suite of algorithms to provide fast solutions for a variety of FFT problems.

In frequency space the charge distribution is converted to a potential using an algorithm adapted from Numerical Recipes for C++ [37]. The algorithm is for a 2D partial differential equation with boundary conditions solver that has been adapted to use with a sine FFT. In outline the Poisson algorithm takes the form:

```
Bin macro-particles to grid - this initialises the array "potential"
Sine FFT of charge distribution
for (i=0; i<M; ++i)
        for (j=0; j<N; ++j) {
                ifrac=i/M;
                jfrac=j/N;
                denom=(2.0 * (cos(π * ifrac) + cos(π * jfrac) - 2.0));
                if (denom == 0) potential[i, j] = 0;
                else potential[i, j] = -potential[i, j]/denom;
        }
Inverse Sine FFT of potential distribution
```

In the algorithm i and j are integers used to iterate through the charge/potential array *potential*. N and M are the horizontal and vertical mesh sizes respectively.

The charge of each macro-particle, *ppmacro*, is calculated using the macro-particle intensity I_M and space charge perveance K_{SC} [38]:

$$I_M = \frac{I}{N_0 C} \tag{3.1}$$

$$K_{SC} = \frac{q^2 I_M}{\beta^2 \gamma^3 \epsilon_0 M_p c^2}, \tag{3.2}$$

where I is the beam intensity, N_0 is the number of macro-particles, C is the ring circumference, q is the particle charge, β and γ are the usual relativistic factors, ϵ_0 is the permittivity of free space, M_p is the proton mass in kg and c is the speed of light.

This value for the macroparticle charge is correct for space charge, but not for the image field. The Poisson solver as written here provides the correct boundary for the electric field, but not the magnetic field. It therefore underestimates the effects of images. At the particle energies simulated in the thesis this will be a small effect. This will be corrected in a future version of the code. The results contained in the thesis are the best available with the methodology developed so far.

Along with factors to convert to mm mrad, from time to longitudinal coordinate and factors left over from the Poisson solver

$$ppmacro = \frac{10^3 \times K_{SC}}{4NM}. \quad (3.3)$$

Horizontal and vertical electric fields can then be calculated by taking differences across mesh cells. Forces are applied to particles in a manner symmetrical to charge deposition - either crude or CIC, this avoids introducing a "self-force" where the particle accelerates itself [39]. The particle angle is then updated:

$$\begin{aligned} x_p &= x_p + E_x s \times 10^3 \\ y_p &= y_p + E_x s \times 10^3 \end{aligned} \quad (3.4)$$

Where x_p and y_p are the angle (conjugate momenta) of the particle, E_x and E_y are the interpolated fields at the particle position, s is the length of the element being traversed and 10^3 is applied to convert to mrad.

The Poisson class can also print the potentials, raw fields and interpolated fields.

FEA Solver

The finite element analysis solver is similar to the FFT solver in that it discretises the charge distribution to a grid, but the grid and method of solution are very different, providing an independent tool for space charge analysis. It is also possible to solve for complicated boundaries with the FEA solver. The FEA solver used in Set was produced using established methods [40]. The FEA solver uses a triangular mesh to collect the particle charge, as shown in Figure 3.1 (a). The triangles or elements contain the material properties and charge, Figure 3.1 (b), while the vertices store mesh information and the potential, Figure 3.1 (c).

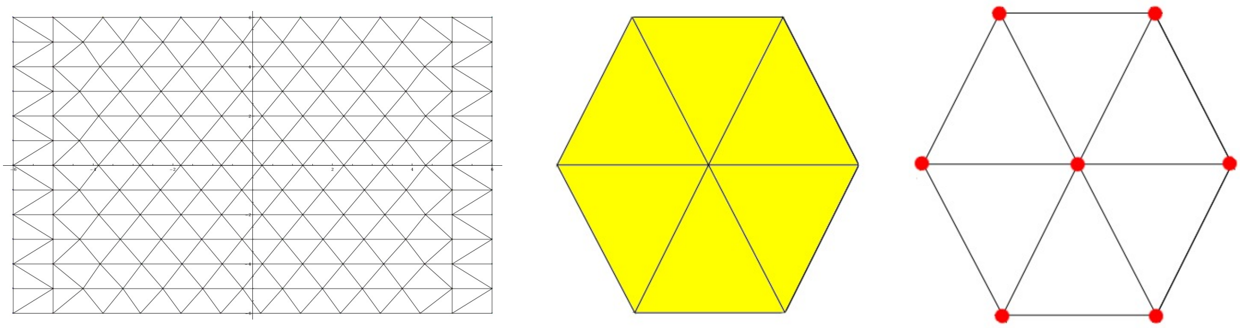

Figure 3.1: (a) Rectangular domain covered with finite elements, (b) finite elements in a hexagonal cell, (c) vertices for the cell.

Each vertex of the mesh has six neighbouring elements and six nearest neighbour vertices, Figure 3.2 (a). The potential from the neighbouring vertices is weighted by the area and angle of adjacent elements:

$$W_6 = \frac{\varepsilon_1 \cot \theta_{1b} + \varepsilon_6 \cot \theta_{6a}}{2} \quad (3.5)$$

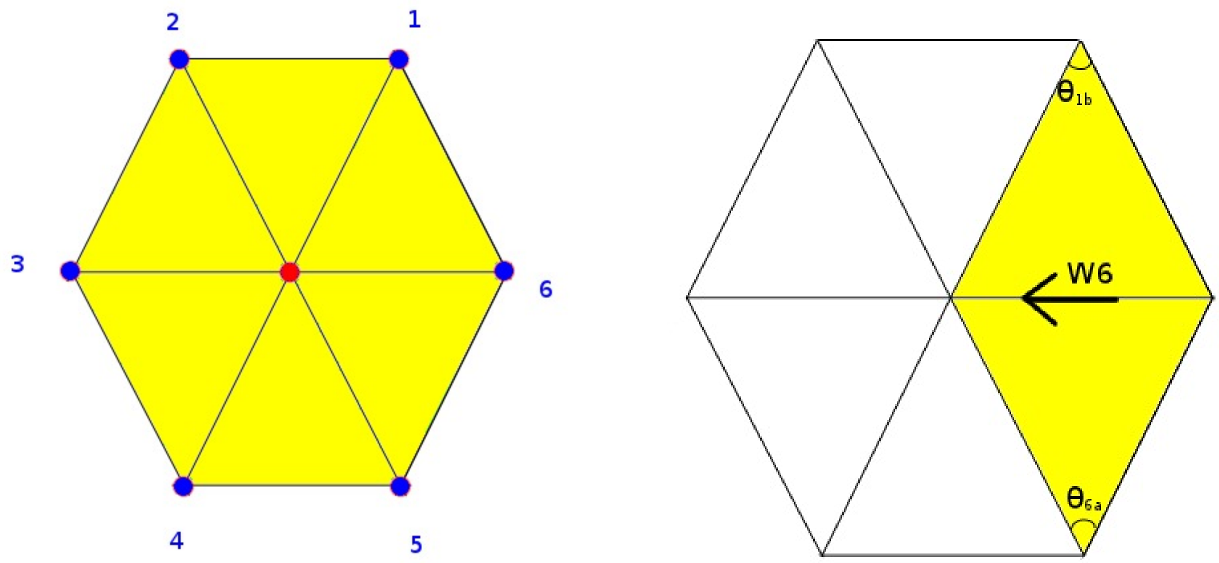

Figure 3.2: (a) Nearest neighbour vertices and (b) coupling constants associated with each vertex.

where ε is the local permittivity within each element and θ is the angle between two elements, Figure 3.2 (b). Potentials for the other vertices are calculated analogously, iterating through indices.

The coupling constants can be calculated directly from mesh information

$$\cot\theta_a = \frac{-y_1(y_2 - y_1) - x_1(x_2 - x_1)}{2a}, \tag{3.6}$$

$$\cot\theta_b = \frac{y_2(y_2 - y_1) + x_2(x_2 - x_1)}{2a}, \tag{3.7}$$

where

$$a = \frac{x_1 y_2 - x_2 y_1}{2}. \tag{3.8}$$

The various positions are taken relative to the third corner of the triangle, generally the vertex. The potential at each vertex can then be estimated using:

$$\phi_0 = \frac{\sum_{i=1}^{6}\left(\phi_i W_i + \frac{\rho_i A_i}{3\varepsilon_0}\right)}{\sum_{i=1}^{6} W_i}. \tag{3.9}$$

Here ρ_i and A_i are the charge collected and area of element i respectively.

A technique called successive over-relaxation can then be used to continue to update the potential until the error between updates is below a specified level. It is also possible to solve for the potential in one shot using a matrix formalism, which will be explored in an update to the code.

Experiments Using Smooth Focusing, AG Lattices and Conformal Vacuum Vessels

In Chapter 5 simulation experiments are performed to extend the work done in Chapter 4, in particular looking at the dynamic effects of beams with harmonic closed orbits. In the first parts of the chapter the particles are tracked through a smooth focusing lattice, whilst in the later parts an alternating gradient lattice is used. For the smooth focusing and one of the AG cases the vacuum vessel and boundary conditions are kept constant, whilst in the final part an AG lattice is simulated with conformal vacuum vessels and appropriate boundary conditions. In Chapter 7 simulations with the AG lattice and conformal vacuum vessel are used to study the 180 MeV Injection Upgrade design.

Smooth Focusing

If smooth focusing is enabled, Set does not load a lattice and instead updates the particle trajectories each simulation step using a constant betatron tune. In this model the beta functions of the machine are also constant. Each simulation step the particle angles are updated as

$$x_p = x_p - \left(\frac{Q_x}{r_0}\right)^2 xs \tag{3.10}$$

where x_p is the conjugate momenta of the particle, Q_x is the betatron tune, r_0 is the machine radius, x is the particle position and s is the length of the element being traversed. These kicks are provided at the same time as the space charge kicks outlined above. The position x is then updated

$$x = x + x_p s. \tag{3.11}$$

If a driven harmonic closed orbit is required, it is provided by

$$x_p = x_p + kick \times \sin\left(F_d\, 2\pi\, \frac{dist}{C}\right) \tag{3.12}$$

where $kick$ is the kick strength, F_d is the kick azimuthal frequency, $dist$ is the cumulative distance around the accelerator and C is the circumference. Alternatively, a single kick may be applied once per turn, in which case the closed orbit will have the frequency of the nearest half integer to the betatron tune, Q.

Lattice Class

If the lattice is AG then it is composed in the following way. Matrices for the lattice are comprised of three types: drifts, combined function bending magnets and quadrupoles [41]. These matrices provide the solution of the trajectory equations of the particles.

For a drift space:

$$\begin{pmatrix} C & S & D \\ C' & S' & D' \\ 0 & 0 & 1 \end{pmatrix} = \begin{pmatrix} 1 & l & 0 \\ 0 & 1 & 0 \\ 0 & 0 & 1 \end{pmatrix}. \tag{3.13}$$

Here and in the following matrices C and S are the Cosine and Sine like trajectories and D the dispersion trajectory with the primed quantities being the momenta trajectories. l is the length of the element.

Focusing combined function magnet:

$$\begin{pmatrix} \cos\phi & \frac{1}{\sqrt{|K|}}\sin\phi & \frac{1}{\rho K}(1-\cos\phi) \\ -\sqrt{|K|}\sin\phi & \cos\phi & \frac{1}{\rho\sqrt{K}}\sin\phi \\ 0 & 0 & 1 \end{pmatrix}. \tag{3.14}$$

Defocusing combined function magnet:

$$\begin{pmatrix} \cosh\phi & \frac{1}{\sqrt{|K|}}\sinh\phi & -\frac{1}{\rho K}(1-\cosh\phi) \\ \sqrt{|K|}\sinh\phi & \cosh\phi & \frac{1}{\rho\sqrt{|K|}}\sinh\phi \\ 0 & 0 & 1 \end{pmatrix}. \tag{3.15}$$

Focusing quadrupole:

$$\begin{pmatrix} \cos\phi & \frac{1}{\sqrt{|k|}}\sin\phi & 0 \\ -\sqrt{|k|}\sin\phi & \cos\phi & 0 \\ 0 & 0 & 1 \end{pmatrix}. \tag{3.16}$$

Defocusing quadrupole:

$$\begin{pmatrix} \cosh\phi & \frac{1}{\sqrt{|k|}}\sinh\phi & 0 \\ \sqrt{|k|}\sinh\phi & \cosh\phi & 0 \\ 0 & 0 & 1 \end{pmatrix}. \tag{3.17}$$

k is the normalised quadrupole strength. $K = k$ in the vertical plane and $-k + \frac{1}{\rho^2}$ in the horizontal plane. ρ is the bending radius of the combined function magnet. $\phi = l\sqrt{|K|}$ for the combined function magnets and $\phi = l\sqrt{|k|}$ for the quadrupoles.

These matrices can be multiplied together to produce the matrix for a cell, super-period or complete turn. Twiss parameters such as α, β, γ and the betatron tune Q can be obtained from them using standard methods. For simulating ISIS, a table of values for l, ρ, k is available which has been produced from magnet measurements including sensitive areas such as fringe fields. For other machines these matrices can read in from MAD output.

During simulation, each lattice element is split in two, with a space charge kick occuring centrally. The velocity and position updates are also offset by half a time step in order to reduce noise propagation [39].

There are also tools to apply trim quadrupole harmonics. Single and harmonic closed orbit kicks are applied in the same way as with smooth focusing. It is possible to match an input beam to a lattice (or mis-match) using input parameters.

There are more sophisticated methods of obtaining transfer maps, however this method is simple and easily implemented. Use of 2nd order coordinates is not currently implemented.

Poisson Solver Benchmarks

The mathematics software tool Mathematica [42] contains an optimised differential equation solver which has been used to benchmark the Poisson Solver from Set. The solver is available as part of the package "DifferentialEquations" and interpolation is provided by "InterpolatingFunctionAnatomy". These packages solve a given differential equation with boundary conditions using grid methods which are automatically chosen. While a variety of options are available to increase the accuracy, it has been found that best accuracy is provided simply by forcing the grid to be extremely fine. One of the pleasant features of the tool is that an arbitrary distribution can be provided to the Poisson solver. For example for a circular, uniform density (KV) beam in a square aperture:

```
uval = NDSolveValue[{D[u[x, y], x, x] + D[u[x, y], y, y]
  == If[((x - bx)^2 + (y - by)^2) <= br^2, -4/(br^2), 0],
  u[x, -yap] == u[x, yap] == u[-xap, y] == u[xap, y] == 0}
, u, {x, -xap, xap}, {y, -yap, yap}, Method ->
{"FiniteElement", "MeshOptions" -> {MaxCellMeasure -> 1}},
AccuracyGoal -> 30, PrecisionGoal -> 30, WorkingPrecision
-> 30, InterpolationOrder -> 20]
```

This rather obtuse looking input solves for an (xap, yap) half aperture boundary, with a beam centred at (bx, by) with a radius of br. It forces a finite element solution with a maximum element size of 1. Accuracy, precision and interpolation order are all maximised, though in practice this has little effect given the small mesh. The total charge is -4π C. The

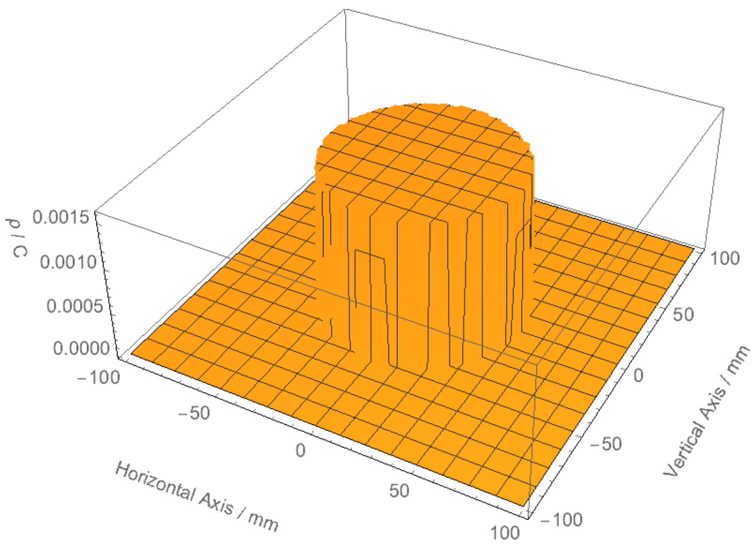

Figure 3.3: Circular, uniform density 4π charge distribution used in Mathematica model.

charge distribution solved for in this model, for an aperture of ± 100 mm in both planes and a centred beam radius 50 mm is shown in Figure 3.3. The resulting potential distribution is

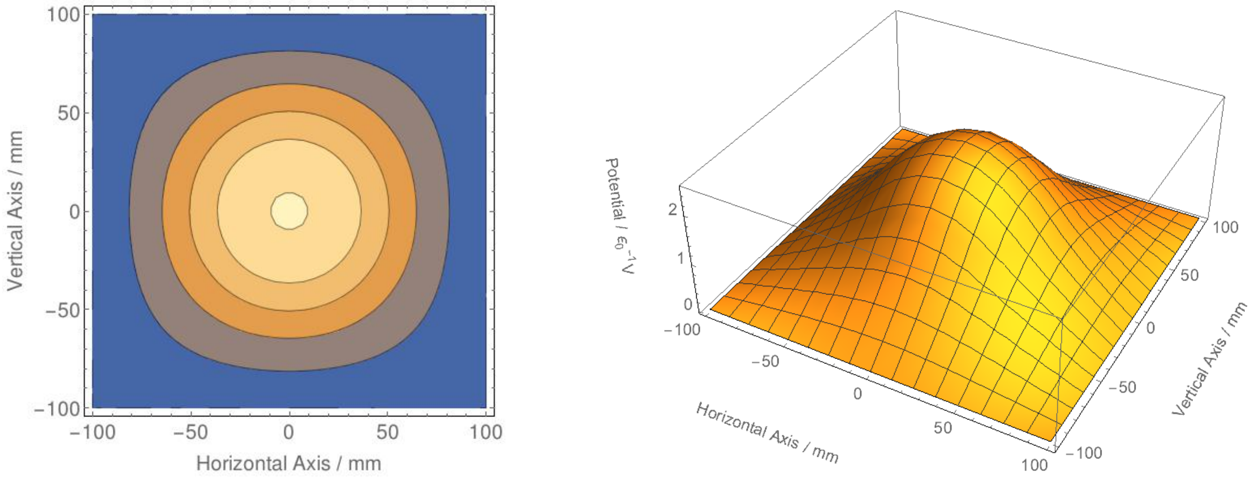

Figure 3.4: Contour plot (a) and 3D plot of potential produced in Mathematica model.

shown as a contour plot and 3D plot in Figure 3.4 (a) and (b) respectively.

The Poisson solvers from Set can be given a uniform beam input - the charge distribution is a uniform grid. With other input parameters analogous to those from Mathematica - a 200 × 200 cell grid for the FFT solver, and similar resolution for the FEA solver, the error between the solvers for a centred beam is as shown in Figures 3.5 and 3.6. Figure 3.5 (a) is a comparison between the values of the two potentials along a centre line through the grid, while (b) shows the relative error as a 3D plot, with an overall accuracy greater than 0.02%. Figure 3.6 shows the same values for the FEA solver, with an overall error less than 0.05%.

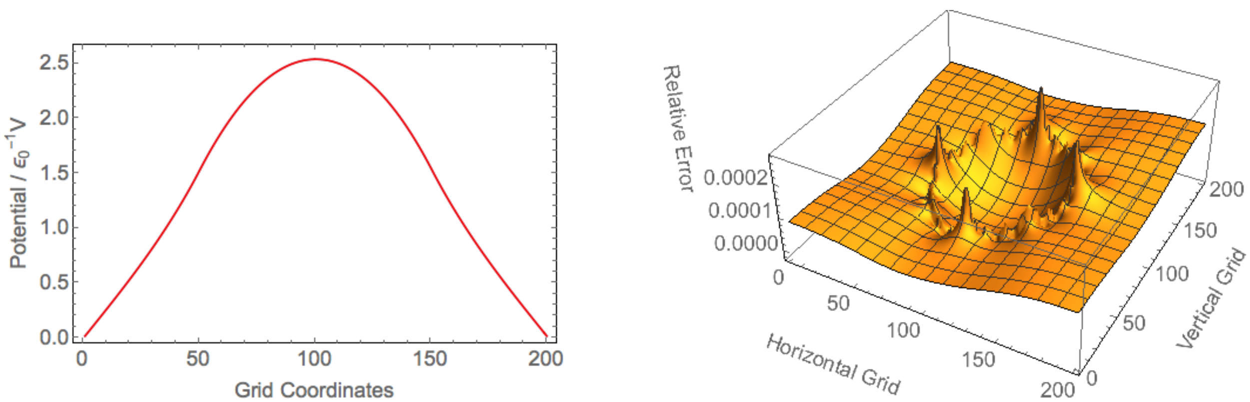

Figure 3.5: FFT Poisson Solver with uniform beam compared to Mathematica solution (a) comparison of centre line, (b) 3D plot of relative error.

Set normally creates beams using a random number generator to produce a KV or waterbag distribution. The fineness of the grid is also usually half that used in the previous studies. With these normal settings in place, figures 3.7 and 3.8 show the same data, but using a randomly generated KV beam with 50000 macroparticles. As can be seen the error

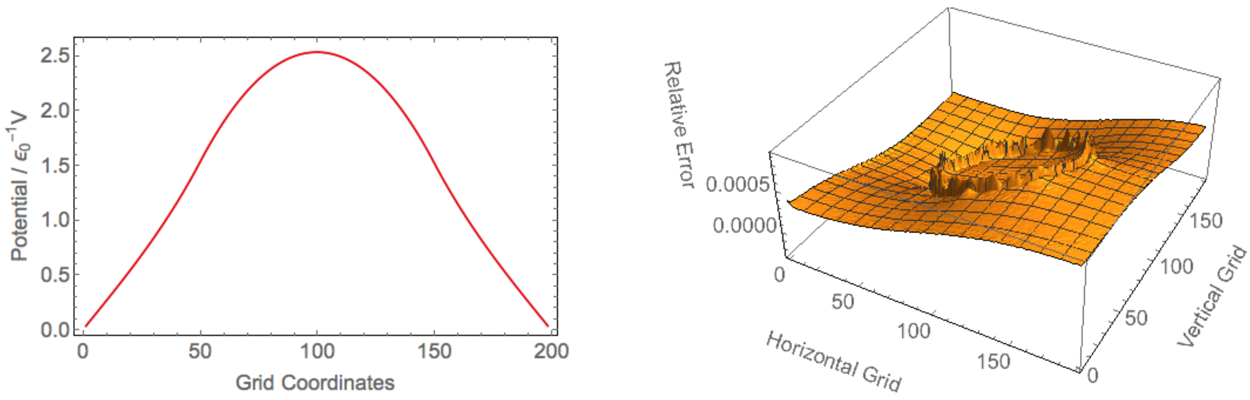

Figure 3.6: FEA Poisson Solver with uniform beam compared to Mathematica solution (a) comparison of centre line, (b) 3D plot of relative error.

gets worse as the beam has noise and is less well sampled, to 0.2% for both solvers (the error is more difficult to quantify as Mathematica is not using precisely the same input). The error between the FFT and FEA solvers is less than 0.1%. If the number of macro-particles in the distribution is increased to 5×10^5 and the grid fineness is doubled the error between the solvers reduces to less than 0.05%.

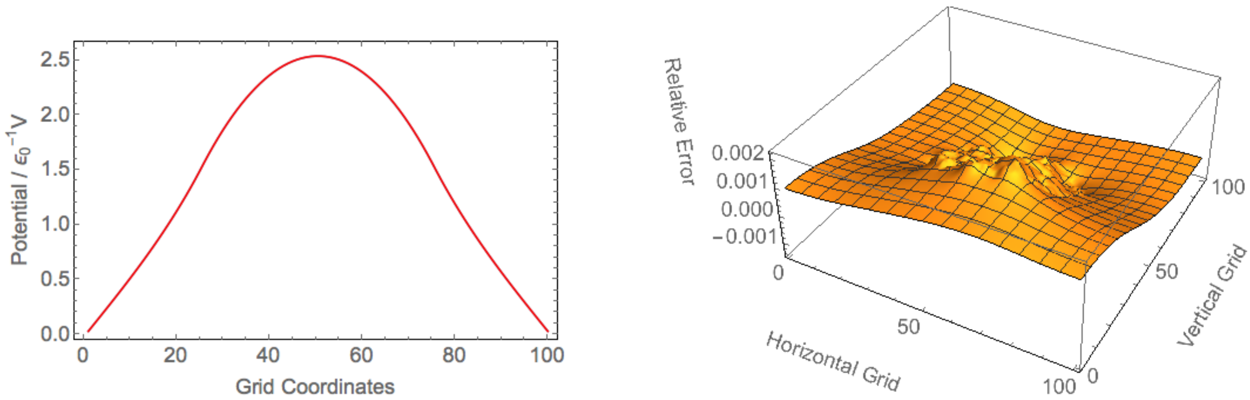

Figure 3.7: FFT Poisson Solver with uniform random beam compared to Mathematica solution (a) comparison of centre line, (b) 3D plot of relative error.

Further benchmark results are shown in Appendix A. These include beams with a horizontal offset, a horizontal and a vertical offset, small beams, small beams with offsets and simulations with large aspect ratio rectangular boundaries.

Chapter Summary

The simulation tools used in much of the thesis have been introduced and the numerical methods used have been explained.

Two independent space charge solvers which include electric images from rectangular vacuum vessels have been built and tested against commercially available solutions. They

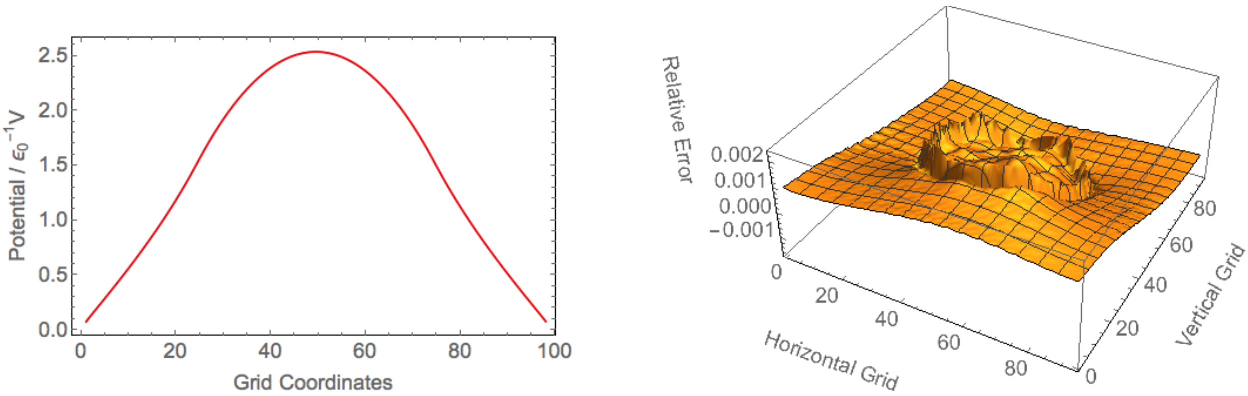

Figure 3.8: FEA Poisson Solver with uniform random beam compared to Mathematica solution (a) comparison of centre line, (b) 3D plot of relative error.

will be used in Chapter 4 to investigate analysis of beam images and come up with new solutions for realistic situations.

Tools for tracking particles through lattices, smooth focusing or alternating gradient, as well as space charge fields have been developed. While the lattice models are simple they allow reproduction of most physical accelerator behaviour in the transverse plane, neglecting momentum dependent terms and magnetic images. In Chapters 5 and 7, Set is used to model increasingly complex and realistic beams and lattices with closed orbits and investigate image induced beam resonances.

The original reason for developing a new code, that of accurately simulating the effects of the conformal vacuum vessel, has been supplemented by others. It has proved invaluable to have a tool that can be edited, modified, honed and expanded to meet the purpose at hand. Additions include calculation of beam moments and FFT spectra, single particle incoherent tunes, beam halo, Poincare Maps and lost particle tracking.

Chapter 4

Image Field Terms for Uniform Beams in Rectangular Geometry

Introduction

Understanding how image fields depend on the particle position and beam centroid for beams circulating in the conformal rectangular ISIS vacuum vessels is essential for developing models of beam behaviour and loss. A review of analytical calculations of electric fields for pencil beams in parallel plate and rectangular geometry metallic vacuum vessels is presented, showing steps in the derivation of the most important results.

The transition from the simpler parallel plate case to the more realistic treatment of round uniform beams in rectangular geometry is of particular relevance for ISIS. Therefore with the help of numerical solvers the applicability of each model was explored as a function of important parameters. The numerical methods show the limits of the theory, and suggest ways to extend it for use in more practical situations. Accuracy of numerical field calculations was ensured with the use of two independent field solvers.

A key result of the chapter was the numerical derivation of the higher order image co-efficients as the vacuum vessel geometry goes from rectangular (closer to parallel plate) to square. Image co-efficients were also investigated in the plane orthogonal to the beam offset and new image terms suggested.

Overview

The ISIS Synchrotron has a unique conformal rectangular vacuum vessel which is manufactured to follow the profile of the design beam envelopes in both planes. Interactions between the beam and vacuum vessel can be modelled as image forces which act back on the beam. When the beam is off-centre, there are additional components of the images which may contribute to beam loss. Magnetic image terms from the magnet poles were not considered here.

These forces have been analysed elsewhere for pencil beams in parallel plate geometry by Laslett [43] and Baartman [44], and also for pencil beams in rectangular geometry by Ng [45, 46]. Two analyses of transverse motion for closed orbit driven image resonances [44, 47], approximate the rectangular aperture using infinite parallel plates to make the analysis more straightforward. In both papers the image field components are extracted as a power series, based on the approach used by Laslett.

The parallel plate analysis is outlined here in Sections 4.3 and 4.4, as the derivation is not trivial. A further analysis due to Ng uses elliptical functions to solve exactly for the images from a centred or off-centred beam in rectangular geometry. Ng's results for a centred beam are summarised in Section 4.5. In Section 4.6 the simulation methods used to test the image fields will be briefly described, with the results for centred round beams in rectangular geometry vacuum vessels given in Section 4.7. A comparison with the theoretical results using pencil beams is made. In Section 4.8 the image coefficients for off-centred round beams are explored and a table of the numerically determined co-efficients produced. The 2D nature of the image potentials as well as values for the image coefficients in the orthogonal plane is explored in Section 4.9. Finally there will be a summary and brief outline of future work.

Laslett: Image Terms Due to Pencil Beams in Parallel Plate Geometry

Conformal Mapping

Following Laslett [43], parallel plate geometry is used as an approximation to rectangular. For a pencil beam centred at $\bar{y}$ between two infinite parallel plates at $\pm h$ and a field point at y as shown in Figure 4.1, there are an infinite series of images above and below the plates. Conformal mapping may be used to transform to a new system where the images are easier to obtain. The transformation $z' = \mathrm{e}^{\pi(z+ih)/2h}$ carries points 1 - 5 from Figure 4.1 into the real number line in z' as shown in Figure 4.2. The complex potential in z' is $W = U + iV$

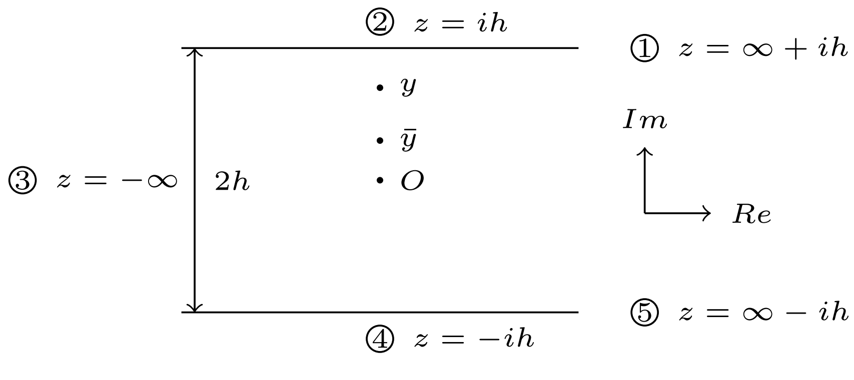

Figure 4.1: Parallel plate geometry before conformal mapping.

and the real part of this is the solution to the potential in z. The line charge at $i\bar{y}$ goes to

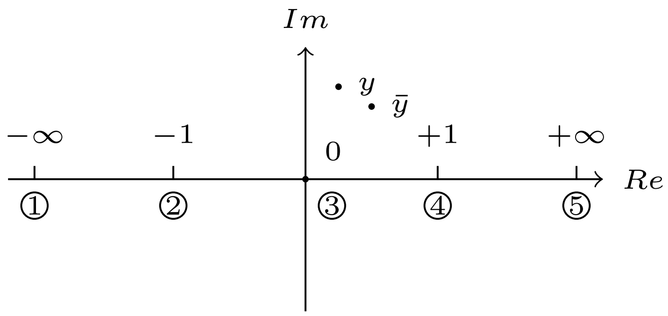

Figure 4.2: Parallel plate geometry after a conformal mapping into the real axis.

$\mathrm{e}^{i\pi(\bar{y}+h)/2h}$, while the field point at iy goes to $\mathrm{e}^{i\pi(y+h)/2h}$. The infinite series of images in z have become one image in z' located at $\mathrm{e}^{-i\pi(\bar{y}+h)/2h}$.

The potential due to a line charge, line charge density λ, is $W = -\frac{\lambda \ln|z|}{2\pi\varepsilon_0}$.

$$W = -\frac{\lambda}{2\pi\varepsilon_0}\left(\ln\left|\mathrm{e}^{i\pi(y+h)/2h} - \mathrm{e}^{i\pi(\bar{y}+h)/2h}\right| - \ln\left|\mathrm{e}^{i\pi(y+h)/2h} - \mathrm{e}^{-i\pi(\bar{y}+h)/2h}\right|\right). \tag{4.1}$$

To make the denominator real multiply through by its complex conjugate:

$$W = -\frac{\lambda}{2\pi\varepsilon_0}\ln\left|\frac{1 + \mathrm{e}^{i\pi(y+\bar{y})/2h} - \mathrm{e}^{2i\pi\bar{y}/2h} - \mathrm{e}^{-i\pi(y-\bar{y})/2h}}{2(1+\cos\left(\pi(y+\bar{y})/2h\right))}\right|. \tag{4.2}$$

Selecting the real part of $W = U + iV$. For a complex number $z = Re^{i\theta}$ the logarithm is $\ln|z| = \ln|R| + i\theta$.

$$U = \ln|R| = \sqrt{zz^*}. \tag{4.3}$$

$$\begin{aligned} U = -\frac{\lambda}{2\pi\varepsilon_0}\ln\Bigg|\Big(&4 + 2(\mathrm{e}^{i\pi(y+\bar{y})/2h} + \mathrm{e}^{-i\pi(y+\bar{y})/2h} - \mathrm{e}^{i\pi(y-\bar{y})/2h} - \mathrm{e}^{-i\pi(y-\bar{y})/2h}) - \mathrm{e}^{2i\pi y/2h} \\ &- \mathrm{e}^{-2i\pi y/2h} - \mathrm{e}^{2i\pi\bar{y}/2h} - \mathrm{e}^{-2i\pi\bar{y}/2h}\Big)^{\frac{1}{2}} \Big/ \left(2(1+\cos(\pi(y+\bar{y})/2h)\right)\Bigg|. \end{aligned} \tag{4.4}$$

Converting to trigonometric functions

$$U = -\frac{\lambda}{2\pi\varepsilon_0}\ln\left|\frac{\sin(\pi y/2h) - \sin(\pi\bar{y}/2h)}{1+\cos(\pi(y+\bar{y})/2h))}\right|. \tag{4.5}$$

Power Series Expansion

In the proceeding section the solution was exact. Now the answer will be approximated using power series expansions. Laslett expanded the series to a power of two but as will become clear an expansion to a power of three must be made initially. First the denominator:

$$F(x) = \frac{1}{1+\cos x} = a_0 + a_1 x + a_2\frac{x^2}{2!} + \ldots \tag{4.6}$$

$$F(x) = \frac{1}{2} + \frac{x^2}{8} + \ldots \tag{4.7}$$

Expanding the sin terms to 3rd power also, and ignoring π and factors of $2h$ for now:

$$\frac{\sin y - \sin \bar{y}}{1+\cos(y+\bar{y})} = \left(y - \frac{y^3}{6} - \bar{y} + \frac{\bar{y}^3}{6}\right)\left(\frac{1}{2} + \frac{(y+\bar{y})^2}{8}\right). \tag{4.8}$$

$$+ \text{ higher order terms.}$$

$$\simeq \frac{y}{2} - \frac{\bar{y}}{2} + \frac{y^3}{24} + \frac{3y^2\bar{y}}{24} - \frac{3y\bar{y}^2}{24} - \frac{\bar{y}^3}{24} \tag{4.9}$$

$$\simeq \left(\frac{y-\bar{y}}{2}\right)\left(1 + \frac{y^2+4y\bar{y}+\bar{y}^2}{12}\right). \tag{4.10}$$

Inserting this into Equation 4.5

$$U \simeq -\frac{\lambda}{2\pi\varepsilon_0}\left(\ln\left|\frac{\pi(y-\bar{y})}{4h}\right| + \ln\left|1 + \frac{\pi^2(y^2+4y\bar{y}+\bar{y}^2)}{48h^2}\right|\right). \tag{4.11}$$

Then expand the second term using $\ln|1+x|$ to give

$$\simeq -\frac{\lambda}{2\pi\varepsilon_0}\left(\ln\left|\frac{\pi(y-\bar{y})}{4h}\right| + \frac{\pi^2(y^2+4y\bar{y}+\bar{y}^2)}{48h^2}\right). \tag{4.12}$$

The first term is the potential of a bare line charge, the second is Laslett's expansion for images between parallel plates. Real high intensity beams are not point-like, but rather have a finite distribution. The image terms of a pencil beam need to be compared to those of a more realistic beam, and this is done numerically later in this chapter.

Differentiating the image potential with respect to y we obtain the image component of the electric field

$$E_y \simeq -\frac{\lambda}{2\pi\varepsilon_0}\frac{\pi^2}{48h^2}\left(2y+4\bar{y}\right). \tag{4.13}$$

We change variables to $\hat{y} = y - \bar{y}$ to give the field point in terms of the relative position to the beam

$$E_y \simeq -\frac{\lambda}{2\pi\varepsilon_0}\frac{\pi^2}{48h^2}\left(2\hat{y}+6\bar{y}\right). \tag{4.14}$$

Laslett's image co-efficients are divided by 4 so that they can be factored into the equation for the field of an elliptical beam, to obtain $\epsilon_1 = \frac{\pi^2}{48}$ for images due to the offset of the field point from the centre of the beam, and $\xi_1 = \frac{\pi^2}{16}$ for images due to the offset of the beam from the centre of the beam pipe, finally giving for the electric field due to images

$$E_y \simeq -\frac{\lambda}{\pi\varepsilon_0 h^2}\left(\epsilon_1\hat{y} + \xi_1\bar{y}\right). \tag{4.15}$$

Baartman: Image Terms Due to Pencil Beams in Parallel Plate Geometry

Baartman [44] follows Laslett, but expands Equation 4.5 in power series to the 5$^{\text{th}}$ power, ignoring factors of π and $2h$ for now.

$$\frac{\sin y - \sin \bar{y}}{1+\cos(y+\bar{y})} \simeq \left(y - \frac{y^3}{6} + \frac{y^5}{120} - \bar{y} + \frac{\bar{y}^3}{6} - \frac{\bar{y}^5}{120}\right)\left(\frac{1}{2} + \frac{(y+\bar{y})^2}{8} + \frac{(y+\bar{y})^4}{48}\right). \tag{4.16}$$

$$= \frac{y-\bar{y}}{2} + \frac{y^3+3y^2\bar{y}-3y\bar{y}^2-\bar{y}^3}{24} + \frac{y^5+5y^4\bar{y}+5y^3\bar{y}^2-5y^2\bar{y}^3-5y\bar{y}^4-\bar{y}^5}{240} \tag{4.17}$$

$$= \left(\frac{y-\bar{y}}{2}\right)\left(1 + \frac{y^2+4y\bar{y}+\bar{y}^2}{12} + \frac{y^4+6y^3\bar{y}+11y^2\bar{y}^2+6y\bar{y}^3+\bar{y}^4}{120}\right). \tag{4.18}$$

Inserting this into Equation 4.5

$$U \simeq -\frac{\lambda}{2\pi\varepsilon_0}\left(\ln\left|\frac{\pi(y-\bar{y})}{4h}\right| + \ln\left|1 + \frac{\pi^2(y^2+4y\bar{y}+\bar{y}^2)}{48h^2} + \frac{\pi^4(y^4+6y^3\bar{y}+11y^2\bar{y}^2+6y\bar{y}^3+\bar{y}^4)}{960h^4}\right|\right). \tag{4.19}$$

Now expand $\ln|1+x|$ to the third power $\simeq x - \frac{x^2}{2} + \frac{x^3}{3}$

$$U \simeq -\frac{\lambda}{2\pi\varepsilon_0}\left(\ln\left|\frac{\pi(y-\bar{y})}{4h}\right| + \frac{\pi^2(y^2+4y\bar{y}+\bar{y}^2)}{48h^2} + \frac{\pi^4(7y^4+32y^3\bar{y}+42y^2\bar{y}^2+32y\bar{y}^3+7\bar{y}^4)}{23040h^4}\right). \tag{4.20}$$

Leave out the term due to the free line charge and differentiate with respect to y to get E_y

$$E_y = \frac{\lambda}{4\pi\varepsilon_0}\left(\frac{\pi^2}{24h^2}(2y+4\bar{y}) + \frac{\pi^4}{11520h^4}(28y^3+96y^2\bar{y}+84y\bar{y}^2+32\bar{y}^3)\right). \tag{4.21}$$

Baartman then rearranged this in terms of $\hat{y} = y - \bar{y}$ to give

$$E_y = \frac{\lambda}{4\pi\varepsilon_0}\left(\frac{\pi^2}{24h^2}(2\hat{y}+6\bar{y}) + \frac{\pi^4}{11520h^4}(28\hat{y}^3+180\hat{y}^2\bar{y}+360\hat{y}\bar{y}^2+240\bar{y}^3)\right) \tag{4.22}$$

$$E_y = \frac{\lambda}{4\pi\varepsilon_0}\left(\frac{\pi^2\hat{y}}{12h^2} + \frac{\pi^2\bar{y}}{4h^2} + \frac{28\pi^4\hat{y}^3}{11520h^4} + \frac{\pi^4\hat{y}^2\bar{y}}{64h^4} + \frac{\pi^4\hat{y}\bar{y}^2}{32h^4} + \frac{\pi^4\bar{y}^3}{48h^4}\right). \tag{4.23}$$

The first two terms are Laslett's linear image terms. The others represent non-linear higher order terms which are functions of both the distance of the field point from the beam centre, and the beam centre offset from the origin. It is these higher order terms that Rees, Prior [47] and Baartman thought might describe image based driving terms, some deriving from closed orbits, that lead to loss on ISIS.

For an off-centred beam the higher order image terms can become significant. Baartman goes on to describe general higher order image coefficients κ in a way analogous to those in Equation 4.23

$$\frac{E_{yimage}}{4\lambda} = \frac{1}{4\pi\varepsilon_0}\left(\epsilon_1\frac{\hat{y}}{h^2} + \xi_1\frac{\bar{y}}{h^2} + \kappa_{30}\frac{\bar{y}^3}{h^4} + \kappa_{21}\frac{\hat{y}\bar{y}^2}{h^4} + \kappa_{12}\frac{\hat{y}^2\bar{y}}{h^4} + \kappa_{03}\frac{\hat{y}^3}{h^4} + ...\right) \tag{4.24}$$

The terms in this equation will be used as a basis for understanding the strength and effect of image driving terms using numerical methods in the rest of this chapter.

Ng: Elliptic Function Solution for Image Terms Due to Pencil Beams in Rectangular Geometry

Ng used conformal mapping to calculate the potential of a line charge with a rectangular boundary. He solved for the potential using elliptic functions to find the exact solution [45, 46]. Elliptic functions are doubly periodic functions in the complex plane.

For a centred beam the elliptical functions simplify to (see Equation 3.109 from [46]):

$$\mathrm{sn}\left(\frac{K(k')}{2}, k'\right) = \frac{1}{\sqrt{1+k}}, \tag{4.25}$$

$$\mathrm{cn}\left(\frac{K(k')}{2}, k'\right) = \frac{\sqrt{k}}{\sqrt{1+k}}, \tag{4.26}$$

$$\mathrm{dn}\left(\frac{K(k')}{2}, k'\right) = \sqrt{k}. \tag{4.27}$$

sn, cn and dn are defined as follows [48]. If the incomplete elliptic integral of the first kind

$$u = \int_0^{\phi} \frac{d\theta}{\sqrt{1 - m\sin^2\theta}} \tag{4.28}$$

then

$$\mathrm{sn}u = \sin\phi, \tag{4.29}$$

$$\mathrm{cn}u = \cos\phi \tag{4.30}$$

and

$$\mathrm{dn}u = \sqrt{1 - m\sin^2\phi}. \tag{4.31}$$

The nome is a special function defined as

$$q = \mathrm{e}^{-\frac{\pi K'}{K}}, \tag{4.32}$$

where K and K' are the quarter periods of the functions. For the case of rectangular geometry the nome is $q = \mathrm{e}^{-2\pi\omega/h}$. The argument of the doubly periodic functions can be approximated if the ratio of the vacuum vessels satisfies certain conditions:

$$k^2 = 16q(1 - 8q + 44q^2 - 192q^3 + 718q^4 - 2400q^5 + 7352q^6 - 20992q^7 + 56549q^8). \tag{4.33}$$

$$K(k) = \frac{\pi}{2}\left[1 + \frac{1}{4}k^2 + \frac{9}{64}k^4 + \mathcal{O}(k^6)\right]. \tag{4.34}$$

Following these steps a simple estimate can be made for the image co-efficient for a centred beam cf. Equation 4.15

$$\epsilon_1 = \frac{K^2(k)}{12}(1 - 6k + k^2). \tag{4.35}$$

As will be seen later in the chapter, this approach accurately described the behaviour of Laslett's image coefficients as the vacuum vessel aspect ratio changed. The approach using elliptic functions shows promise as a method to calculate images analytically for pencil beams in rectangular geometry. However in order to solve for off-centred 2D round beams, alternative numerical methods were used in the rest of the thesis.

Simulation Models with 2D Round Beams

The Poisson solvers introduced in Chapter 3 were used in this section and those that follow to study image forces. In this section the method will be described and some initial results demonstrated, then in the next three sections the solvers will be used to investigate the different models introduced in Sections 4.3 to 4.5. The simulation model allowed the generation of a 2D round beam distribution in a rectangular geometry aperture, and calculation of the resulting potential and electric fields. Two Poisson solvers were compared for this task, one using a rectangular mesh with an FFT solver and the other using a triangular mesh and an FEA solver. These were thoroughly described and benchmarked in the previous chapter.

For these simulations a round, uniform density beam distribution was used as it has a linear space charge force which can easily be compared with theory. 5×10^5 macro particles were used for each of the simulations as this number gave acceptably low statistical noise. The fields of a uniform beam in free space were subtracted from the results to obtain the image fields.

A standard terminology is adopted here to describe the simulations to try to avoid confusion. The analysis above was all 1D with pencil beams, parallel plate or rectangular geometry. The simulations are 2D with uniform beams in rectangular geometry. Beams may be centred or off-centred. Simulations will be described with aspect ratio w/h, for (horizontal, vertical) dimensions (w, h). The size of the beam relative to the vertical dimension is h/r for a beam radius r. Field points are at (x, y) and the beam centre is at $(\bar{x}, \bar{y})$. Potentials and fields will be described in terms of $(x, y, \bar{x}, \bar{y})$.

The electric field $E_y(x, y, 0, 0)$ with a large, centred beam ($h/r = \sqrt{2}$) for the case of a square aperture ($w/h = 1$) is shown in Figure 4.3. The charge per macroparticle here and in the following sections was $4\pi/N$ where N was the number of macroparticles. Cloud-in-cell binning and interpolation were used for the FFT solver, which reduced numerical errors introduced by the mesh discretisation, while the FEA solver used least squares fitting. The units are slightly strange as a consequence of using a space charge solver written for accelerator tracking, with the final fields given in units of ε_0 Vmm^{-1}. For each simulation, the electric field of a uniform beam in free space (linear field) was then subtracted from the generated field, to leave the field due to images. The image field for the same example is shown in Figure 4.4. Some additional results are shown below.

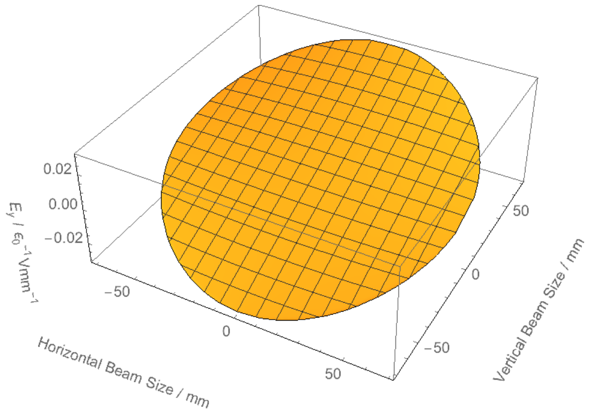

Figure 4.3: Field for a uniform beam in a square boundary.

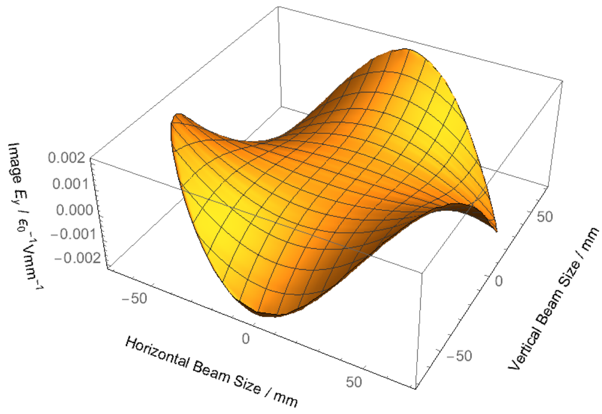

Figure 4.4: Image field for a uniform beam in a square boundary.

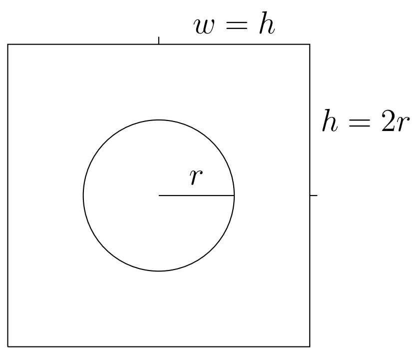

Figure 4.5: Schematic of simulation for square beam pipe, beam diameter = half aperture.

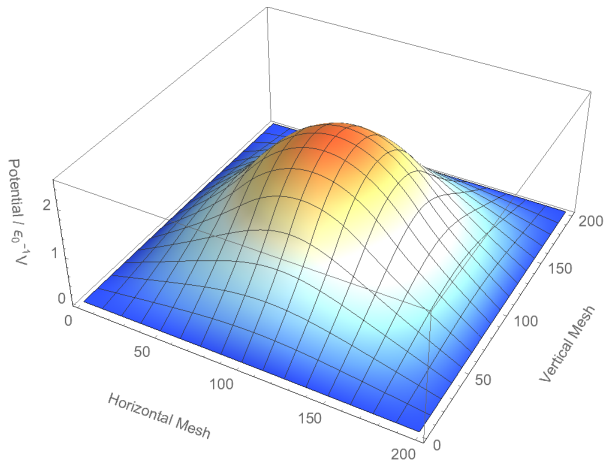

Figure 4.6: 3D plot of potential due to KV beam in square aperture.

Square Beam Pipe ($w/h = 1$), Beam Diameter = Half Aperture ($h/r = 2$)

This simulation was for a centred beam with a diameter half the aperture of a square beam pipe, using 200 x 200 mesh cells, shown schematically in Figure 4.5. The solvers were used to calculate the potential from the beam distribution, as shown in Figure 4.6 for the FFT solver. Horizontal and vertical electric fields ($E_x(x, y, 0, 0)$ and $E_y(x, y, 0, 0)$) were generated by the solvers, an example for the FFT is shown in Figure 4.7. If those fields are plotted along the horizontal and vertical axes of the beam, they can be compared with the prediction for a uniform beam in free space, as shown in Figure 4.8. As can be seen, in this instance (centred beam, square beampipe), there was very little deviation from the free space case, i.e. the image terms are small. The relative error between the solvers for the electric field was less than 0.5%.

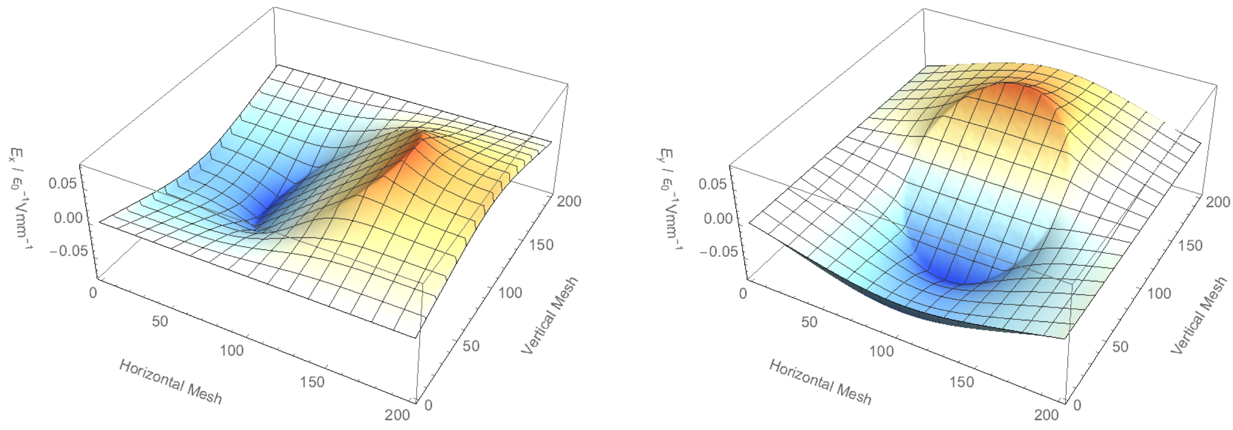

Figure 4.7: Fields produced by FFT solver: left horizontal and right vertical.

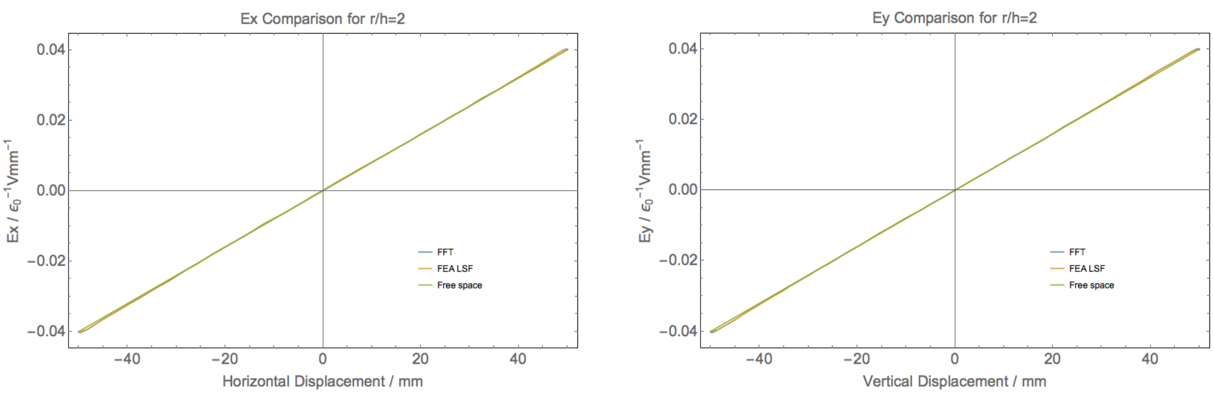

Figure 4.8: Fields produced by FFT and FEA solvers, compared with those for a KV beam in free space: left horizontal axis and right vertical axis.

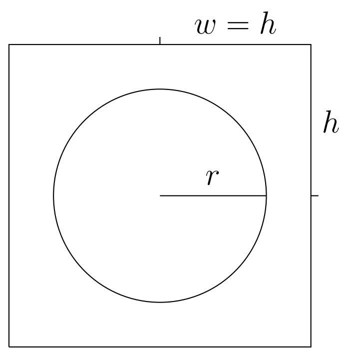

Figure 4.9: Schematic of simulation for square beam pipe, beam diameter $= 1/\sqrt{2}$ aperture.

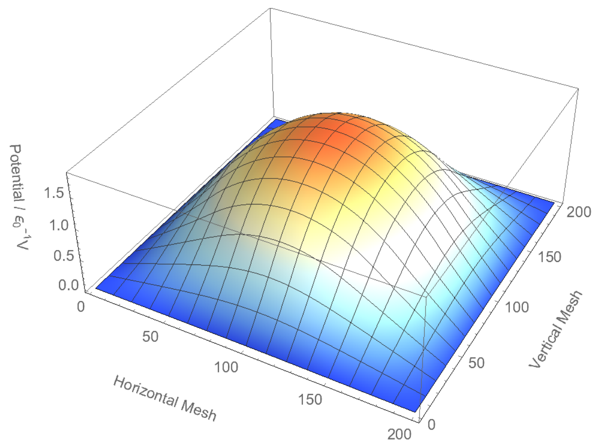

Figure 4.10: 3D plot of potential due to KV beam in square aperture, where beam diameter to aperture ratio is $\sqrt{2}$.

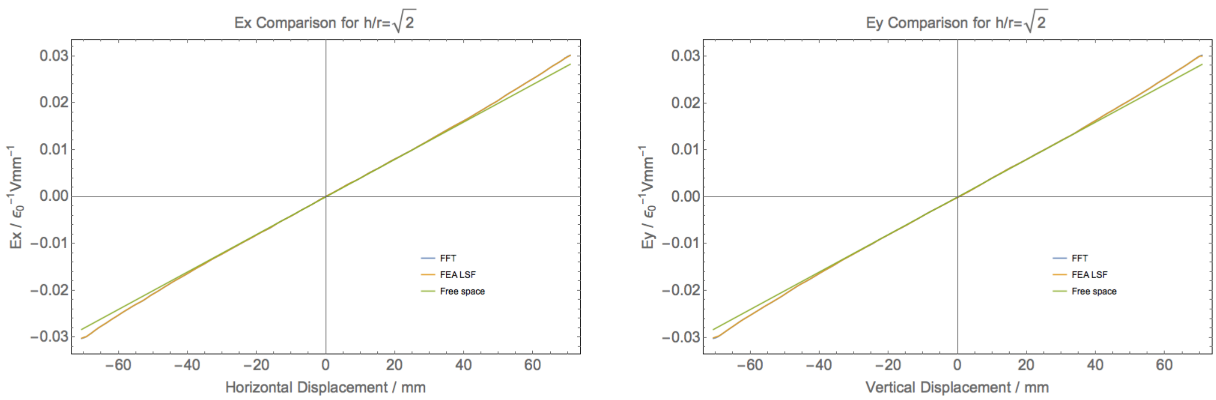

Figure 4.11: Fields produced by FFT and FEA solvers, where diameter to aperture ratio is $\sqrt{2}$, compared with those for a KV beam in free space: left horizontal axis and right vertical axis.

Square Beam Pipe ($w/h = 1$), Beam Diameter $= 1/\sqrt{2}$ Times Aperture ($h/r = \sqrt{2}$)

The same exercise was performed with a larger beam, where the ratio of aperture to diameter was a factor of $\sqrt{2}$ rather than 2, more like the situation which exists at ISIS where the beam fills the available aperture (Figure 4.9). These results are shown in Figures 4.10 and 4.11. As can be seen in Figure 4.11, the image forces were starting to modify the behaviour of the fields, as the beam was larger inside the beam pipe. There was a visible deviation from the case of a KV beam in free space. The relative error for the electric field between the solvers was less than 0.5%.

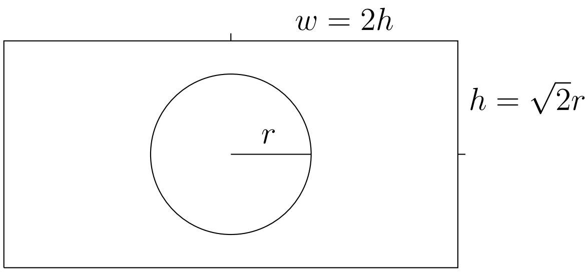

Figure 4.12: Schematic of simulation for rectangular beam pipe, beam diameter = $1/\sqrt{2}$ aperture.

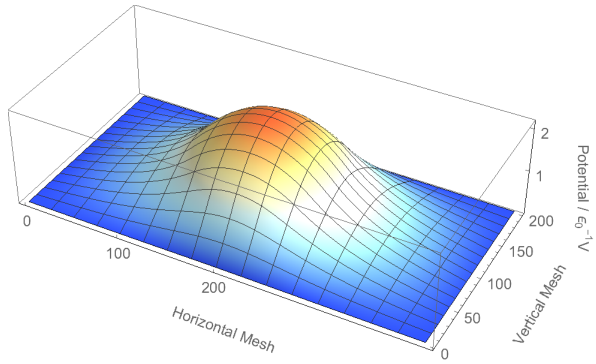

Figure 4.13: 3D plot of potential due to KV beam in rectangular aperture.

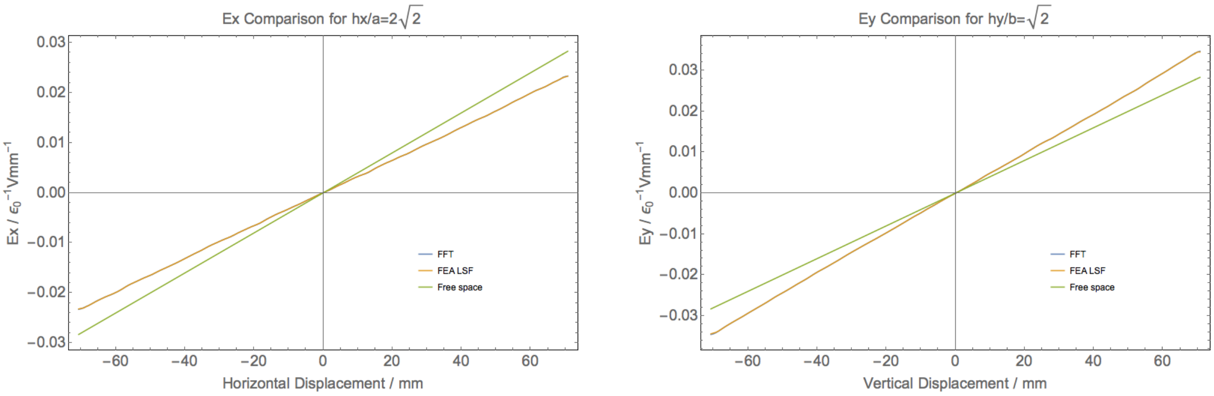

Figure 4.14: Fields produced by FFT and FEA solvers, in a rectangular aperture, compared with those for a KV beam in free space: left horizontal axis and right vertical axis.

Rectangular Beam Pipe ($w/h = 2$), Vertical Half Aperture = $\sqrt{2}$, Beam Radius ($h/r = \sqrt{2}$), Horizontal Half Aperture = $2\sqrt{2}$

The simulation was also repeated with the beam in a rectangular aperture where the vertical half aperture was still $\sqrt{2}$ times the beam radius, but the horizontal was twice that (Figure 4.12). The number of mesh cells for both the FFT and FEA solvers was doubled in the horizontal direction. The potential produced by this configuration can be seen in Figure 4.13, while the fields are plotted along the beam axes in Figure 4.14. In this case, image forces clearly modified the behaviour of the horizontal and vertical electric fields compared with those for a beam in free space. The relative error between the solvers for the electric field was less than 0.6%.

Summary of Simulation Model

The simulation model has been introduced and some definitions introduced which will simplify descriptions in later sections. The two main solvers available in the code have been compared for generating image fields. There was close agreement between the FFT and FEA

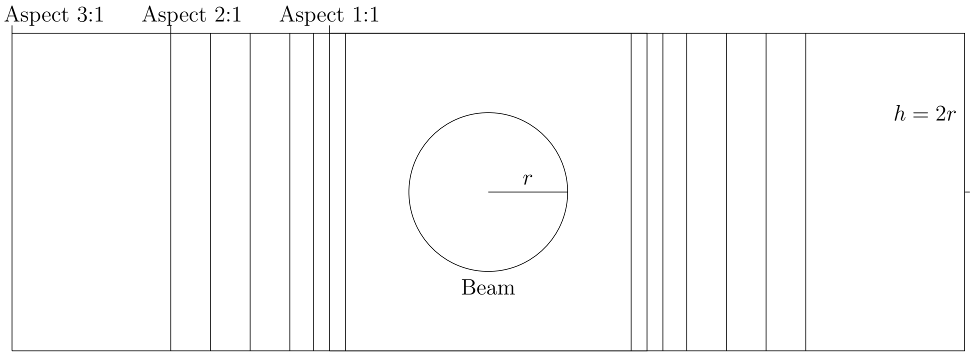

Figure 4.15: Schematic of simulation showing beam dimension and aspect ratio.

solvers, provided the number of mesh cells was sufficient in either case. Linear interpolation, initially used with the FEA solver, was improved to a least squares fit routine during the course of the investigations. For the following sections of the chapter, though both solvers were used, only results from the FFT solver will be presented.

Dependence of Image Coefficients on Aspect Ratio of Vacuum Vessel with a Centred Beam

Here we explore the range of validity for the parallel plate approximation compared with rectangular geometry. Only a centred beam was investigated for this initial study, so only the image terms due to a centred beam were considered.

An image co-efficient equivalent to Laslett's incoherent image term ϵ_1 (Equation 4.15) was obtained by taking the gradient of the image electric field along the vertical axis of the beam ($\frac{dE_y}{dy}(0, y, 0, 0)$). A set of simulations was run in which the beam pipe aspect ratio was varied in the horizontal direction, from 0.75 to 3 ($w/h = 0.75$ - 3), while it was held constant in the vertical at 100 mm. The beam radius was also constant at 50 mm ($h/r = 2$). These dimensions are illustrated in Figure 4.15.

Image coefficients were calculated from each simulation and the results plotted in Figure 4.16, along with Laslett's prediction for a centred beam between parallel plates.

A linear fit provided the best match to the image co-efficient, though a third order polynomial fit was also tried. Baartman's expansion (Equation 4.23) only adds very small terms to the solution for a centred beam on the vertical axis. The simulation result approaches Laslett's image term as the ratio of horizontal to vertical beam pipe size becomes larger. As Laslett's solution is for infinite parallel plates this is to be expected. It is also clear that Laslett's solution is the "worst case scenario" and so represents a pessimistic estimate, perhaps useful for machine designs where one wants to err on the side of caution. Errors were generated here from PIC noise by running the simulations 10 times with different randomly generated KV beams.

Ng's solution was also compared with these results, also in Figure 4.16. As can be seen

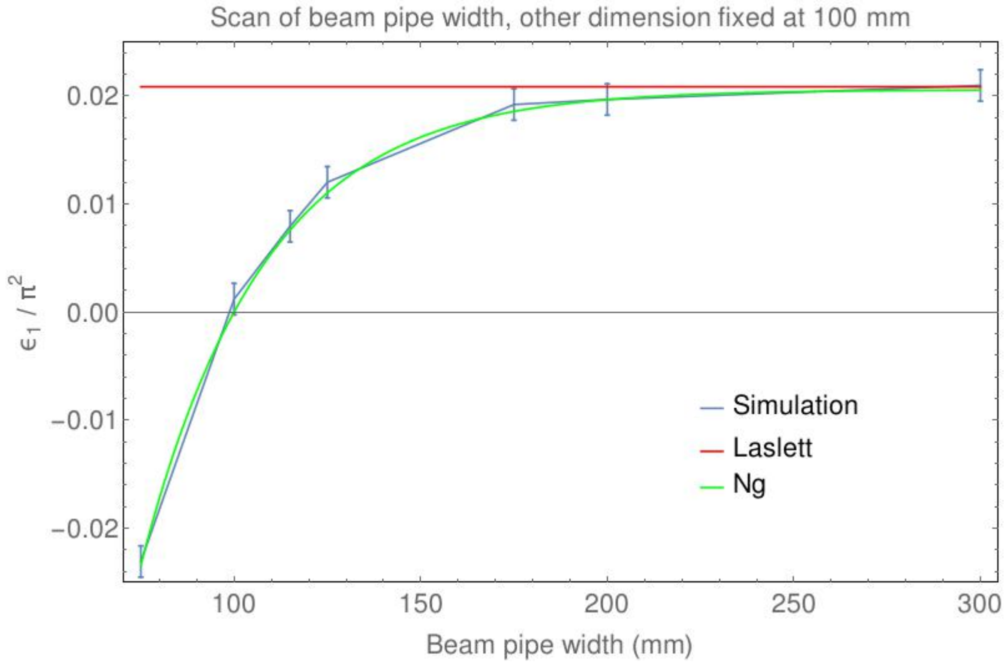

Figure 4.16: Results for a scan of beam pipe width from 75 - 300 mm, while height is held fixed at 100 mm. Laslett and Ng's image co-efficients for a centred beam compared with simulations.

this value for the image coefficient was a good fit for the simulation data. Ng's results for off-centred beams will be studied more in the future and compared with the simulation results below. However the numerical methods used here provide results for 2D round uniform beams and can be extended to other beam distributions and vacuum vessel geometries.

Results for Off-Centred Beam

Simulation Setup

A set of simulations was performed in which the vacuum chamber aspect ratio was swept from 0.9 to 3 ($w/h = 0.9$ - 3) and kept constant at 100 mm in the vertical direction. The beam was offset between 0 and 10 mm in steps of 1 mm in the vertical direction for each of these cases ($\bar{y} = 0$ - 10 mm). The beam was a regular round uniform distribution, it was not generated randomly in this case but was made from a regular grid to minimise noise. The beam radius was 0.7 of the vertical half beam pipe size (very close to the value used in [47] for the ISIS beam) ($h/r = \sqrt{2}$). These parameters are illustrated in Figure 4.17. The electric potential and fields were generated for each case, specifically calculated inside the beam ($E_y(x, y, 0, \bar{y})$).

Mathematica [42] was used to fit the image field in several steps (it was not possible to fit a 4D surface directly as there were so many more data points in x and y than in $\bar{y}$). A third order polynomial function with respect to y (the field point) was fitted to the electric

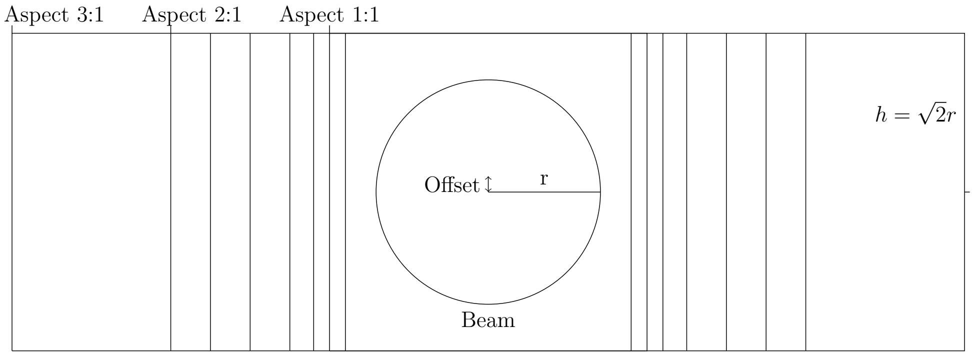

Figure 4.17: Schematic of simulation showing range of offset and aspect ratio.

field within the beam obtained from the simulations.

$$E_{iy}(x, y) = A + By + Cy^2 + Dy^3 \tag{4.36}$$

In Equation 4.36, E_{iy} is the vertical image field and A, B, C and D are variables to be determined from the simulation data.

Further fitting was carried out for A, B, C and D to obtain functions with respect to $\bar{y}$ (the beam offset) in order to obtain the values of the κ terms from Equation 4.24, i.e. A was fitted to an equation for $E\bar{y} + F\bar{y}^3$, where E and F are further constants to be determined from the simulations.

Fitting in this manner averaged out variation in the horizontal plane, but allowed comparison with 1D theory. 2D models of the fields and potential will be discussed more in Section 4.9. As there was a great deal of horizontal variation in the image field, different regions of the beam were explored to see whether there was better agreement with the 1D case.

In the following results, image coefficients will be shown plotted for the whole beam, and for the region $-20\,\mathrm{mm} \leq x \leq -20\,\mathrm{mm}$, $-40\,\mathrm{mm} \leq y \leq -40\,\mathrm{mm}$, labelled "subset" in Figure 4.18, as well as compared to the values calculated for pencil beams in parallel plate geometry by Laslett and Baartman.

Image Term ϵ_1 (Quadrupole Term, y Dependence)

Image term ϵ_1 is plotted in Figure 4.19 for both the whole beam (left) and a rectangular subsection of the beam $-20\,\mathrm{mm} \leq x \leq -20\,\mathrm{mm}$, $-40\,\mathrm{mm} \leq y \leq -40\,\mathrm{mm}$ (right). The straight line is the value of Laslett's incoherent image term for a pencil beam in parallel plate geometry. For the subset ϵ_1 approaches zero when the aspect ratio is one. The calculated image term tends to Laslett's term at large aspect ratio, as expected. This tendency is improved for the subsection of the beam.

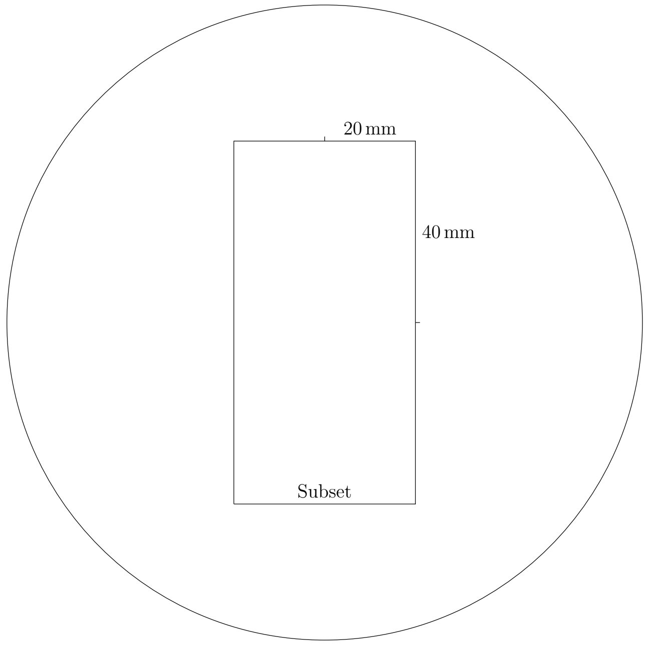

Figure 4.18: Schematic illustrating subset within beam.

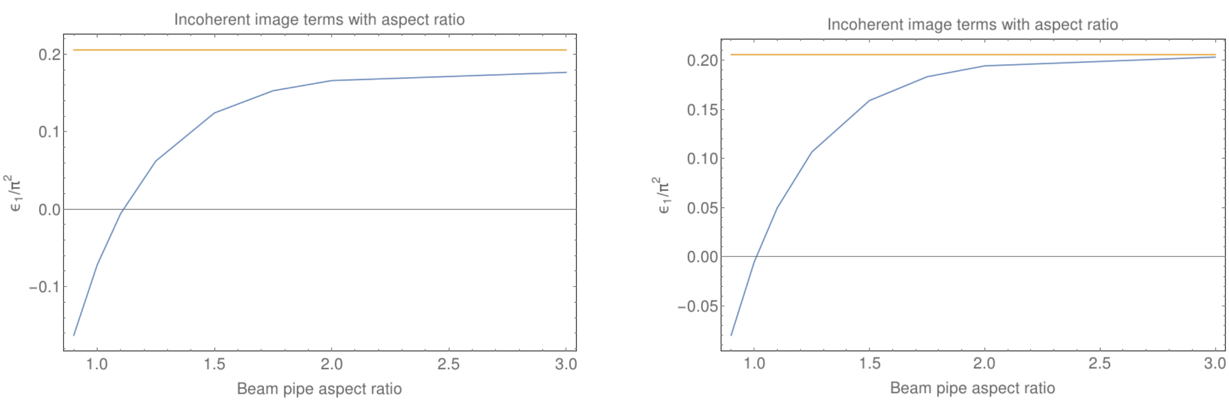

Figure 4.19: Incoherent image term for (left) the whole beam, (right) a section of beam $-20\,\mathrm{mm} \leq x \leq -20\,\mathrm{mm}$, $-40\,\mathrm{mm} \leq y \leq -40\,\mathrm{mm}$.

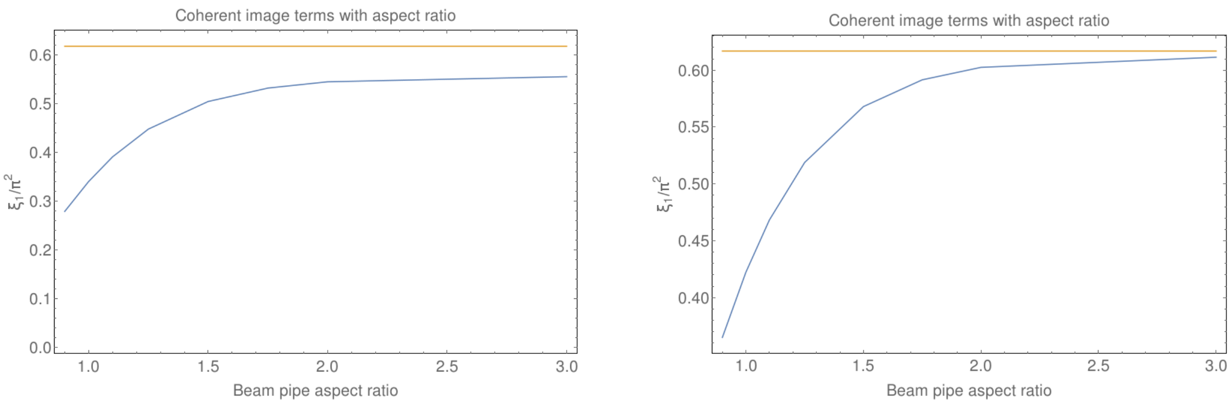

Figure 4.20: Coherent image term for (left) the whole beam, (right) a section of beam $-20\,\mathrm{mm} \leq x \leq -20\,\mathrm{mm}$, $-40\,\mathrm{mm} \leq y \leq -40\,\mathrm{mm}$.

Image Term ξ_1 ($\bar{y}$ Dependence)

Image term ξ_1 is plotted in Figure 4.20 for both the whole beam (left) and a rectangular subsection of the beam $-20\,\mathrm{mm} \leq x \leq -20\,\mathrm{mm}$, $-40\,\mathrm{mm} \leq y \leq -40\,\mathrm{mm}$ (right). The straight line is the value of Laslett's coherent image term for a pencil beam in parallel plate geometry. For the subset the coefficient is about two thirds as big when the aspect ratio is one. The values for the whole beam and subsection converge on Laslett's term but the subsection is closer.

Image Term κ_{30} ($\bar{y}^3$ dependence)

Image term κ_{30} is plotted in Figure 4.21 for both the whole beam (left) and a rectangular subsection of the beam $-20\,\mathrm{mm} \leq x \leq -20\,\mathrm{mm}$, $-40\,\mathrm{mm} \leq y \leq -40\,\mathrm{mm}$ (right). The straight line is the value of Baartman's κ_{30} image term for a pencil beam in parallel plate geometry. For the subset, the coefficient is considerably larger when the aspect ratio is one and thus may provide a larger driving term than predicted for the parallel plate case. As can be seen from the value for the whole beam there was considerable horizontal variation and the image term deviated from the 1D case.

Image Term κ_{21} (Quadrupole Term, $y\bar{y}^2$ Dependence)

Image Term κ_{21} is plotted in Figure 4.22 for both the whole beam (left) and a rectangular subsection of the beam $-20\,\mathrm{mm} \leq x \leq -20\,\mathrm{mm}$, $-40\,\mathrm{mm} \leq y \leq -40\,\mathrm{mm}$ (right). The straight line is the value of Baartman's κ_{21} image term for a pencil beam in parallel plate geometry. The value of the coefficient for the subset is larger at an aspect ratio of one so will provide a larger driving term. Horizontal variation means that the whole beam term deviates from Baartman's value, while the subsection result tends to it at large aspect ratio.

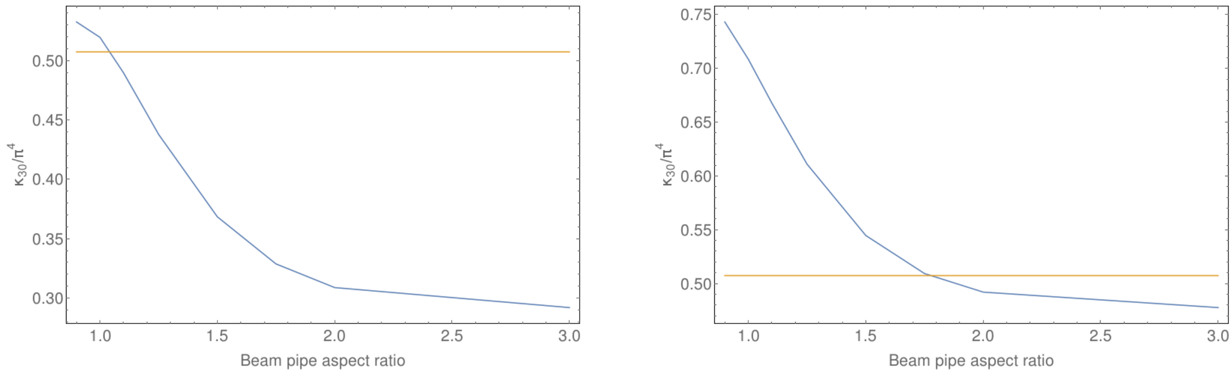

Figure 4.21: κ_{30} image term for (left) the whole beam, (right) a section of beam $-20\,\mathrm{mm} \leq x \leq -20\,\mathrm{mm}$, $-40\,\mathrm{mm} \leq y \leq -40\,\mathrm{mm}$.

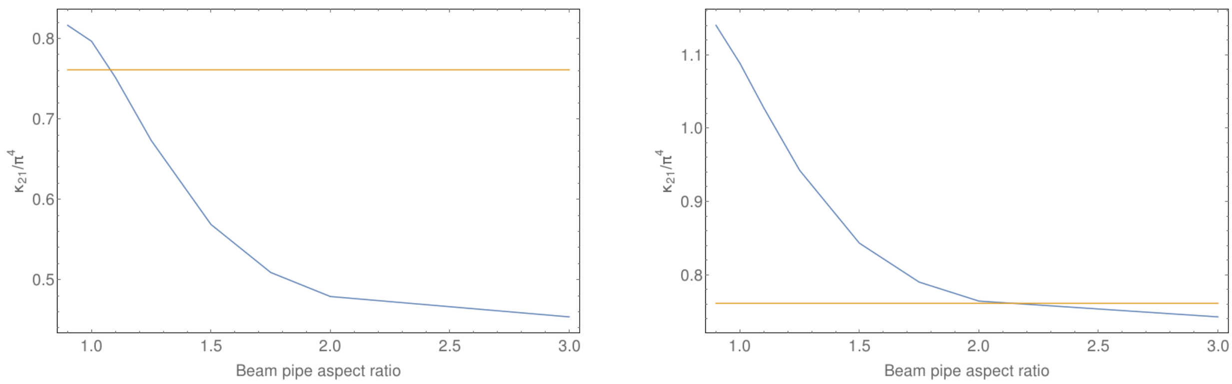

Figure 4.22: κ_{21} image term for (left) the whole beam, (right) a section of beam $-20\,\mathrm{mm} \leq x \leq -20\,\mathrm{mm}$, $-40\,\mathrm{mm} \leq y \leq -40\,\mathrm{mm}$.

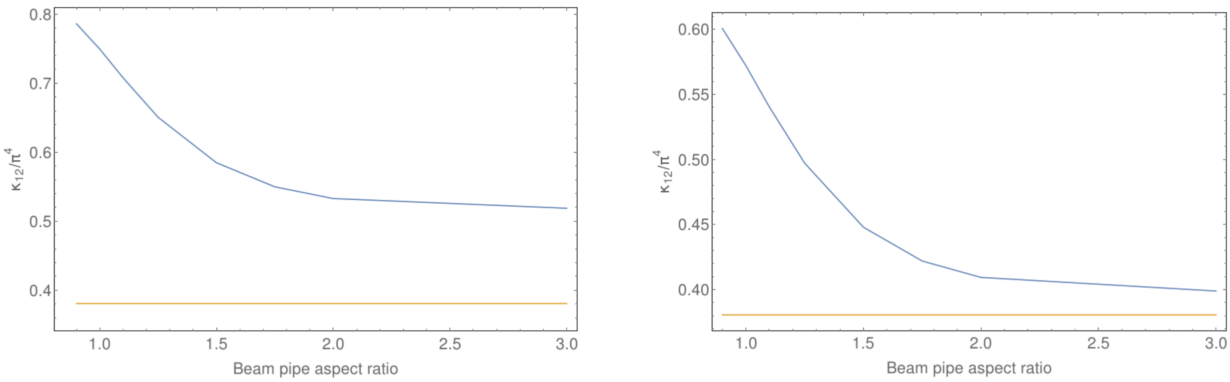

Figure 4.23: κ_{12} image term for (left) the whole beam, (right) a section of beam $-20\,\mathrm{mm} \leq x \leq -20\,\mathrm{mm}$, $-40\,\mathrm{mm} \leq y \leq -40\,\mathrm{mm}$.

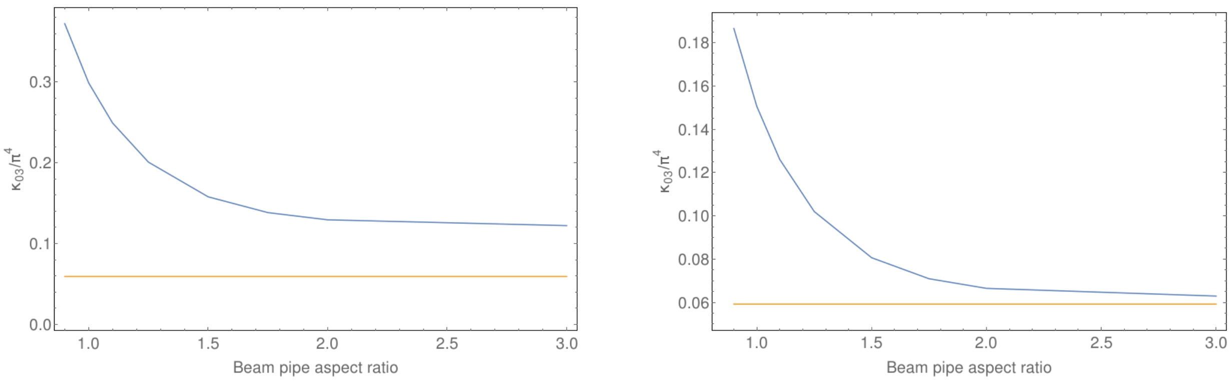

Figure 4.24: κ_{03} image term for (left) the whole beam, (right) a section of beam $-20\,\mathrm{mm} \leq x \leq -20\,\mathrm{mm}$, $-40\,\mathrm{mm} \leq y \leq -40\,\mathrm{mm}$.

Image Term κ_{12} (Sextupole Term, $y^2\bar{y}$ Dependence)

Image term κ_{12} is plotted in Figure 4.23 for both the whole beam (left) and a rectangular subsection of the beam $-20\,\mathrm{mm} \leq x \leq -20\,\mathrm{mm}$, $-40\,\mathrm{mm} \leq y \leq -40\,\mathrm{mm}$ (right). The straight line is the value of Baartman's κ_{12} image term for a pencil beam in parallel plate geometry. The value of the coefficient approaches Baartman's parallel plate value for the beam subset, while the whole beam value tends to a larger number, due to horizontal variation in the term. Again the value of the coefficent at an aspect ratio of one is considerably larger, so will provide a larger driving term.

Image Term κ_{03} (Octupole Term, y^3 Dependence)

Image term κ_{03} is plotted in Figure 4.24 for both the whole beam (left) and a rectangular subsection of the beam $-20\,\mathrm{mm} \leq x \leq -20\,\mathrm{mm}$, $-40\,\mathrm{mm} \leq y \leq -40\,\mathrm{mm}$ (right). The straight line is the value of Baartman's κ_{03} image term for a pencil beam in parallel plate geometry. The value for the beam subsection approaches Baartman at large aspect ratio, but is much larger with a square aperture.

Image coefficient	Theory Square	Theory Parallel Plate	Whole Beam Square	Whole Beam Aspect Ratio 3	Beam Section Square	Beam Section Aspect Ratio 3
ϵ_1	0	0.206	-0.0719	0.177	-0.00548	0.203
ξ_1	-	0.617	0.340	0.555	0.422	0.611
κ_{30}	-	0.507	0.520	0.292	0.719	0.478
κ_{21}	-	0.761	0.797	0.454	1.09	0.743
κ_{12}	-	0.381	0.749	0.519	0.570	0.399
κ_{03}	-	0.0592	0.299	0.122	0.151	0.063

Table 4.1: Results for image simulations in plane of beam offset, for whole beam and beam subsection $-20\,\mathrm{mm} \leq x \leq -20\,\mathrm{mm}$, $-40\,\mathrm{mm} \leq y \leq -40\,\mathrm{mm}$, compared with theory. Results are taken at 3 significant figures.

Tabulated Results for Image Terms at Aspect Ratios of 1 and 3 Compared with 1D Theory

Table 4.1 contains the data from the simulations with off-centred beams for a square aperture and an aperture with an aspect ratio of 3. These are compared with the theoretical predictions for parallel plate theory from Laslett and Baartman, and for a square aperture for the case of a centred beam.

As has been seen in the previous sections, the image fields are 2D in nature, with considerable variation across the beam. This leads to the whole beam values of the image coefficients diverging from the predictions of simple 1D theory. However if a subset of the beam along the beam axis is taken, reasonable agreement can be found with the parallel plate case at large aspect ratio.

Most interestingly, the higher order image coefficients are all significantly larger when the aperture is square. This is a significant result which provides a better estimate for the image coefficients in rectangular geometry than was previously available. These image coefficients are potential driving terms for beams with closed orbit offsets, which will be explored more in Chapter 5.

Image Analysis in Two Dimensions

In the preceding sections, 2D image fields ($E_y(x, y, \bar{x}, \bar{y})$) have been compared to analytical terms generated using pencil beams in 1D parallel plate geometry ($E_y(y, \bar{y})$). The results have shown that the image fields have 2D components.

Based on the results it seems likely that a more general 2D approach to images is possible, considering the image potential rather than fields. In fact, new symmetry is revealed in plots of the 2D image potential. For instance, Figures 4.25 and 4.26 show the potential and image potential (potential minus that of a KV beam in free space). The image potential is clearly octupolar in nature, and can be fitted accurately with a scalar and octupolar term. It is

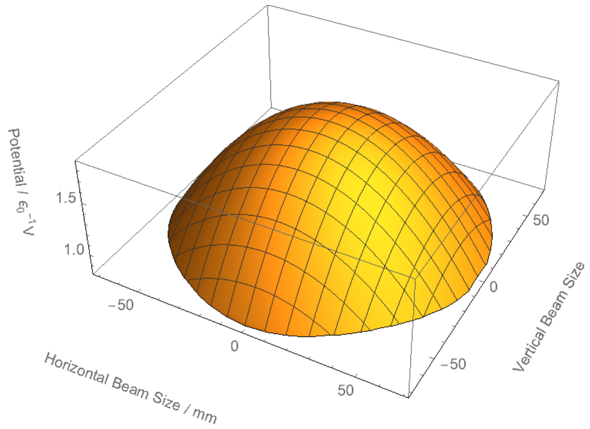

Figure 4.25: Potential of centred uniform round beam in square aperture.

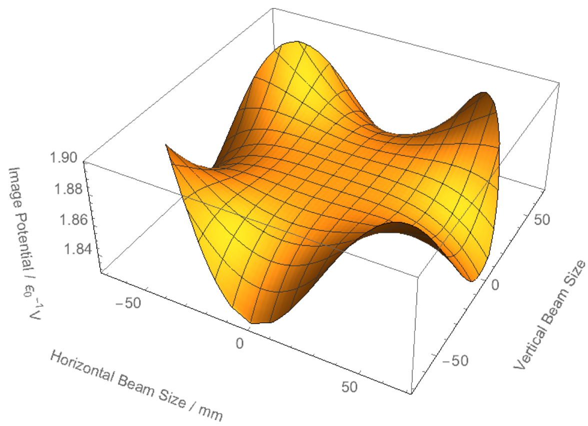

Figure 4.26: Image potential of centred uniform round beam in square aperture.

possible that the image potentials for other aspect ratios and offsets can likewise be described using the theory and terminology of expansions of the magnetic vector potential, though this will require further research to verify. It is hoped such an approach might throw more light on the 2D nature of the image coefficients.

As an initial approach to 2D, image terms were calculated for the orthogonal plane ($E_x(x, y, 0, \bar{y})$), in a manner analogous to that in Section 4.8. In this way any terms generated in the horizontal plane from a $\bar{y}$ offset were investigated. There is a horizontal component to the image field for a vertically offset beam, which will be important for some results in Chapter 5. This leads to some of the image terms for the orthogonal plane being zero and some having finite values, labelled with a subscript "T" in the following sections. While the image coefficients that are not dependent on $\bar{y}$ are finite, there is also a large value for κ_{21T}, the reason for which is as yet undetermined.

Horizontal Image Term ϵ_{1T} (Quadrupole Term, x Dependence)

The horizontal image term ε_{1T} is plotted in Figure 4.27 for both the whole beam (left) and a rectangular subsection of the beam $-40\,\text{mm} \leq x \leq -40\,\text{mm}$, $-20\,\text{mm} \leq y \leq -20\,\text{mm}$ (right). The straight line is minus the value of Laslett's coherent image term for a pencil beam in parallel plate geometry.

Horizontal Image Term κ_{21T} (Quadrupole Term, $x\bar{y}^2$ Dependence)

The horizontal image term κ_{21T} is plotted in Figure 4.28 for both the whole beam (left) and a rectangular subsection of the beam $-40\,\text{mm} \leq x \leq -40\,\text{mm}$, $-20\,\text{mm} \leq y \leq -20\,\text{mm}$ (right). These coefficients are large and negative in both the whole beam and subset case, with the largest values appearing at small aspect ratio.

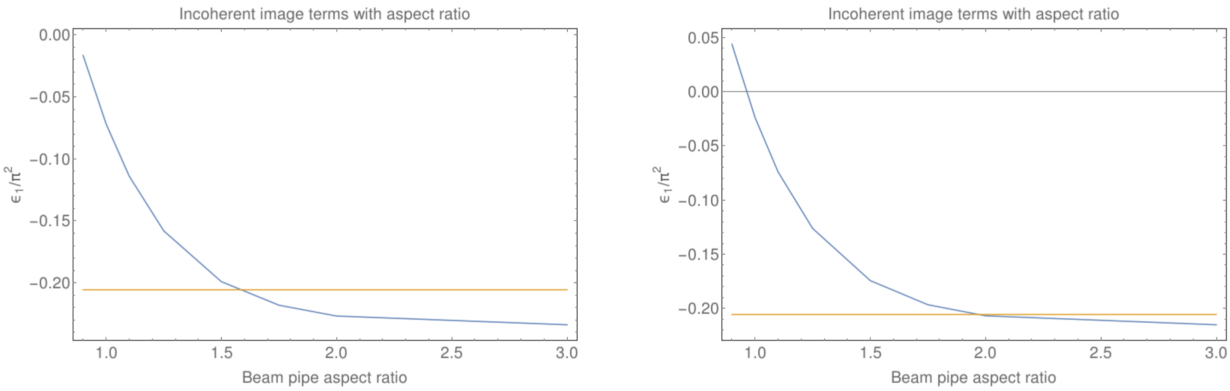

Figure 4.27: Incoherent image term ε_{1T} in the orthogonal plane for (left) the whole beam, (right) a section of beam $-40\,\mathrm{mm} \leq x \leq -40\,\mathrm{mm}$, $-20\,\mathrm{mm} \leq y \leq -20\,\mathrm{mm}$.

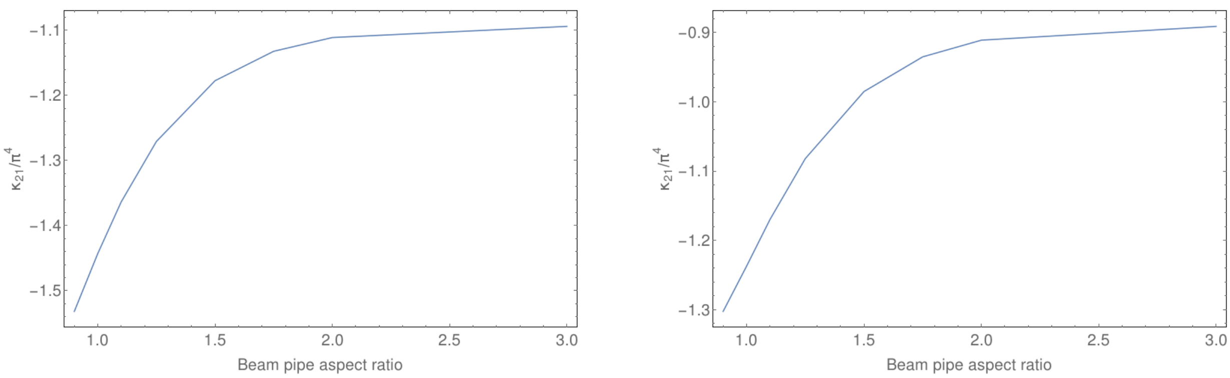

Figure 4.28: κ_{21T} image term in the orthogonal plane for (left) the whole beam, (right) a section of beam $-40\,\mathrm{mm} \leq x \leq -40\,\mathrm{mm}$, $-20\,\mathrm{mm} \leq y \leq -20\,\mathrm{mm}$.

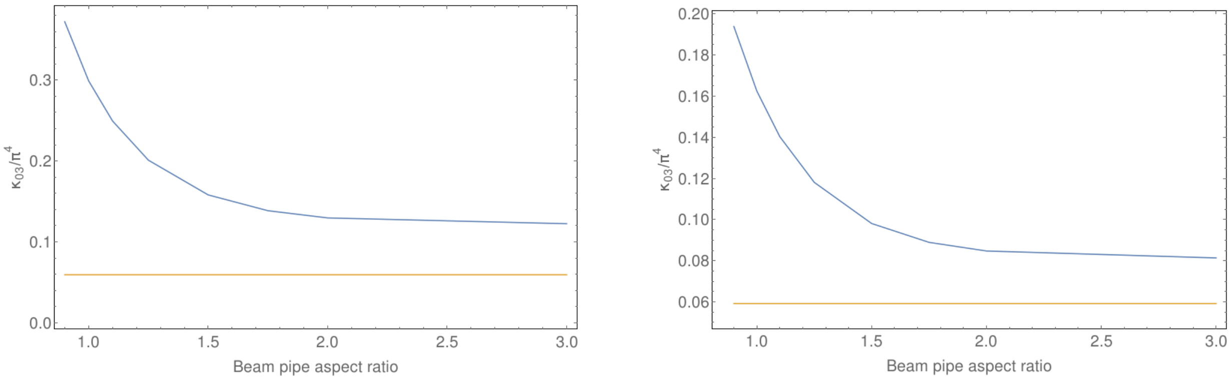

Figure 4.29: κ_{03T} image term in the orthogonal plane for (left) the whole beam, (right) a section of beam $-40\,\text{mm} \leq x \leq -40\,\text{mm}$, $-20\,\text{mm} \leq y \leq -20\,\text{mm}$.

Horizontal Image Term κ_{03T} (Octupole Term, x^3 Dependence)

The horizontal image term κ_{03T} is plotted in Figure 4.29 for both the whole beam (left) and a rectangular subsection of the beam $-40\,\text{mm} \leq x \leq -40\,\text{mm}$, $-20\,\text{mm} \leq y \leq -20\,\text{mm}$ (right). The straight line is the value of Baartman's κ_{03} image term for parallel plate geometry. In this case the image term in the orthogonal plane is very similar to that in the 1D case.

Summary

1D theory for images from pencil beams was reviewed for the cases of parallel plate geometry and, for centred beams only, rectangular apertures. 1D image coefficients were defined which were then used to study 2D beams.

Simple simulations were carried out to explore the range of validity of this 1D theory when applied to 2D round uniform beams in rectangular apertures. It was found, perhaps unsurprisingly, that at large aspect ratios, along the beam axis, such theory described image coefficients well.

The theory analysing rectangular apertures could only be applied to centred beams, but described the behaviour of the image coefficients with aspect ratio very well. This theory is promising for off-centred beams but will require further research.

Values were obtained from the simulations for the image coefficients in a square boundary, where they deviate significantly from their parallel plate values both along the beam axis and when considering the beam as a whole. This is relevant to image studies on ISIS as well as other machines with rectangular aperture beam pipes.

Values for the image coefficients in the orthogonal 1D plane were calculated from the simulations. The more complicated general 2D problem was discussed and suggestions for a full treatment of images was given.

Chapter 5

Beam Response to Image Terms

Introduction

How might image forces contribute to beam loss? Single particle models can predict the onset of particle resonances where particles move from the core of the beam to islands in phase space or are lost completely. Coherent models explain that particles respond collectively, and that the limits as calculated for single particles need to be modified. Simulations allow for such models to be explored with a good approximation of the real physics involved.

In this chapter, the effect of the image driving terms, analysed and simulated in Chapter 4, on beam motion is explored. Models of closed orbits at low and high intensities, image driving terms derived from these orbits, single particle motion using Hamiltonian resonance theory and how coherent effects modify such behaviour are covered.

Then in a series of studies, selected image driving terms are explored with particle simulations. The simulations start simply with smooth focusing lattices and constant density (KV) beams. These conditions are the closest possible to the theory using pencil beams in one dimension. Next the beam distribution is changed to a more realistic waterbag distribution and the image terms are investigated again. After this an alternating gradient (AG) lattice based on that of ISIS is used, though the vacuum vessel is kept constant. Finally an AG lattice with a conformal vacuum vessel is simulated.

In this manner a succession of models is used to explore image driven beam resonances and how they are affected as the simulations become more sophisticated and realistic.

Of course the real motion in an accelerator is three dimensional. However under certain conditions (coasting beam) a 2D model is a good description of the physics. In addition, breaking the real physics down so that it can be understood is one method for generating insight into physical processes.

Magnetic images from the lattice magnets can also contribute to collective motion, but have not been treated in the simulations.

Overview

A beam driven by single or multiple dipole errors will follow on a new closed orbit, so long as the tune is not equal to an integer. Such a closed orbit can be calculated at zero intensity, the solution of which is outlined in Section 5.3. At higher intensities, image effects can modify the closed orbit and it is much more difficult to calculate. However, particle simulations can be run to obtain the correct solutions numerically and the results of these will be shown.

Stable closed orbits will generate image forces of the type calculated and simulated in Chapter 4. These image forces can be included in one dimensional single particle Hamiltonian resonance theory. In Section 5.4 this is summarised. The Hamiltonian including higher order image coefficients is transformed to action-angle variables. The results for two image terms are expanded to show the resonant structure.

The real beam is not one dimensional or made up of independent single particles, but rather responds collectively to excitations. Section 5.5 outlines the main issues which occur when treating the collective response of the beam.

Sections 5.6 through 5.10 cover the simulation setup, then go through simulations from most simple - smooth focusing with KV beams, to waterbag beams, alternating gradient lattices and conformal vacuum vessels. In each case selected image driving terms are explored and the conditions under which the beam goes into resonance found.

Finally, there is a brief chapter summary.

Closed Orbit and Image Driving Terms

Closed Orbits at Low and High Intensity

Starting with the equation for transverse betatron motion

$$\frac{d^2y}{dt^2} + (Q\Omega)^2 y = \frac{F_y}{\gamma m_0}, \tag{5.1}$$

where y is a transverse coordinate, t is time, Q betatron tune, Ω is the revolution frequency, F_y is the external force, γ is the usual relativistic factor and m_0 is the particle rest mass. The dependent variable is changed from time t to the longitudinal coordinate s

$$\frac{d^2y}{ds^2} + \left(\frac{Q\Omega}{v_s}\right)^2 y = \frac{F_y}{v_s^2\gamma m_0} \tag{5.2}$$

$$\frac{d^2y}{ds^2} + \left(\frac{Q}{\rho_0}\right)^2 y = \frac{F_y}{p_0 v_s} \tag{5.3}$$

where v_s is the particle velocity in the longitudinal direction, ρ_0 is the accelerator mean radius and p_0 is the longitudinal relativistic momentum. Expressing F_y as the Lorentz Force

Law, $F_y = e\left[\bar{E} + \bar{v} \times \bar{B}\right]_y$, where e is the particle charge and using $\frac{p_0}{e} = B_0\rho_0$, where B_0 is the dipole strength,

$$\frac{d^2y}{ds^2} + \left(\frac{Q}{\rho_0}\right)^2 y = \frac{1}{B_0\rho_0 v_s}\left[\bar{E} + \bar{v} \times \bar{B}\right]_y. \tag{5.4}$$

The right hand side components of the force contain all of the forces that act on the particles, apart from the linear focusing force which is contained on the left hand side. The magnet term B can be associated with general magnet error terms, while E includes space charge and image driving terms.

At low intensity the E term is zero. Considering just dipole errors, with a single kick ΔB

$$\frac{d^2y}{ds^2} + \left(\frac{Q}{\rho_0}\right)^2 y = \frac{\Delta B}{B_0\rho_0}. \tag{5.5}$$

This equation is solved by the particular integral [49]

$$y = \left(\frac{\beta_s}{2|\sin \pi Q|}\frac{\Delta B}{B_0\rho_0}\right)\cos Q\theta \tag{5.6}$$

where β_s is the Twiss beta function and θ is the angular position around the accelerator. Due to the term in the denominator, $\sin \pi Q$, the closed orbit solution does not exist when Q is an integer. For the purposes of the current chapter it will be sufficient to take the closed orbit as

$$y = a_{sk}\cos Q\theta. \tag{5.7}$$

For the case of multiple kicks, the azimuthal pattern of the perturbation dominates over the tune. The solution for the closed orbit is in this case one of a number of Fourier amplitudes, with the dominant term stated here as

$$y = a_n \cos n\theta. \tag{5.8}$$

At high intensity, E is no longer zero. Direct space charge and image forces are present. Direct space charge forces do not affect the closed orbit, however image forces can do so. Re-stating Baartman's Equation from Chapter 4, (Equation 4.24), replacing $\hat{y}$ with y:

$$E_{yimage} = \frac{1}{\gamma m_0\beta^2c^2}\frac{\lambda}{\pi\varepsilon_0}\left(\epsilon_1\frac{y}{h^2} + \xi_1\frac{\bar{y}}{h^2} + \kappa_{30}\frac{\bar{y}^3}{h^4} + \kappa_{21}\frac{y\bar{y}^2}{h^4} + \kappa_{12}\frac{y^2\bar{y}}{h^4} + \kappa_{03}\frac{y^3}{h^4} + ...\right), \tag{5.9}$$

where β is the usual relativistic factor and c is the speed of light. The factor of 4 from Laslett has been multiplied out. These terms can be associated with the electric field term E from Equation 5.4. Only the purely coherent terms that contain powers of $\bar{y}$ without y will modify the closed orbit (ξ_1 and κ_{30} to third order). These and higher terms make calculation of the orbit much more complicated, as these image terms are dependent on intensity, closed orbit amplitude, and vacuum vessel geometry. However as long as the intensity is not too high the new closed orbit will be a perturbation of the low intensity case.

Simulations can be used to find the correct closed orbit, and that is what has been done in this chapter. For instance, a single dipole kick generates a discontinuity in the particle trajectories. This is illustrated in Figure 5.1 where the centroid position is plotted for a single turn every 10 turns of a 100 turn simulation, demonstrating the match of the orbit. The closed orbit was found by running the simulation several times, and successively improving the closed orbit until a good enough match was found. As the horizontal tune was set to 4.31, the closed orbit has a harmonic of 4.5 which is the nearest half integer.

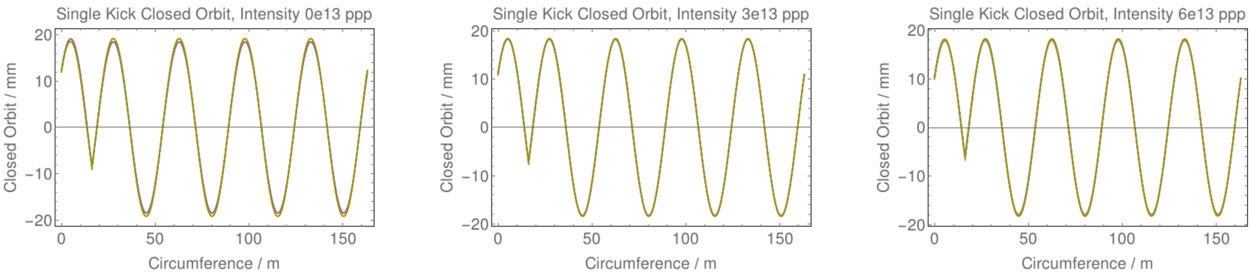

Figure 5.1: Closed orbit plotted at intensities of 0, 3 and 5.5×10^{13} ppp, over-plotted in each case every 10 turns. Simulations were with a single angular kick at the beginning of the second superperiod.

Alternatively a closed orbit can be created with a series of kicks, to create a specific azimuthal harmonic. An example is shown in Figure 5.2 where a small kick is applied at every element to create a 13$^{\text{th}}$ harmonic closed orbit. Again the orbits are over-plotted every 10 turns for 100 turns. 3 intensities are shown: 0, 5 and 7.6×10^{13} ppp.

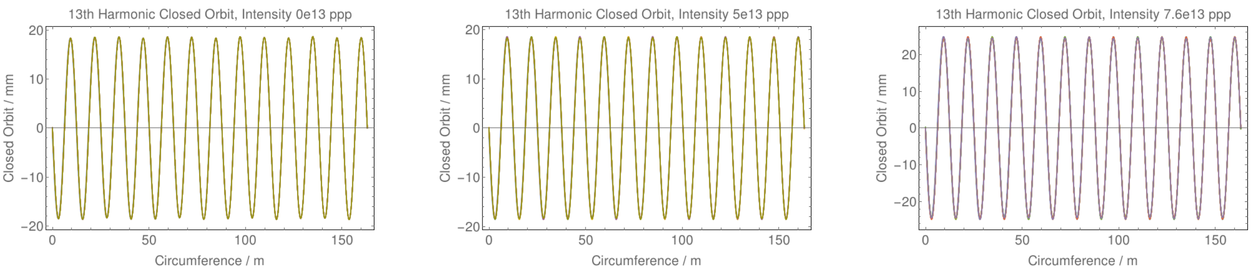

Figure 5.2: Closed orbit plotted at intensities of 0, 5 and 7.6×10^{13} ppp, over-plotted in each case every 10 turns. Simulations were with a distributed angular kick to produce a 13$^{\text{th}}$ harmonic closed orbit.

Image Driving Terms

Once the existence of a high intensity closed orbit has been established, the effects of images induced by this closed orbit can then be assessed. Rewriting Equation 5.4, with respect to the established closed orbit, as

$$y'' + ky = F_D + F_I \tag{5.10}$$

where the prime indicates differentiation with respect to s, k is the smooth focusing strength $(Q/\rho_0)^2$, F_D contains the direct space charge terms and F_I the indirect (i.e. image) terms. For a KV beam, F_D is linear inside the beam, while for other distributions it is non-linear. Both F_D and F_I are included in the simulations that follow, however it is the effect of F_I that is of interest here.

Taking Equation 5.9, including the closed orbit $\bar{y} = a_n \cos n\theta$ and separating out terms leads to the results listed in Table 5.1. The coefficients were defined and calculated in Chapter 4. The order of the driving term comes from the power of y in the expression. The closed orbit harmonic is n. How these terms are expanded out will lead to the resonant form in the next section.

Coefficient	Image Term	Order	Harmonic
ξ_1/h^2	$\bar{y}$	Dipole	$\cos n\theta$
κ_{30}/h^4	$\bar{y}^3$	Dipole	$\cos^3 n\theta$
ϵ_1/h^2	y	Quadrupole	None
κ_{21}/h^4	$y\bar{y}^2$	Quadrupole	$\cos^2 n\theta$
κ_{12}/h^4	$y^2\bar{y}$	Sextupole	$\cos n\theta$
κ_{30}/h^4	y^3	Octupole	None

Table 5.1: Image driving terms from Equation 4.24.

There are equivalent driving terms in the orthogonal plane, where only ϵ_{1T}, κ_{21T} and κ_{30T} were found to have non-zero values. When the lattice is not smooth focusing, e.g. alternating gradient, and especially when the vacuum vessel is conformal, there are additional driving terms from the variation of the beam size with respect to the boundary.

Single Particle Hamiltonian Including Image Driving Terms

Once created, closed orbits will create image forces that act back on the beam. As discussed, these will modify the closed orbits themselves, however this will be treated as a small perturbation here. Therefore the single particle motion about the closed orbit may be treated taking the closed orbit motion itself as constant. Direct space charge forces will modify the particle motion but not the closed orbit.

The one dimensional single particle Hamiltonian can be written [50]

$$H(y, P_y, s) = \frac{1}{2}P_y^2 + \frac{1}{2}ky^2 + V_D + V_I \tag{5.11}$$

where H is the Hamiltonian, P_y is the canonical momentum, V_D and V_I are potentials representing F_D and F_I and the other variables are as above.

Writing the indirect space charge forces in potential form,

$$\begin{aligned} V_I = \frac{1}{\gamma m_0 \beta^2 c^2} \frac{\lambda}{\pi\varepsilon_0} \Bigg[& -\frac{\pi^2}{24h^2}\left(y^2 + 6y\bar{y} + 6\bar{y}^2\right) \\ & -\frac{\pi^4}{11520h^4}\left(7y^4 + 60y^3\bar{y} + 180y^2\bar{y}^2 + 240y\bar{y}^3 + 120\bar{y}^4\right) + \dots \Bigg] \end{aligned} \tag{5.12}$$

These are the terms for Baartman's image term equation, plus two terms that disappear upon differentiation. Baartman's equation can also be written in this form:

$$V_I = \frac{1}{\gamma m_0 \beta^2 c^2} \frac{\lambda}{\pi \varepsilon_0} \left[\epsilon_1 \frac{y^2}{2h^2} + \xi_1 \frac{y\bar{y}}{h^2} + \kappa_{30} \frac{y\bar{y}^3}{h^4} + \right. \\ \left. \kappa_{21} \frac{y^2\bar{y}^2}{2h^4} + \kappa_{12} \frac{y^3\bar{y}}{3h^4} + \kappa_{03} \frac{y^4}{4h^4} + \ldots \right] \quad (5.13)$$

Transform the Hamiltonian to action-angle coordinates

$$y = \sqrt{\frac{2J}{\omega}} \sin \phi \quad (5.14)$$

and substitute the closed orbit solution as above

$$\bar{y} = a_n \cos n\theta. \quad (5.15)$$

To obtain

$$H(J, \omega) = \omega J + V_I(J, \theta) + V_D(J). \quad (5.16)$$

Two of the image terms have been studied in particular in the simulations to follow, κ_{12} and κ_{21}. They are explored more fully here.

Hamiltonian Including κ_{12}

The κ_{12} image term can be inserted into the Hamiltonian as $T_{12} y^3 \bar{y}$ where T_{12} is a constant absorbing κ_{12} and other constant terms. Changing y to action-angle variables and substituting for $\bar{y}$:

$$H = \omega J + T_{12} \left(\frac{2J}{\omega} \right)^{\frac{3}{2}} \sin^3 \phi \; a_n \cos n\theta + V_0(J) \quad (5.17)$$

$V_0(J)$ is a non-linear term in J due to direct space charge and other image terms.

$$H = \omega J + a_n T_{12} \left(\frac{2J}{\omega} \right)^{\frac{3}{2}} \left(\frac{3}{4} \sin \phi - \frac{1}{4} \sin 3\phi \right) \cos n\theta + V_0(J) \quad (5.18)$$

$$H = \omega J + a_n T_{12} \left(\frac{2J}{\omega} \right)^{\frac{3}{2}} \left(\frac{3}{4} \sin \phi \cos n\theta - \frac{1}{4} \sin 3\phi \cos n\theta \right) + V_0(J) \quad (5.19)$$

$$H = \omega J + a_n T_{12} \left(\frac{2J}{\omega} \right)^{\frac{3}{2}} \left(\frac{3}{8} \left(\sin(\phi - n\theta) + \sin(\phi + n\theta) \right) \right. \\ \left. - \frac{1}{8} \left(\sin(3\phi - n\theta) + \sin(3\phi + n\theta) \right) \right) + V_0(J) \quad (5.20)$$

This suggests that the κ_{12} term has potential resonances at $Q = n$ and $3Q = n$.

Hamiltonian Including κ_{21}

Similarly the κ_{21} image term can be inserted as $T_{21}y\bar{y}^2$ where T_{21} is a constant absorbing κ_{21} and other constant terms. Changing y to action-angle variables and substituting for $\bar{y}$:

$$H = \omega J + T_{21}\,\frac{2J}{\omega}\sin^2\phi\; a_n^2\cos^2 n\theta + V_0(J) \tag{5.21}$$

Expand both trigonometric terms

$$H = \omega J + T_{21}a_n^2\frac{2J}{\omega}\;\frac{1-\cos 2\phi}{2}\;\frac{\cos 2n\theta + 1}{2} + V_0(J) \tag{5.22}$$

$$H = \omega J + T_{21}a_n^2\frac{J}{2\omega}\left(1 + \cos 2n\theta - \cos 2\phi - \cos 2\phi\cos 2n\theta\right) + V_0(J) \tag{5.23}$$

Of the terms in the bracket, the 1$^{\text{st}}$ is a tune shift and the 2$^{\text{nd}}$ and 3$^{\text{rd}}$ average to zero. The last term is dominant.

$$\cos 2\phi\cos 2n\theta = \frac{1}{2}\left(\cos(2\phi - 2n\theta) + \cos(2\phi + 2n\theta)\right) \tag{5.24}$$

This term suggests that there is a potential resonance due to the κ_{21} term at $2Q = 2n$.

Coherent Response of the Beam

Single particle analysis is an incomplete description of the situation in the beam as the space charge forces mean that the beam responds collectively to excitations. Collective beam response has been studied extensively. In the seminal paper by Kapchinskij and Vladimirskij [51], a stationary distribution was identified (the "KV" distribution) which has linear space charge forces. This was used to calculate an envelope equation for the beam and limits for high space charge beams.

Subsequent developments extended the analysis to 2D anisotropic beams. These various studies showed that it was not the incoherent tune of the beam that mattered for resonance but the space charge modified coherent tune, providing a coherent advantage over the incoherent case [52, 53].

For different beam moments the beam would beat in a manner to oppose the space charge forces. For instance in the half integer case, for small tune split there are two modes, "breathing" and "quadrupole", in and out of phase respectively, with different coherent tune shifts depending on the mode. The situation becomes much more complicated for higher order resonances. The conclusion is that it is the coherent frequencies, shifted by intensity, that matter for onset of resonance. Hoffman addressed this with a modified resonance formula

$$\omega = nQ_H + mQ_V + \Delta\omega = N, \tag{5.25}$$

where n and m are integers, $n+m$ is the order of the resonance, $\Delta\omega$ is the coherent mode shift and N is the azimuthal harmonic. In the simulation studies in this chapter, resonances were identified by fixing the lattice tune and scanning the intensity, thus shifting the coherent mode.

Baartman has summarised the results in a useful paper which also addressed the image driving terms discussed here [44]. Additionally he showed that for direct space charge, incoherent motion is not affected by integer driving terms, as the dipole forces disappear in the beam frame on a closed orbit. However image forces may affect the beam as they break the symmetry centred on the beam.

Machida used simulations to show that the analysis based on collective effects was a good description of the physics [54].

Coherent theory assumes that beam emittance is conserved and therefore does not contain the mechanics of beam re-distribution. On the other hand, single particle mechanics must be modified to take account of the modified forces and frequencies provided by coherent motion. Neither approach is a complete description of the physics. Self-consistent multi-particle simulations are one way to deal with both of these complexities at the same time, and will be explored further in the rest of the chapter.

Simulation Setup

Resonances were investigated using self-consistent PIC simulations of a coasting beam through a smooth focusing lattice, or one based on the ISIS AG lattice. The simulations are as detailed in Chapter 3. Simulations were generally run for 100 turns, which was sufficient for high intensity resonant behaviour to manifest. Distributions of 5×10^4 macroparticles were RMS matched to the envelope and closed orbit on the first turn. Coherent moments, single particle tunes, phase space distributions and losses (particles which exceeded the aperture) were all recorded. Dipole driving terms were applied singly or harmonically as detailed above.

Typically a particular closed orbit term was selected for study, then coherent resonances looked for in appropriate moments as expected from resonance theory. This gave a clear indication of the presence and action of an image driving term. Single particle phase space gave a useful indication of terms driving emittance growth. The importance of a given driving term was assessed by the magnitude of oscillation it caused to the relevant moment, emittance growth and particle losses.

These simulations are an approximation to the 3D, fast cycling, bunched, accelerating situation at ISIS. However they allow relevant 2D physics to be observed which contributes to greater knowledge of the global picture. The work here will be complemented by more realistic simulations in the future.

For each higher order image term that was investigated the procedure was the same:

1. Start with a zero intensity beam
2. Move the tune of the lattice to a suitable point so that a higher order driving term

might be excited

3. Kick the beam so that the required closed orbit harmonic was created in order to drive a resonance

4. Match the new closed orbit

5. Increase the beam intensity until the coherent beam frequency interacted with the image driving term

6. With each intensity change, re-match the RMS envelope and closed orbit

Closed orbits were created as large as possible ∼20 mm to create large image driving terms, while still allowing the beam to respond without immediately causing beam loss.

In each results section the simulation parameters are tabulated to allow reconstruction of the various results.

Smooth Focusing Simulations

In this section, simulations were run with the simplest 2D parameters. A smooth focusing lattice (constant beta functions), and constant aperture vacuum vessel meant that image driving terms were comparable to those obtained in Chapter 4. In the first part, a KV beam distribution was used which has linear space charge forces. In a KV beam, the particles all have the same incoherent tune. However the beam responds very strongly to coherent resonance - it is less stable than more realistic distributions. Later a waterbag (WB) beam was introduced, which has a tune spread between the particles, and was more stable to coherent excitation.

A beam of radius 50 mm (100% emittance 300 π mm mrad) was generated randomly at the start of each simulation. The vacuum vessel was a constant square aperture with a half-aperture of 100 mm. These and other smooth focusing simulation parameters are included in Table 5.2.

Lattice type	Smooth focusing
No. elements	880
Circumference	163.36 m
No. macros	50000
100% emittance (ε_H, ε_V)	(300, 300)
Vacuum vessel	± 100 mm (Square)
Turns simulated	100

Table 5.2: Simulation parameter list, smooth focusing.

Intensity at resonance	7.6×10^{13} ppp
Beam distribution	KV
Lattice tunes (Q_H, Q_V)	(4.6, 3.83)
Kick type	Horizontal 13$^{\text{th}}$ harmonic
Kick strength	0.75 mrad (peak)
Closed orbit match at resonance (x, x', y, y')	(0, -12.3, 0, 0)
Envelope match at resonance $(\beta_H, \alpha_H, \beta_V, \alpha_V)$	(6.0, 0, 7.5, 0)
Max closed orbit	24.9 mm

Table 5.3: Simulation parameter list, smooth focusing, KV beam, κ_{12} driven with 13$^{\text{th}}$ harmonic closed orbit.

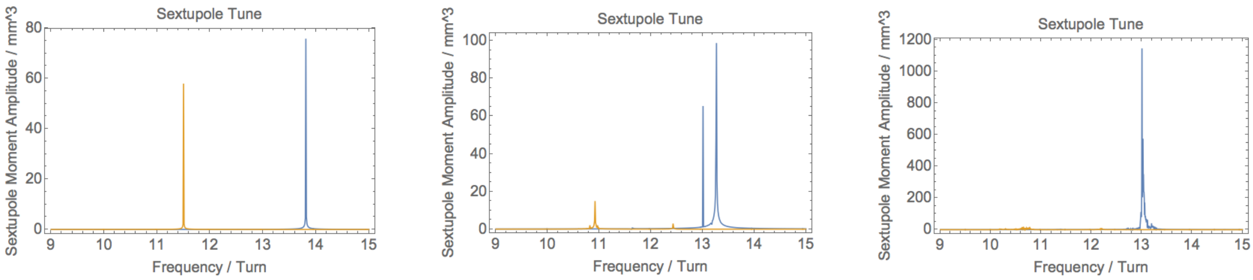

Figure 5.3: Sextupole moment spectra with a 13$^{\text{th}}$ harmonic closed orbit driving the κ_{12} higher order image term, at intensities of 0, 5 and 7.6×10^{13} ppp. Blue: horizontal, yellow: vertical.

KV Beams

Investigation of κ_{12} Image Term, Driven with 13$^{\text{th}}$ Harmonic Closed Orbit

Beam behaviour due to the κ_{12} image term was investigated. This term has the form $y^2\bar{y}$. It is a sextupole term. The Hamiltonian in action-angle coordinates suggests that there is a resonance at $3Q_H = n$, where n is the azimuthal harmonic of the driving term. A 13$^{\text{th}}$ harmonic driving term was created and the tune of the lattice moved to 4.6. The closed orbit was shown in Figure 5.2. These and other simulation parameters are listed in Table 5.3. Beam intensity was then increased, so that the coherent sextupole tune was depressed towards resonance.

The sextupole moment frequency of the beam is shown in Figure 5.3 for three intensities, 0, 5 and 7.6×10^{13} ppp. With zero intensity there is no driving term as images are intensity dependent. At 5×10^{13} ppp the driving term is present in the beam spectra, but the beam moment does not yet interact with it. At 7.6×10^{13} ppp the beam is at resonance caused by the image driving term. Resonance is also indicated by the vertical scale of the plot, where the sextupole moment amplitude has increased significantly.

Figure 5.4 shows horizontal phase space on turns 10, 20 and 30 for the case when the intensity is 7.6×10^{13} ppp. There is clearly a three fold structure in phase space indicating a third order resonance.

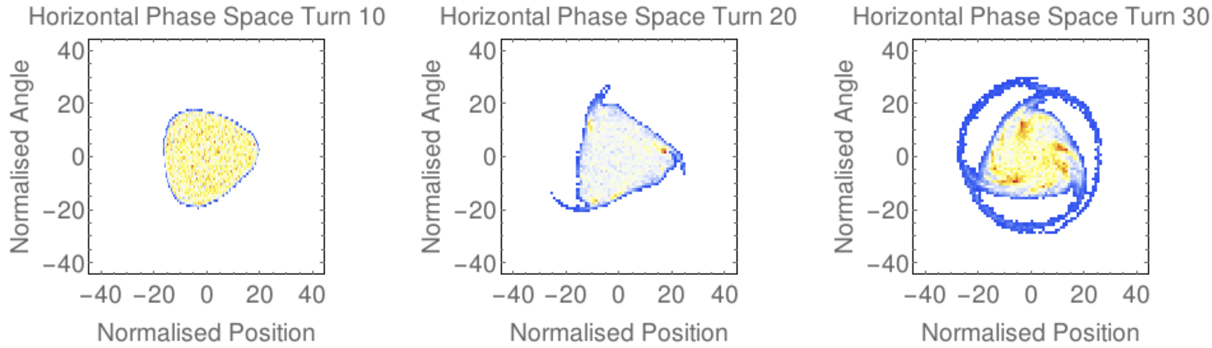

Figure 5.4: Horizontal phase space density plots on turns 10, 20 and 30 at an intensity of 7.6×10^{13} ppp, for a KV beam in a smooth focusing lattice driven with a 13^{th} harmonic closed orbit.

An image driven resonance was located as predicted at $3Q_H = 13$, modified by the coherent beam motion. This example was artificial as it involved modifying the tune away from the nominal ISIS value, however it demonstrated a clear third order resonance. The driving term was also observed to weaken dramatically as the vacuum vessel size was increased. This image term is not a concern for ISIS operations or upgrades, however terms with lower azimuthal frequency, which occur nearer to the nominal tune, may be of concern.

Investigation of κ_{21} Image Term, Driven with Single Kick, 2Q = 9^{th} Harmonic Driving Term

Beam behaviour due to the κ_{21} image term was investigated. This term has the form $y\bar{y}^2$. It is a quadrupole term. The Hamiltonian in action-angle coordinates suggests that there is a resonance at $2Q_H = 2n$, where n is the azimuthal harmonic of the driving term. A closed orbit driven by a single kick was used to generate a 4.5 harmonic closed orbit, shown in Figure 5.1. The horizontal zero intensity tune was moved above the half integer, in this case to 4.65. This and other simulation parameters are listed in Table 5.4.

Figure 5.5 shows the quadrupole moment spectra for intensities of 0, 3 and 5.5×10^{13} ppp.

Intensity at resonance	5.5×10^{13} ppp
Beam distribution	KV
Lattice tunes (Q_H, Q_V)	(4.65, 3.83)
Kick type	Horizontal single kick
Kick strength	6.0 mrad
Closed orbit match at resonance (x, x', y, y')	(10.0, 2.67, 0, 0)
Envelope match at resonance $(\beta_H, \alpha_H, \beta_V, \alpha_V)$	(4.98, 0, 7.23, 0)
Max closed orbit	18.3 mm

Table 5.4: Simulation parameter list, smooth focusing, KV beam, κ_{21} driven with single kick, 2Q = 9^{th} harmonic driving term.

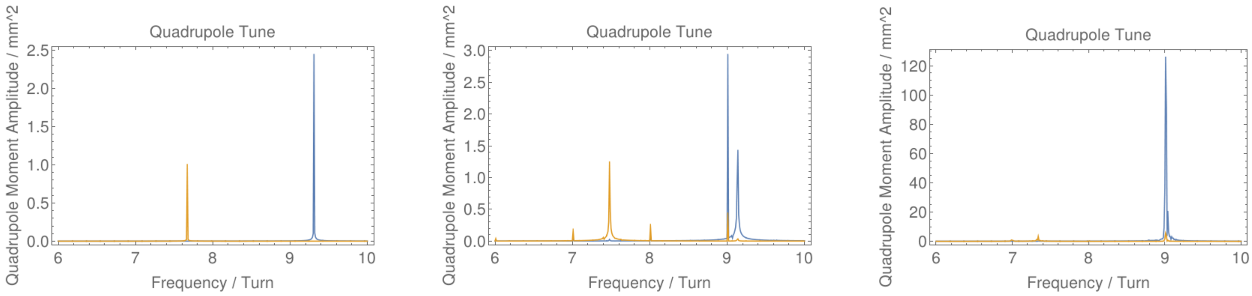

Figure 5.5: Quadrupole moment spectra with a closed orbit excited by a single kick driving the κ_{21} higher order image term at 9^{th} harmonic, at intensities of 0, 3 and 5.5×10^{13} ppp. Blue: horizontal, yellow: vertical.

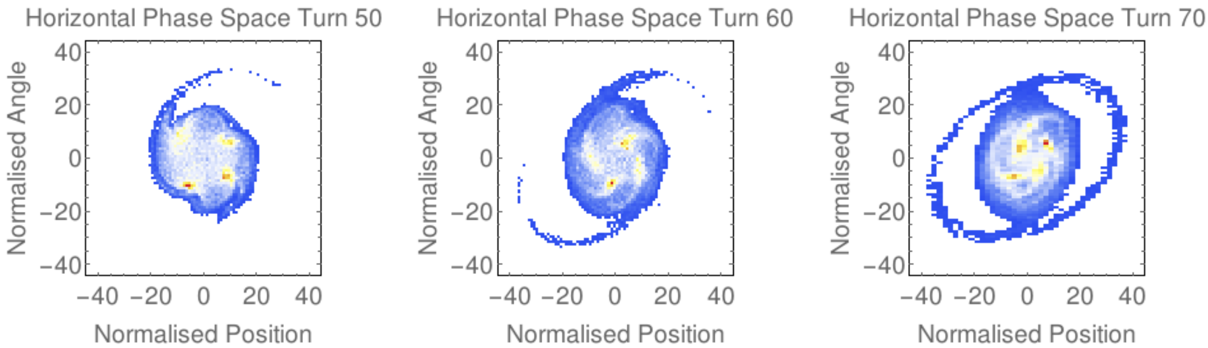

Figure 5.6: Horizontal phase space on turns 50, 60 and 70 for a beam excited by a single kick driving the κ_{21} higher order image term at 9^{th} harmonic, at an intensity of 5.5×10^{13} ppp.

At zero intensity there is no image driving term. At higher intensities the effect of the intensity dependent driving term has appeared at $2Q_H = 9$ and at an intensity of 5.5×10^{13} ppp the beam has reached resonance, as is indicated by the magnitude of the frequency component.

Figure 5.6 shows horizontal phase space on turns 50, 60 and 70 for the simulation with intensity 5.5×10^{13} ppp. The formation of a half integer (quadrupole) resonance structure is clearly visible. There are also signs of an octupole resonance structure, though this has not been explored further.

An image driven resonance was located as predicted at $2Q_H = 2n$, modified by the coherent beam motion. This example was artificial as it involved modifying the tune away from the nominal ISIS value, however it demonstrated a clear second order resonance. The driving term was also observed to weaken dramatically as the vacuum vessel size was increased. This image term is not of concern for ISIS.

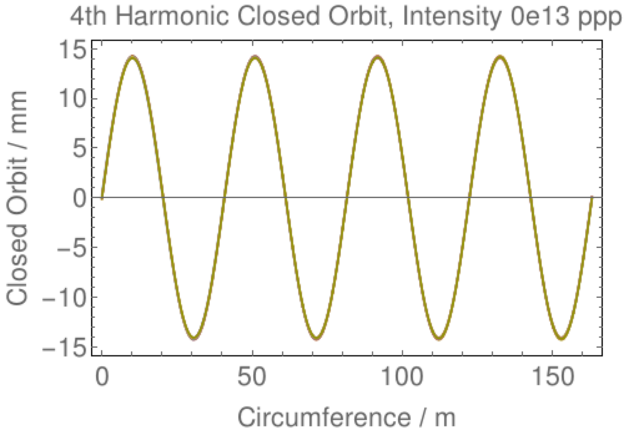

Figure 5.7: Closed orbit plotted at intensity of 0×10^{13} ppp, overplotted in each case every 10 turns. Simulations were with a distributed angular kick to produce a 4$^{\text{th}}$ harmonic closed orbit.

Intensity at resonance	9.0×10^{13} ppp
Beam distribution	KV
Lattice tunes (Q_H, Q_V)	(4.31, 3.83)
Kick type	Horizontal 4$^{\text{th}}$ harmonic
Kick strength	0.01 mrad (peak)
Closed orbit match at resonance (x, x', y, y')	(0, 2.88, 0, 0)
Envelope match at resonance $(\beta_H, \alpha_H, \beta_V, \alpha_V)$	(6.44, 0, 7.52, 0)
Max closed orbit	19.3 mm

Table 5.5: Simulation parameter list, smooth focusing, KV beam driven with 4$^{\text{th}}$ harmonic closed orbit.

Investigation of Effects of 4$^{\text{th}}$ Harmonic Closed Orbit at ISIS Nominal Tunes

Many different image driving terms can be excited by the 4$^{\text{th}}$ harmonic closed orbit. It was expected that half integer resonance would be important. The single particle behaviour for half integer is identical to Section 5.8.2, except that the closed orbit is now of the form $n = 4$ and the resonance condition becomes $2Q_H = 8$. The matched closed orbit is shown in Figure 5.7, overplotted every 10 turns, at zero intensity. The closed orbit at other intensities was very similar.

Accordingly a 4$^{\text{th}}$ horizontal closed orbit was set up, using ISIS nominal tunes (4.31, 3.83). The beam intensity was scanned until resonance was reached, in this case at 9×10^{13} ppp. Values for the simulation parameters are contained in Tables 5.2 and 5.5.

The quadrupole frequency measured from the beam is plotted in Figure 5.8 at intensities of 0, 5 and 9×10^{13} ppp. However the beam had started to redistribute before the quadrupole moment reached resonance. More investigations were required.

Figure 5.9 shows the FFT of the sextupole moment of the beam at the same intensities. From the spectra it seems that the beam encountered a sextupole resonance located at

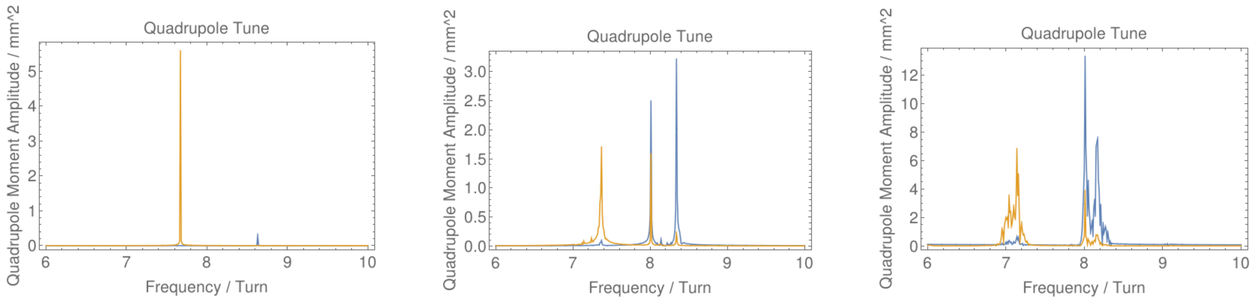

Figure 5.8: Quadrupole moment spectra with a 4^{th} harmonic closed orbit driving the κ_{21} higher order image term at 8^{th} harmonic, at intensities of 0, 5 and 9×10^{13} ppp. Blue: horizontal, yellow: vertical.

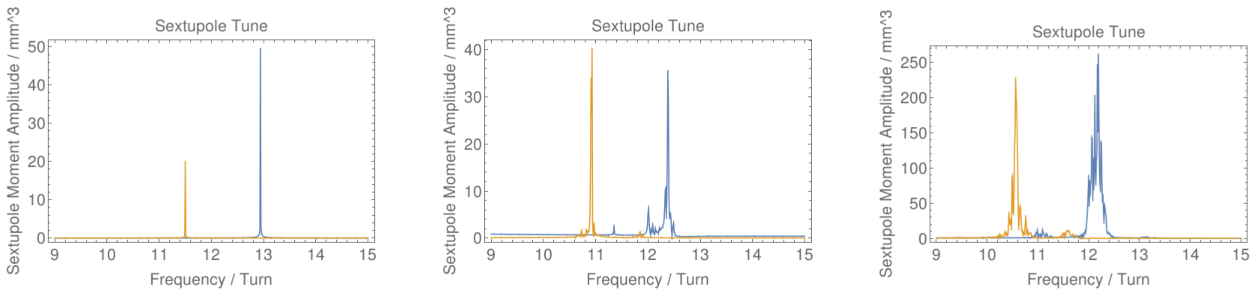

Figure 5.9: Sextupole moment spectra with a 4^{th} harmonic closed orbit driving the κ_{30} higher order image term at 12^{th} harmonic, at intensities of 0, 5 and 9×10^{13} ppp. Blue: horizontal, yellow: vertical.

$3Q_H = 12$ at an intensity of 9×10^{13} ppp. This example brings out some of the complexities of image driven resonances. It is not possible to just drive one - a closed orbit will drive multiple orders of image terms. In this case, the quadrupole term was dominated by a stronger sextupole term.

Figure 5.10 shows horizontal phase space on turns 20, 30 and 40 for the simulation run with an intensity of 9×10^{13} ppp. The resonance has an integer structure. For direct space charge, integer resonances cannot occur before the coherent limit is reached. There was a strong integer driving term at $Q_H = 4$, but the coherent dipole frequency was at 4.27, well above the integer. However, image forces break the symmetry for the integer resonance, which may mean that an incoherent resonance occurred here. The single particle tune footprint (incoherent tunes) is shown in Figure 5.11. The beam has redistributed and the tunes no longer have a single incoherent value. Some of them lie on top of the $Q_H = 4$ resonance line.

What was less clear was why a sextupole resonance would be associated with an integer phase space structure. There was an integer resonance component to the sextupole driving term however this would have resonated at $Q_H = n$ not $3Q_H = 3n$ which appeared to be the case here. What was driving a harmonic at $n = 12$ was also unclear though it could have been a modulation of $2Q_H = 8$ and $n = 4$. Many other effects are possible, including but not limited to, coupling and other higher order terms.

A simulation with nominal ISIS tunes and a 4^{th} harmonic closed orbit exhibited beam

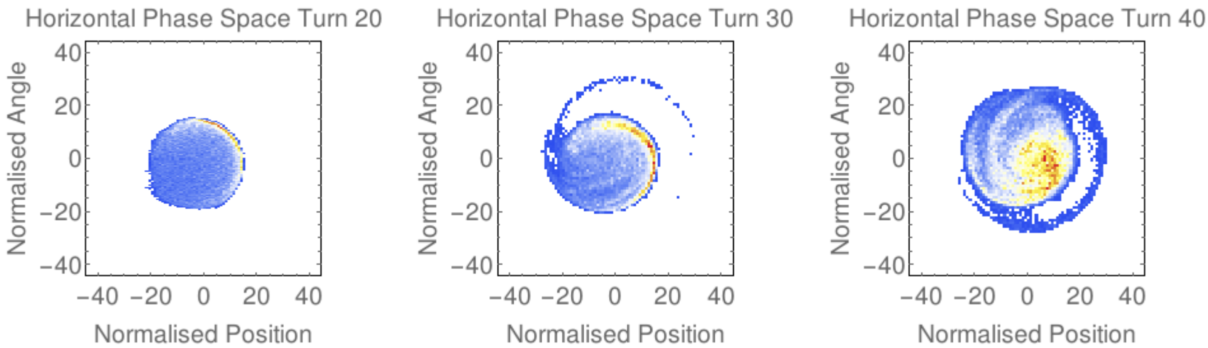

Figure 5.10: Horizontal phase space on turns 20, 30 and 40 at an intensity of 9×10^{13} ppp, for a smooth focusing, KV simulation driven with a 4$^{\text{th}}$ harmonic closed orbit.

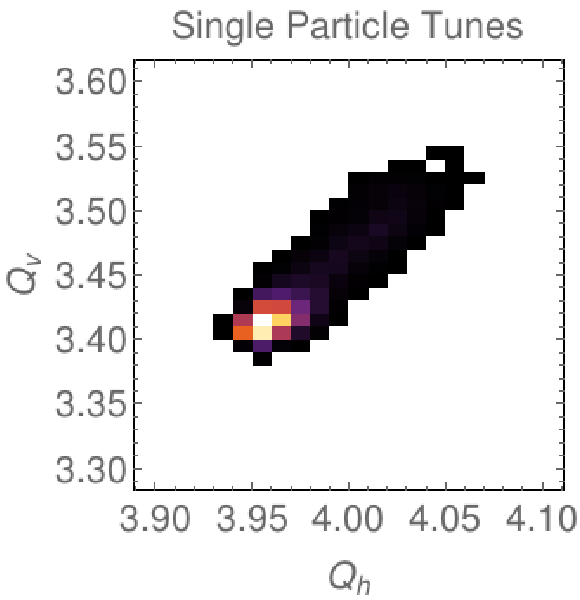

Figure 5.11: Single particle tune footprint for ISIS nominal tunes and 4$^{\text{th}}$ harmonic closed orbit, at an intensity of 9×10^{13} ppp.

redistribution and emittance growth consistent with an integer resonance. The precise cause of the resonance is unclear, though incoherent dipole and coherent sextupole are possibilities, amongst others. This resonance should be investigated further as it is potentially of concern for ISIS, though the closed orbits on ISIS are much reduced.

Investigation of Effects of 4$^{\text{th}}$ Harmonic Vertical Closed Orbit at ISIS Nominal Tunes

This section is similar to the last, except that it explores the effect of a vertical 4$^{\text{th}}$ harmonic closed orbit. The existence of a higher order image term in the orthogonal plane to that of the beam offset was established with simulations in Chapter 4. The image term was called κ_{21T} though it was applied in the vertical plane here. It was expected it would lead to a horizontal resonance. The image term is $y\bar{y}^2$ and it is a quadrupole term. The Hamiltonian for such a term is identical to that in Section 5.8.3. The expected resonance is of the form $2Q_H = 2n = 8$. The matched closed orbit obtained for these simulations is shown in Figure 5.14 for the zero intensity case, overplotted every 10 turns.

Tables 5.2 and 5.6 contain the simulation parameters for these results.

Figure 5.13 shows plots of the FFT of the horizontal quadrupole moment of the beam at intensities of 0, 9 and 12×10^{13} ppp. At zero intensity the effect of the image driving term is not visible. It is visible at higher intensities and the beam is on resonance at an intensity of 12×10^{13} ppp.

Figure 5.14 shows horizontal phase space on turns 20, 30 and 40 for the simulation with intensity 12×10^{13} ppp. A half integer resonance is clearly observed. There is some additional octopole structure which has not been investigated further at this stage.

In this case the expected horizontal half integer resonance did occur as a result of the vertical harmonic closed orbit. While the closed orbits in the simulation are large, this image driving term is expected to be present at ISIS and should be investigated further.

Intensity at resonance	12.0×10^{13} ppp
Beam distribution	KV
Lattice tunes (Q_H, Q_V)	(4.31, 3.83)
Kick type	Vertical 4$^{\text{th}}$ harmonic
Kick strength	0.01 mrad (peak)
Closed orbit match at resonance (x, x', y, y')	(0, 0, 0, -2.6)
Envelope match at resonance (β_H, α_H, β_V, α_V)	(7.85, 0, 8.11, 0)
Max closed orbit	17.1 mm

Table 5.6: Simulation parameter list, smooth focusing, KV beam driven with 4$^{\text{th}}$ harmonic vertical closed orbit.

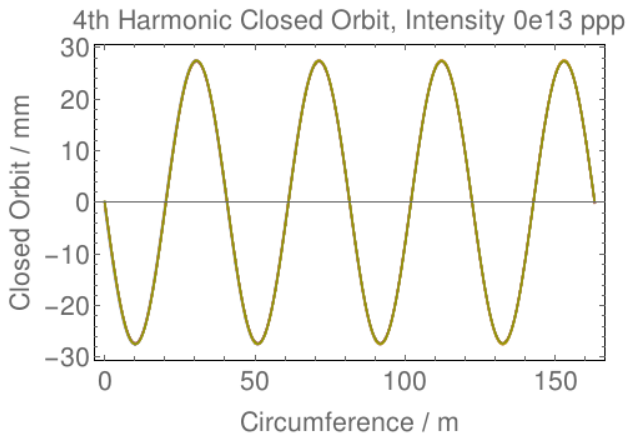

Figure 5.12: Vertical closed orbit plotted at intensity of 0×10^{13} ppp, overplotted in each case every 10 turns. Simulations were with a distributed angular kick to produce a 4$^{\text{th}}$ harmonic closed orbit.

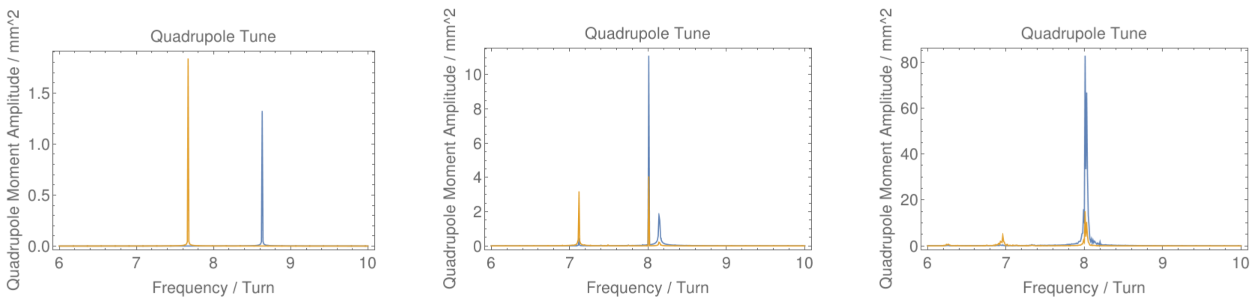

Figure 5.13: Quadrupole moment spectra with a 4$^{\text{th}}$ harmonic vertical closed orbit driving the horizontal κ_{21T} higher order image term at 8$^{\text{th}}$ harmonic, at intensities of 0, 9 and 12×10^{13} ppp. Blue: horizontal, yellow: vertical.

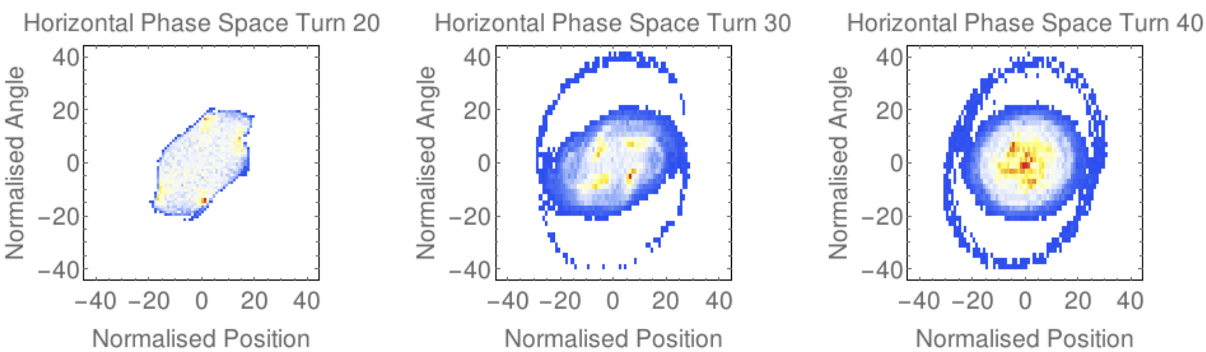

Figure 5.14: Horizontal phase space showing quadrupole resonance for beam driven with 4$^{\text{th}}$ harmonic vertical closed orbit at intensity of 1.2×10^{14} ppp, on turns 20, 30 and 40.

Smooth Focusing Simulations with Waterbag Beams

The same image terms that were investigated in the previous section were investigated here with the exception that the κ_{21} term driven by a single kick was not observed in simulations.

The main simulation parameters were the same as in Table 5.2. A decision was made not to use a waterbag beam which was RMS equivalent to the KV beam used in the previous sections, but rather one that was the same size (100% emittance). Whilst this made comparing the resulting simulations more difficult in some ways, it would have meant having different sized beams, which would have reduced the aperture available for closed orbits and resulting beam evolution. As image forces are a complex result of intensity, beam distribution, orbit and aspect ratio it was felt that this was acceptable. The main purpose of this section was to see how a more realistic beam distribution reacted compared with the less stable KV distribution.

WB Beam: Investigation of κ_{12} Image Term, Driven with 13$^{\text{th}}$ Harmonic Closed Orbit

The single particle Hamiltonian is the same as that in Section 5.8.1, though the non-linear space charge forces from the distribution will change the $V_0(J)$ term. A resonance of the form $3Q_H = 13$ was expected. The closed orbit was also very similar, so has not been replotted.

Tables 5.2 and 5.7 contain the values for the simulations run in this section, though the beam distribution was changed to a waterbag.

Figure 5.15 shows the FFT of the sextupole moment of the beam at three intensities, 0, 4 and 6.3×10^{13} ppp. At zero intensity there is no driving term. At higher intensities the driving term appears and at the highest intensity the beam is on resonance, indicated by the large magnitude of the frequency components.

Figure 5.16 shows horizontal phase space on turns 10, 20 and 30 for the simulations with intensity 6.3×10^{13} ppp. The third order structure of the resonance is clearly observed. The waterbag distribution beam responds less strongly than the KV due to the tune spread induced by the beam distribution.

Intensity at resonance	6.3×10^{13} ppp
Beam distribution	WB
Lattice tunes (Q_H, Q_V)	(4.65, 3.83)
Kick type	Horizontal 13$^{\text{th}}$ harmonic
Kick strength	0.7 mrad (peak)
Closed orbit match at resonance (x, x', y, y')	(0, -8.62, 0, 0)
Envelope match at resonance (β_H, α_H, β_V, α_V)	(6.13, 0, 7.7, 0)
Max closed orbit	17.3 mm

Table 5.7: Simulation parameter list, smooth focusing, WB beam, κ_{12} driven with 13$^{\text{th}}$ harmonic closed orbit.

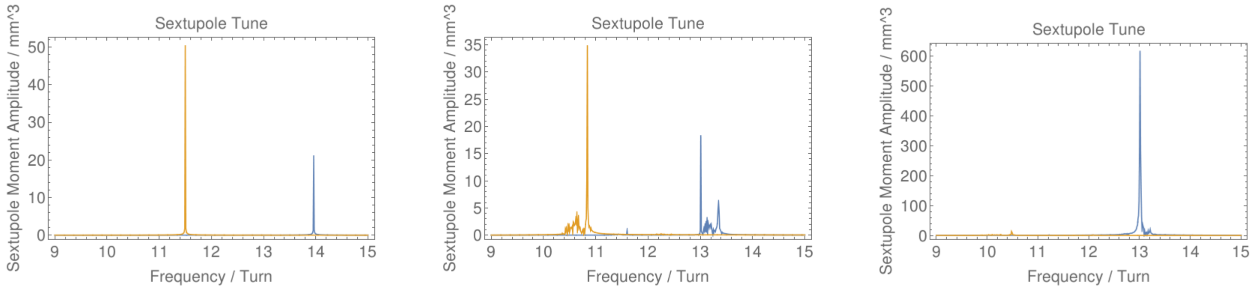

Figure 5.15: Sextupole moment spectra with a 13$^{\text{th}}$ harmonic closed orbit driving the κ_{12} higher order image term, at intensities of 0, 4 and 6.3×10^{13} ppp. Blue: horizontal, yellow: vertical.

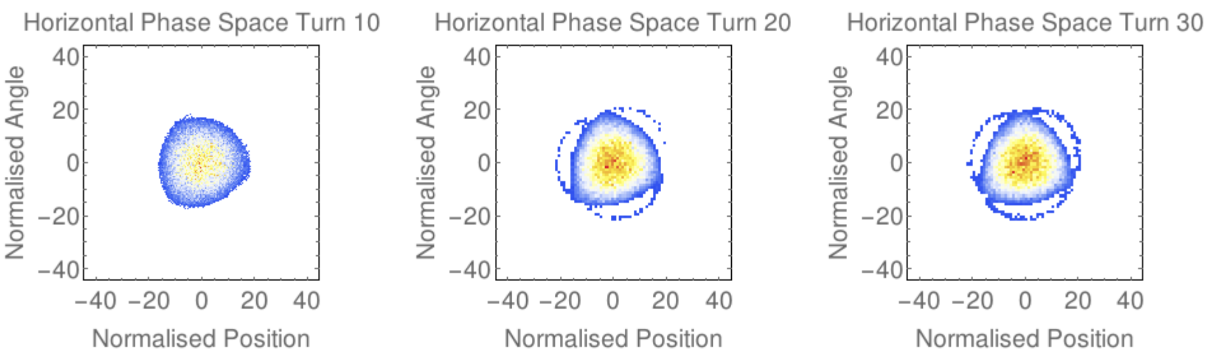

Figure 5.16: Horizontal phase space showing sextupole resonance for a waterbag beam driven with 13$^{\text{th}}$ harmonic closed orbit at intensity of 6.3×10^{13} ppp, on turns 10, 20 and 30.

This simulation with a more realistic beam distribution showed that images could still cause beam redistribution, though the effect was reduced compared with a KV beam. The parameters used were not comparable to those used on ISIS, but rather used to illustrate features of the beam dynamics.

WB Beam: Investigation of Effects of 4^{th} Harmonic Closed Orbit at ISIS Nominal Tunes

The results in this section are very similar to those in Section 5.8.3. As before, it was expected that the $2Q_H = 8$ resonance would be dominant. The different simulation parameters are listed in Table 5.8.

The same beam behaviour that was observed with the KV beam was witnessed with the waterbag distribution. Figures 5.17 and 5.18 show the quadrupole and sextupole moment spectra respectively. At zero intensity no driving terms were present. At an intensity of 5×10^{13} ppp a driving term at $2Q_H = 8$ appeared in the quadrupole spectra. However it was at an intensity of 6×10^{13} ppp that the beam reached resonance, and this was again the dipole phase space structure which coincided with a sextupole resonance as before.

Figure 5.19 shows horizontal phase space on turns 10, 20 and 30, clearly showing an integer resonance developing. The incoherent tune footprint for the simulation is shown in Figure 5.20. As there was more tune spread in the beam due to space charge, the footprint was different from that of the KV beam. However the particle tunes lie on top of the $Q_H = 4$ resonance line.

As with a KV beam, the behaviour observed with these simulations was hard to pin down. The beam redistributed with an integer (dipole) phase space structure, and this coincided with a sextupole coherent resonance. The dipole frequency of the beam was well above resonance. It was not obvious what was driving the sextupole in this instance. Various other factors may have contributed. This simulation was with a more realistic beam, at the ISIS nominal tune, and suggests that this effect should be investigated further as it may have consequences for ISIS operations.

Intensity at resonance	6.0×10^{13} ppp
Beam distribution	WB
Lattice tunes (Q_H, Q_V)	(4.31, 3.83)
Kick type	Horizontal 4^{th} harmonic
Kick strength	0.01 mrad (peak)
Closed orbit match at resonance (x, x', y, y')	(0, 2.57, 0, 0)
Envelope match at resonance (β_H, α_H, β_V, α_V)	(6.6, 0, 7.6, 0)
Max closed orbit	16.8 mm

Table 5.8: Simulation parameter list, smooth focusing, WB beam driven with 4^{th} harmonic closed orbit.

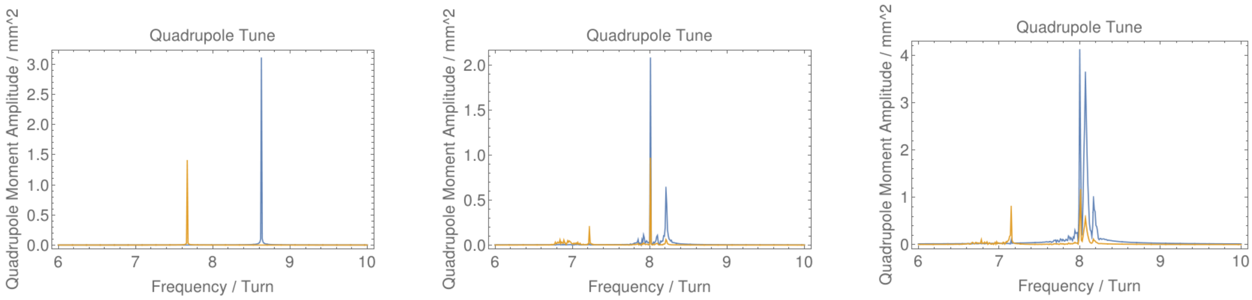

Figure 5.17: Quadrupole moment spectra with a 4th harmonic closed orbit driving the κ_{21} higher order image term at 8th harmonic, at intensities of 0, 5 and 6×10^{13} ppp. Blue: horizontal, yellow: vertical.

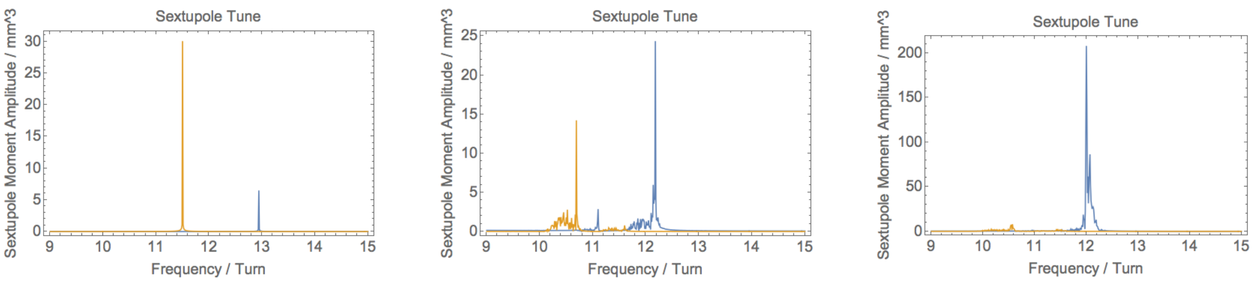

Figure 5.18: Sextupole moment spectra with a 4th harmonic closed orbit driving the κ_{30} higher order image term at 12th harmonic, at intensities of 0, 5 and 6×10^{13} ppp. Blue: horizontal, yellow: vertical.

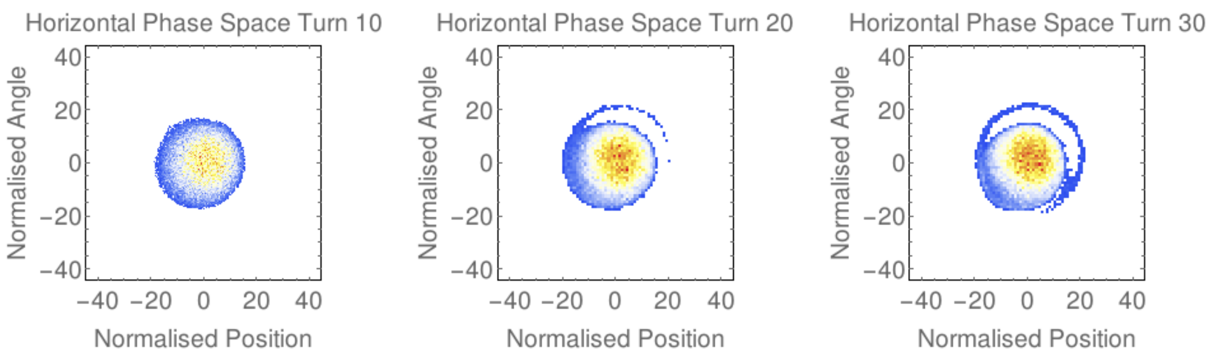

Figure 5.19: Horizontal phase space showing integer resonance for a waterbag beam driven with 4th harmonic closed orbit at intensity of 6×10^{13} ppp, on turns 10, 20 and 30.

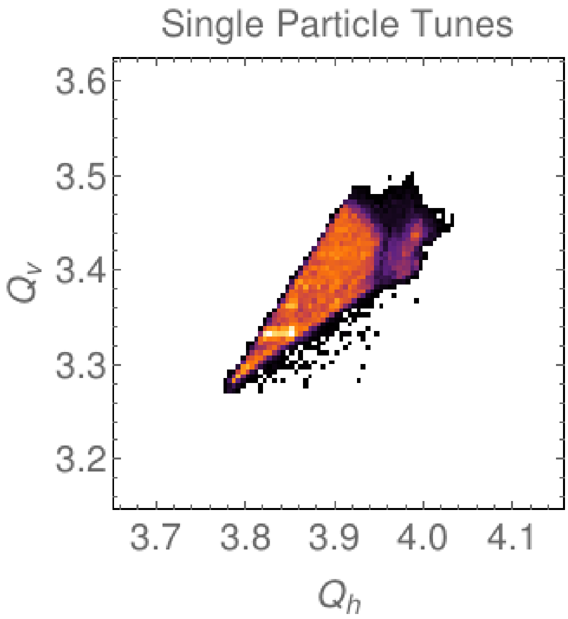

Figure 5.20: Single particle tune footprint for ISIS nominal tunes and 4$^{\text{th}}$ harmonic closed orbit, at an intensity of 6×10^{13} ppp, with a waterbag beam.

WB Beam: Investigation of Effects of 4$^{\text{th}}$ Harmonic Vertical Closed Orbit at ISIS Nominal Tunes

This section is very similar to Section 5.8.4, with a horizontal image term being driven with a vertical 4$^{\text{th}}$ harmonic closed orbit. As before it was expected that a $2Q_H = 8$ quadrupole resonance would be the dominant effect. The simulation parameters are listed in Table 5.9.

Figure 5.21 shows the horizontal quadrupole moment spectra at intensities of 0, 5 and 8×10^{13} ppp. The image driving term was not present at zero intensity, but appeared at $2Q_H = 8$ for higher intensities. The beam reached resonance at 8×10^{13} ppp, indicated by the sharp growth in the magnitude of the frequency component.

Figure 5.22 shows horizontal phase space on turns 20, 30 and 40 for an intensity of 8×10^{13} ppp. The two lobes of a quadrupole resonance are clearly visible.

A vertical 4$^{\text{th}}$ harmonic closed orbit was shown to drive a horizontal quadrupole resonance

Intensity at resonance	8.0×10^{13} ppp
Beam distribution	WB
Lattice tunes (Q_H, Q_V)	(4.31, 3.83)
Kick type	Vertical 4$^{\text{th}}$ harmonic
Kick strength	0.01 mrad (peak)
Closed orbit match at resonance (x, x', y, y')	(0, 0, 0, -2.96)
Envelope match at resonance (β_H, α_H, β_V, α_V)	(9.4, 0, 8.3, 0)
Max closed orbit	19.3 mm

Table 5.9: Simulation parameter list, smooth focusing, WB beam driven with 4$^{\text{th}}$ harmonic vertical closed orbit.

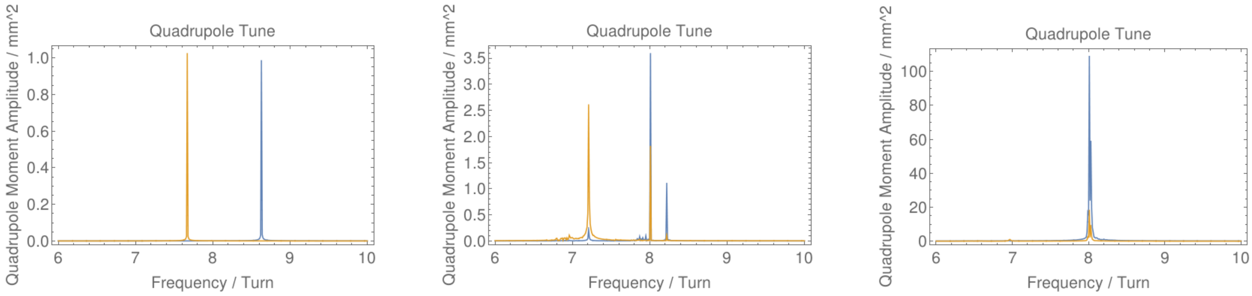

Figure 5.21: Quadrupole moment spectra with a 4^{th} harmonic vertical closed orbit driving the κ_{21T} higher order image term at 8^{th} harmonic, at intensities of 0, 5 and 8×10^{13} ppp. Blue: horizontal, yellow: vertical.

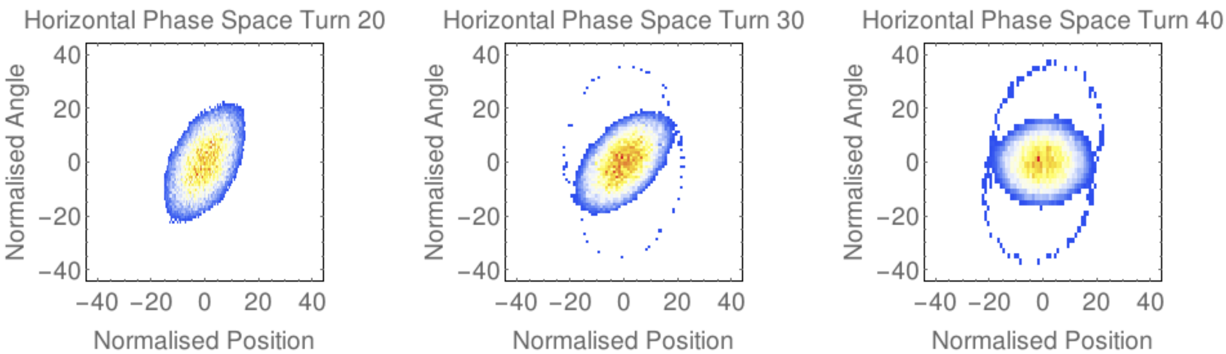

Figure 5.22: Horizontal phase space showing quadrupole resonance for a waterbag beam driven with 4^{th} harmonic vertical closed orbit at intensity of 8×10^{13} ppp, on turns 20, 30 and 40.

with a waterbag beam. The effect is weaker than with a KV beam as might be expected. This effect is expected to be present near to the ISIS nominal tunes, however with realistic beams and other effects it is possible that it is not of concern. It should however be investigated further.

Alternating Gradient Simulations

In this section the smooth focusing lattice was replaced with an alternating gradient lattice based on that of ISIS. The lattice was described in Chapters 2 and 3. The vacuum vessel was maintained at ± 100 mm for the first set of simulations, then the conformal vacuum vessel was included. These parameters are outlined in Table 5.10. Changing the tunes to explore specific image terms would have had additional consequences, changing the beam envelope and therefore image terms, as compared to the fixed vacuum vessel. Therefore only driving terms located near to the nominal tunes were investigated, specifically those driven by 4^{th} harmonic closed orbits in either the horizontal or vertical planes.

With an AG lattice and constant vacuum vessels only the horizontal closed orbit was found to produce a resonance, reported below. The vertical effect, already weakened with a WB beam, was not evident with the AG lattice.

WB Beam, AG Lattice: Investigation of Effect of 4^{th} Harmonic Closed Orbit at ISIS Nominal Tunes

In this section a 4^{th} harmonic horizontal closed orbit was used to drive image terms. As before the expected resonance was the $2Q_H = 8$ quadrupole resonance. The matched closed orbit at intensities of 0, 5 and 7×10^{13} ppp is shown in Figure 5.23. The orbits are overplotted every ten turns. The orbit is much more complex due to the interaction of the harmonic kicks with the alternating gradient lattice. Table 5.11 contains values for the simulation parameters used in this section.

As in the previous sections, the 4^{th} harmonic closed orbit produced an intensity dependent, quadrupole driving term, the effect on the beam motion is visible in Figure 5.24. A weak quadrupole resonance was indicated at an intensity of 7×10^{13} ppp, given the change in scale of the resonance frequency component at that intensity. However again other image

Lattice type	Alternating gradient
No. elements	880
Circumference	163.36 m
No. macros	50000
100% emittance (ε_H, ε_V)	(300, 300)
Vacuum vessel	± 100 mm (Square)
Turns simulated	100

Table 5.10: Simulation parameter list, alternating gradient.

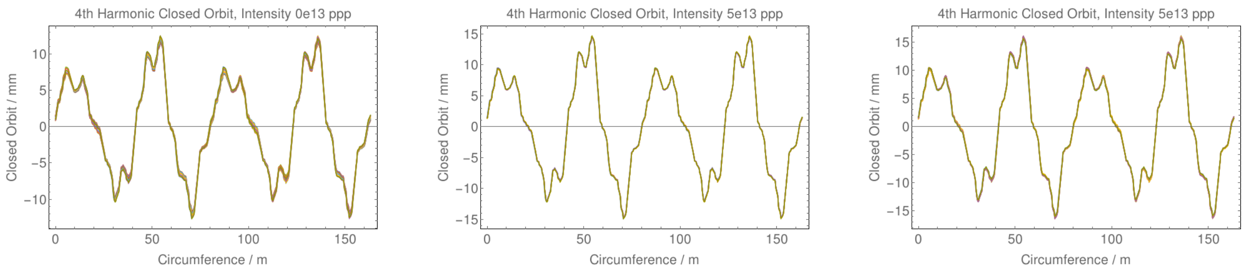

Figure 5.23: Closed orbit plotted at intensities of 0, 5 and 7×10^{13} ppp, overplotted in each case every 10 turns. Simulations were with a distributed angular kick to produce a 4^{th} harmonic closed orbit.

Intensity at resonance	7.0×10^{13} ppp
Beam distribution	WB
Lattice tunes (Q_H, Q_V)	(4.31, 3.83)
Kick type	Horizontal 4^{th} harmonic
Kick strength	0.005 mrad (peak)
Closed orbit match at resonance (x, x', y, y')	(1.54, 1.18, 0, 0)
Envelope match at resonance $(\beta_H, \alpha_H, \beta_V, \alpha_V)$	(8.7, 0.69, 7.96, -1.4)
Max closed orbit	16.1 mm

Table 5.11: Simulation parameter list, AG lattice, WB beam, κ_{21} driven with 4^{th} harmonic closed orbit.

terms were also present.

Figure 5.25 shows the sextupole moment spectra at the same intensities. In this case it is at an intensity of 5×10^{13} ppp that the sextupole moment frequency amplitude peaks. The driving term is situated at a frequency of 14 / turn. This is the frequency of the superperiodicity (10) modulated by the closed orbit harmonic (4).

Figure 5.26 shows horizontal phase space on turns 20, 30 and 40 at an intensity of 5×10^{13} ppp. The integer resonance seen in previous sections is visible. The incoherent particle tunes for the simulation are shown in Figure 5.27. The tunes overlap the $Q_H = 4$ integer resonance.

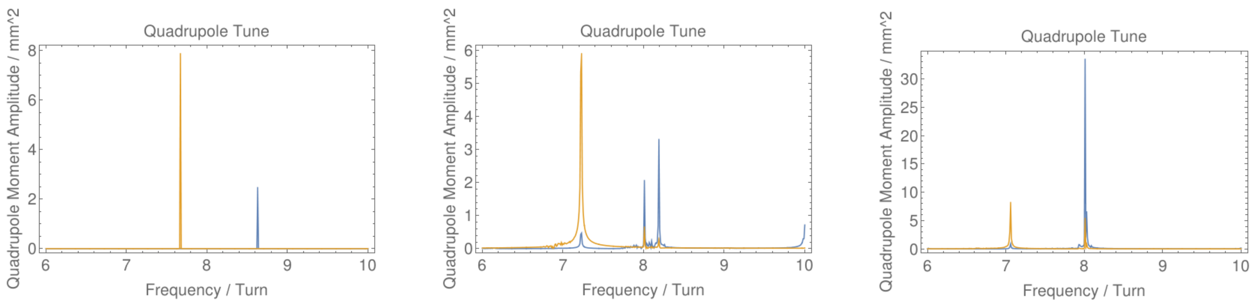

Figure 5.24: Quadrupole moment spectra with a 4^{th} harmonic closed orbit driving the κ_{21} higher order image term at 8^{th} harmonic, at intensities of 0, 5 and 7×10^{13} ppp. Blue: horizontal, yellow: vertical.

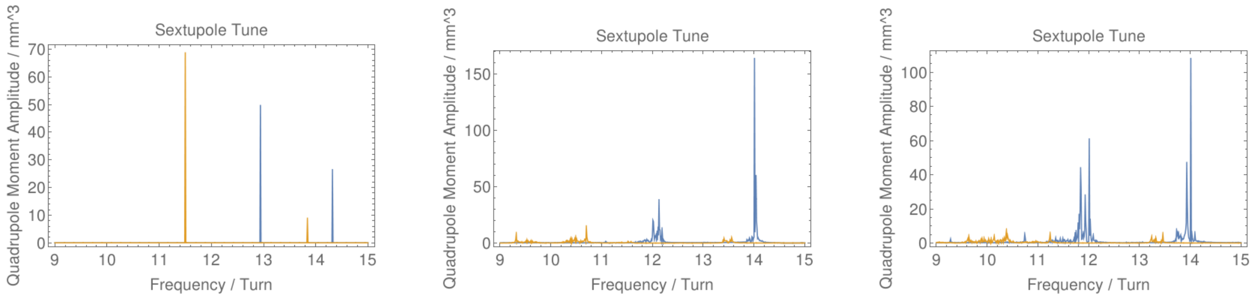

Figure 5.25: Sextupole moment spectra with a 4$^{\text{th}}$ harmonic closed orbit at intensities of 0, 5 and 7 $\times$ 10^{13} ppp. Blue: horizontal, yellow: vertical.

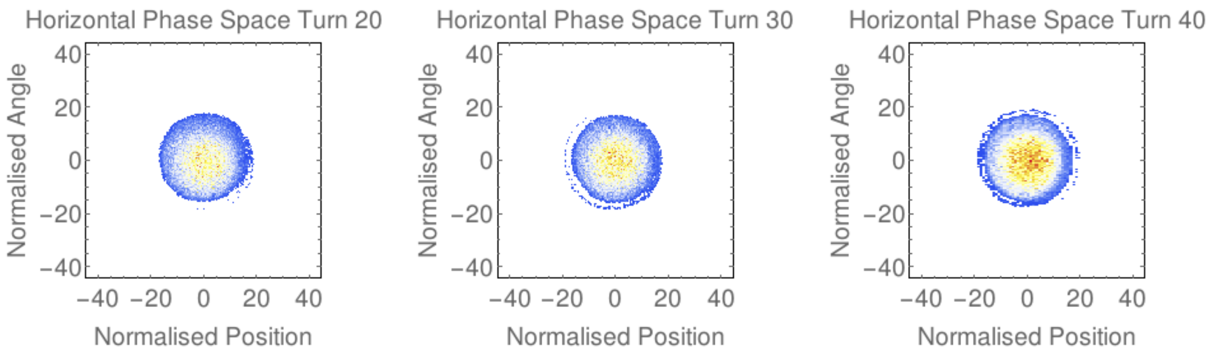

Figure 5.26: Horizontal phase space showing integer resonance for a waterbag beam driven with 4$^{\text{th}}$ harmonic closed orbit at intensity of 5 $\times$ 10^{13} ppp, on turns 20, 30 and 40.

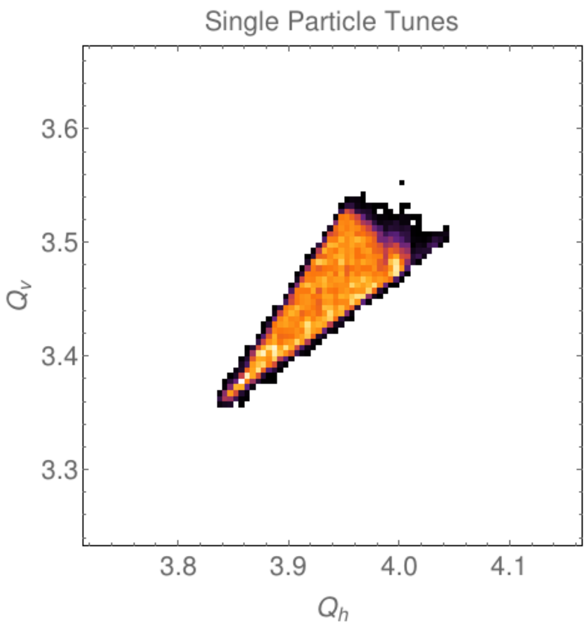

Figure 5.27: Single particle tune footprint for ISIS nominal tunes and 4$^{\text{th}}$ harmonic closed orbit, at an intensity of 5 $\times$ 10^{13} ppp, with a waterbag beam and AG lattice.

With an alternating gradient lattice, image driving terms near to the ISIS nominal tunes were found to have a much weaker effect. In the vertical plane no resonances were observed, while in the horizontal a weak integer resonance was observed in particle phase space. This integer resonance again coincided with a sextupole resonance in the frequency components of the third moment of the beam. The AG lattice in a smooth vacuum vessel is different from ISIS, actually creating more image driving terms. The result illustrated how an increase in the complexity of the simulation modified the beam dynamics.

WB Beam, AG Lattice, Conformal Vacuum Vessel: Investigation of Effect of 4$^{\text{th}}$ Harmonic Closed Orbit at ISIS Nominal Tunes

In the final section investigating image resonances, a conformal vacuum vessel was introduced. The alternating gradient lattice was the same as used in the previous section, reported in Table 5.10, except that the vacuum vessel was no longer constant, but instead varied with the lattice envelope. To allow for large closed orbits and subsequent beam evolution a larger conformal vessel size was used to that installed on ISIS. The aperture was twice the lattice envelope at all points. This is illustrated in Figure 5.28, where the horizontal and vertical 100% beam envelopes and apertures are shown. Image effects are stronger with the vacuum vessel at the ISIS aperture, but more difficult to observe as loss occurs before the beam can redistribute very much. Simulations with the actual ISIS aperture are included in Chapter 7.

A 4$^{\text{th}}$ harmonic horizontal closed orbit was used to generate image terms. The closed orbits were very similar to those shown in Figure 5.23 in the previous section. Values for the parameters used in the simulation are listed in Tables 5.10 and 5.12.

As in previous sections, the 4$^{\text{th}}$ harmonic closed orbit was being used to generate a $2Q_H = 2n = 8$ quadrupole driving term. This is illustrated in Figure 5.29. Quadrupole moment spectra are shown at intensities of 0, 5 and 9×10^{13} ppp are shown in the Figure, with

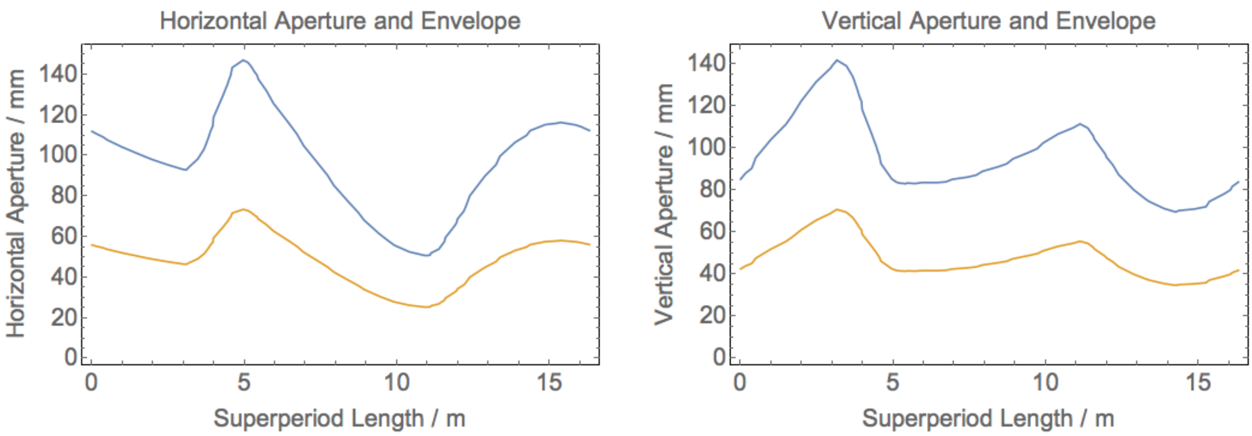

Figure 5.28: Envelope and aperture for a simulation with conformal vacuum vessels set to twice the design envelope.

Intensity at resonance	9.0×10^{13} ppp
Beam distribution	WB
Lattice tunes (Q_H, Q_V)	(4.31, 3.83)
Kick type	Horizontal 4^{th} harmonic
Kick strength	0.005 mrad (peak)
Closed orbit match at resonance (x, x', y, y')	(1.72, 1.19, 0, 0)
Envelope match at resonance $(\beta_H, \alpha_H, \beta_V, \alpha_V)$	(9.7, 0.8, 8.14, -1.4)
Max closed orbit	16.9 mm

Table 5.12: Simulation parameter list, AG lattice, WB beam, conformal vacuum vessel, κ_{21} driven with 4^{th} harmonic closed orbit.

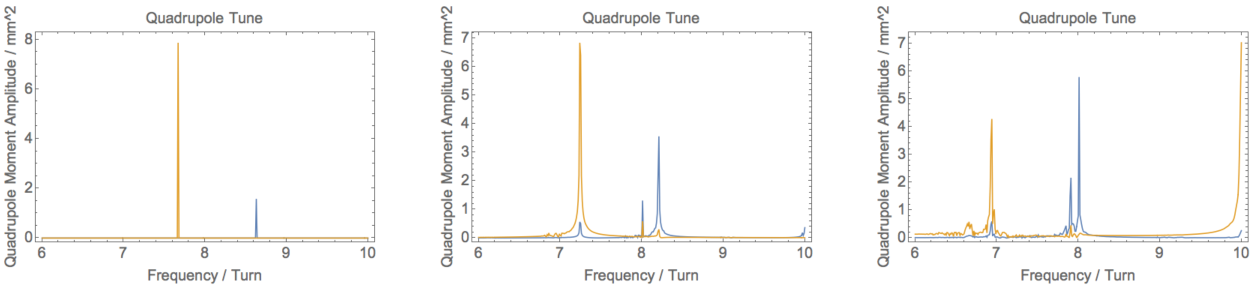

Figure 5.29: Quadrupole moment spectra with a 4^{th} harmonic closed orbit driving the κ_{21} higher order image term at 8^{th} harmonic, at intensities of 0, 5 and 9×10^{13} ppp. Blue: horizontal, yellow: vertical.

the effect of the intensity dependent driving term visible in the latter two cases. However, again as in previous examples, resonance was observed before the quadrupole moment of the beam encountered the driving term.

Figure 5.30 shows the sextupole moment spectra at the same intensities. There are two points of interest: at an intensity of 5×10^{13} ppp the beam encountered the relatively weak sextupole driving term encountered in the last section at $3Q_H = 14$ where the harmonic number was produced by the modulation of the superperiodicity and the harmonic closed orbit. However at an intensity of 9×10^{13} ppp the beam meets a much stronger vertical driving term at $3Q_V = 10$. Both the beam envelope and the conformal vacuum vessel provide strong image components at harmonic 10. The 1D results from Chapter 4 do not provide a sextupole driving term in the orthogonal plane and the single particle Hamiltonian model developed in this chapter does not apply to a resonance driven by modulation of the vacuum vessel, but only by the closed orbit. However if sextupole image fields exist they will be modulated at $h = 10$ along with the vacuum vessel.

Figure 5.31 shows vertical phase space on turns 70, 80 and 90 at an intensity of 9×10^{13} ppp. There is a strong third order resonance structure visible.

This section included most of the transverse physics that applies to ISIS, discounting effects due to magnetic images, longitudinal motion and momentum spread. The effect of images was materially different in this section, with a new, previously unobserved, resonance dominating the beam dynamics. The resonance was not explained by the 1D image terms or single particle Hamiltonian model developed in this thesis. It is possible that this resonance

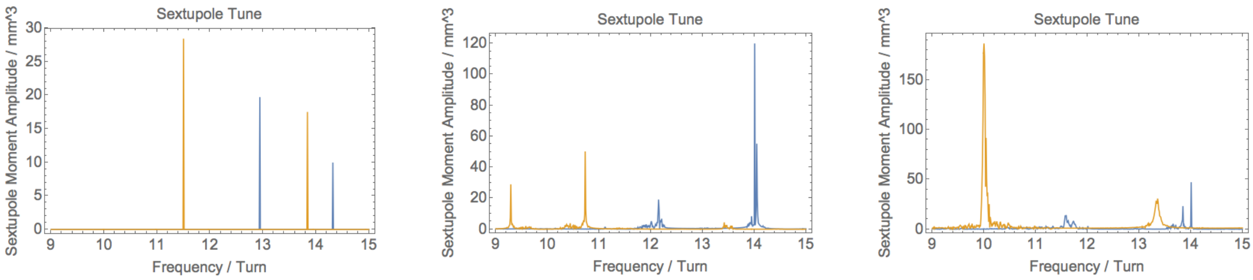

Figure 5.30: Sextupole moment spectra with a 4th harmonic closed orbit at intensities of 0, 5 and 9×10^{13} ppp. Blue: horizontal, yellow: vertical.

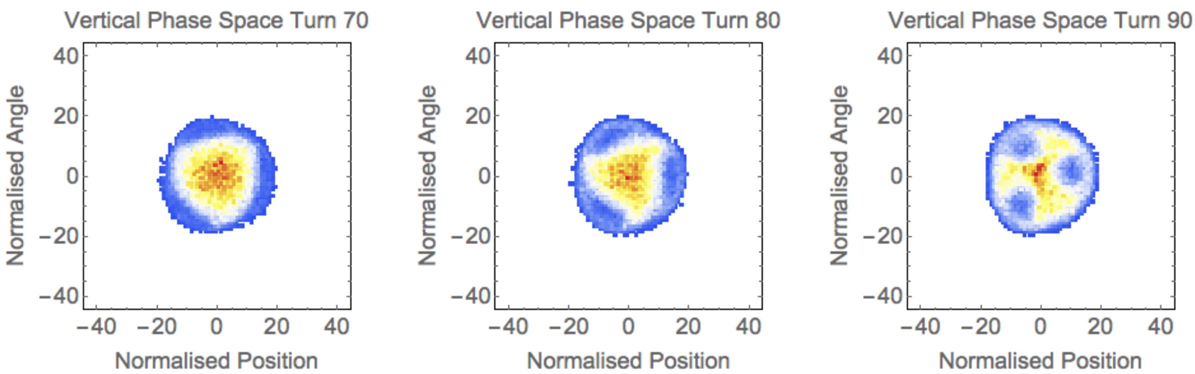

Figure 5.31: Vertical phase space showing sextupole resonance for a waterbag beam driven with 4th harmonic closed orbit at intensity of 9×10^{13} ppp, on turns 70, 80 and 90.

could contribute to beam growth on ISIS at high intensities and should be investigated further.

Summary

The existence of a closed orbit at low intensity and how it is modified at high intensity was established. Motion with respect to the closed orbit was explored using single particle resonance theory with high order image coefficients. Expected driving terms were derived, including their order and harmonic content. Coherent behaviour will modify the beam motion with intensity, in particular the coherent frequencies.

The theoretical model is 1D and does not account for the self-consistent behaviour of the beam. 2D PIC simulations including details of the beam and lattice were carried out to compare with results of the theory. A series of simulations was performed in which the simulation parameters were advanced from KV beams in a smooth focusing lattice to match the theory case, up to waterbag beams with an AG lattice and conformal vacuum vessel to represent the situation on ISIS more closely.

Simulations have explored both image terms of interest to establish their relation with theory, as well as terms of particular significance for ISIS. In general, simulations demonstrate significant effects on the beam due to images, as predicted by 1D image coefficients. Observed moment excitation and phase space redistribution indicated that these effects could contribute to loss at high intensities on ISIS.

In addition the simulations have identified other resonant behaviour which did not fit neatly into the 1D theoretical model and will require more work to understand. Some of this behaviour was exhibited by all of the different simulations explored. Other resonances were only seen under particular conditions. Image resonances will need to be studied further, in particular with simulations including other relevant effects, to determine their importance operationally.

In Chapter 7, simulations with closed orbits will be compared with other loss mechanisms as part of a design study, which will help to put them into context.

Important extensions to this work will include three dimensional simulations which also model beam dynamics features such as acceleration and injection. Experimental verification of image driven resonances is the long term goal.

Chapter 6

Experimental Studies Investigating Betatron Resonances on the ISIS Synchrotron

Introduction

In order to carry out more detailed and advanced experiments to study space charge and images at high intensity, it was first necessary to understand any intrinsic sources of beam loss present in the ISIS Synchrotron. For this reason a series of experiments was carried out to measure the relationship between betatron tune Q and beam loss, and identify resonances present at low intensity. This chapter details the results of the latest experiment, which provided the most refined results available.

The relationship between beam loss and working point on the ISIS Synchrotron was investigated. A map showing the location of the main resonance lines on the tune diagram was produced. This is the most detailed measurement of tune versus loss for the ISIS ring yet produced, and gives valuable new information.

The experiments were carried out with a low intensity, coasting beam in storage ring mode, so that high intensity effects, such as space charge, could be disregarded. The beam was stored at ISIS injection energy of 71.44 MeV. The existence of a resonance line indicated the presence of a related driving term, which at low intensity was most likely caused by magnet non-linearities, errors or misalignments.

The new results identify resonances which may contribute to beam loss during routine operation. They might affect the outcome of experiments investigating high intensity resonances and image field effects. The measured resonances can be added to our particle tracking models of the ring to improve accuracy and can perhaps be used to identify potential corrections using other magnet systems if required.

Resonances Near to the ISIS Working Point

Resonances which are closest to the working point are of greatest concern, though high intensity effects and non-linear magnet fields can cause the individual particle tunes to spread out, increasing the region over which resonances affect the beam. ISIS operates at a nominal working point $(Q_h, Q_v) = (4.31, 3.83)$ where Q_h and Q_v are the horizontal and vertical tunes, respectively. The general resonance condition is

$$mQ_h + nQ_v = h, \tag{6.1}$$

where m, n and h are all integers. $|m|+|n|$ is the order of the resonance and h is the azimuthal harmonic. The one dimensional resonances, up to 4^{th} order, which are near to the working point, and therefore may pose a risk, are shown in Table 6.1. The coupling resonances, up to 4^{th} order, are shown in Table 6.2. Resonances from Tables 6.1 and 6.2 in the range $(Q_h, Q_v) = (4.0, 3.5) - (4.4, 3.9)$ are shown in Figure 6.1. Some subset of these resonances may affect the beam and their identification is the purpose of the measurements reported here.

Order	Field Term	Horizontal	Vertical
1^{st}	Dipole	$Q_h = 4$	$Q_v = 4$
2^{nd}	Quadrupole	$2Q_h = 8, 9$	$2Q_v = 7, 8$
3^{rd}	Sextupole	$3Q_h = 12, 13$	$3Q_v = 11, 12$
4^{th}	Octupole	$4Q_h = 16, 17$	$4Q_v = 15, 16$

Table 6.1: One dimensional resonances near to ISIS nominal working point.

Order	Sum	Difference
2^{nd}	$Q_h + Q_v = 8$	$Q_h - Q_v = 0, 1$
3^{rd}	$Q_h + 2Q_v = 11, 12$	$Q_h - 2Q_v = -3, -4$
3^{rd}	$2Q_h + Q_v = 12, 13$	$2Q_h - Q_v = 4, 5$
4^{th}	$Q_h + 3Q_v = 15, 16$	$Q_h - 3Q_v = -6, -7, -8$
4^{th}	$2Q_h + 2Q_v = 16, 17$	$2Q_h - 2Q_v = 0, 1$
4^{th}	$3Q_h + Q_v = 16, 17$	$3Q_h - Q_v = 8, 9, 10$

Table 6.2: Coupling resonances near to ISIS nominal working point.

At low intensity these resonances may be driven by magnetic field non-linearities, errors or misalignments. At high intensity space charge and images will modify the effect of the original terms and may also introduce new terms. The linear errors (dipole and quadrupole) should dominate at low intensity and were observed to do so in previous reports exploring a larger region of the tune diagram [55, 56].

When the betatron tunes are set to values that coincide with a resonance line, the beam may be affected causing emittance growth and beam loss. The loss may be affected by the direction in which the resonance is crossed. Even though the measurements are done at low intensity, the intensity is not zero and there will be some broadening of the resonance lines.

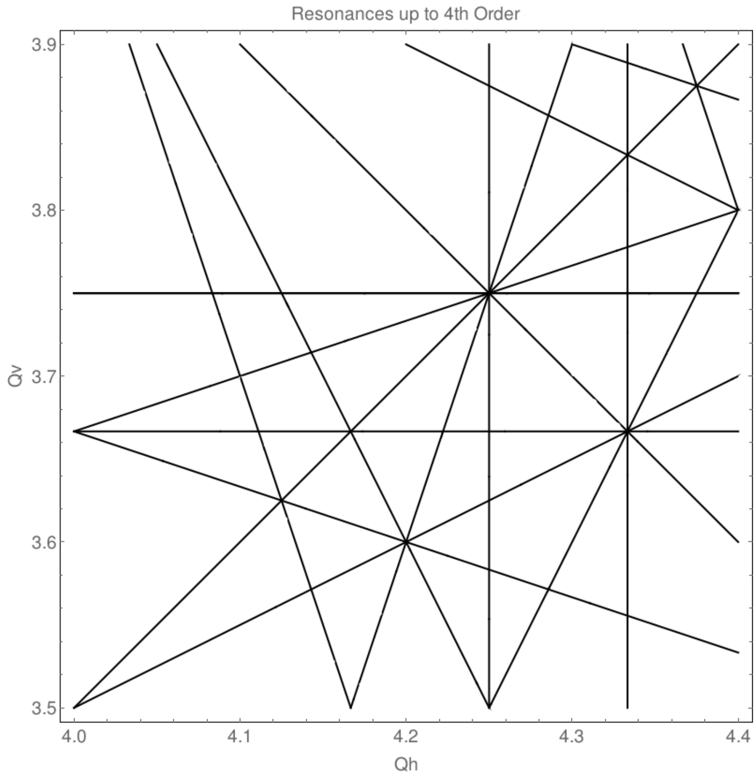

Figure 6.1: Resonances up to 4^{th} order in the region $(Q_h, Q_v) = (4.0, 3.5) - (4.4, 3.9)$

Overview of Experimental Method

ISIS Tune Control, Beam Configuration and Diagnostics

On ISIS, the nominal tune is set by the main lattice magnets: the quadrupoles and combined function dipoles. These are all excited together with sinusoidal 50 Hz. The tune is modified using separate, programmable trim quadrupoles, as detailed in Chapter 2. There are two in each straight section, making two families of ten magnets in all. One family is located near to the maximum horizontal beta function, the other to maximum vertical beta, giving effectively independent control of the horizontal and vertical tunes.

For these experiments the beam diluter was used. The beam diluter is a pepperpot intensity degrader in the LEBT, which can be set to allow either 10 or 40% beam transmission. For these experiments 10% transmission was used to circulate a low intensity beam in the synchrotron. At the end of injection this left a beam of 1×10^{12} particles per pulse (ppp) at injection energy 71.44 MeV. Tune control on ISIS has been established for high intensity operation so the set tune values do not correspond exactly with their measured values at low intensity. Due to the resonances obtained it was possible to reasonably estimate the position of the set tunes.

Beam loss was measured using the ring beam loss monitors (BLMs), while the corresponding reduction in circulating current was measured using an intensity monitor (R5IM).

Complications Due to Injection and Fast Acceleration Ramping

The experiment was made more challenging due to certain aspects of routine ISIS operation. ISIS is a rapid cycling synchrotron (RCS), which pulses at 50 Hz, with beam in the synchrotron for 10.4 ms. Protons are injected over $\sim 200\,\mu s$, with the beam painted in both transverse planes. There are pulse to pulse variations in injection efficiency which had to be accounted for if different experiments were to be compared.

Many machine parameters change rapidly during the cycle. RF systems accelerate the protons from 70 MeV to 800 MeV. Time varying functions are applied to the trim quadrupoles and steering magnets to optimise beam loss. These complications made measurements of beam loss due to tune changes difficult. Rapid cycling also imposed a time limit on measurements of a few milliseconds before the beam environment had changed unacceptably.

Storage Ring Mode

In order to minimise such complications and increase the time available to take the measurements, ISIS was operated in storage ring mode (SRM). ISIS can be run in this mode with the fundamental RF cavities switched off, the second harmonic cavities switched off and set off-tune, the AC component of the main magnet field switched off, the trim quadrupoles adjusted, the steering magnets set to injection values, the extraction kickers and extract septum turned off and the DC part of the main magnet field set to optimise injection from the linac.

The accelerator is run at a repetition rate of 0.4 Hz (50/128) and a coasting beam at injection energy is allowed to circulate in the synchrotron until it is lost against the collectors. Beam can be observed with the R5IM current monitor, BLMs and profile monitors, and may survive for up to a second. Measurements are most easily made over the normal 20 ms machine cycle for which the diagnostics are optimised.

Details of Measurements and Results in Storage Ring Mode

Performing the measurements in SRM removed the time constraints and complications due to RCS mode. The 10% beam diluter was inserted, with injected beam intensities of the order of 1×10^{12} ppp. Particles were injected normally at the start of a measurement.

The tune vs. loss diagram was reproduced four times. For each diagram the tune was scanned one way whilst being held constant in the other plane. This was repeated until the area covered by the diagram was filled. Four diagrams were made including Q_h being scanned down while Q_v was held constant, Q_h scanned up while Q_v was held constant, Q_v scanned down while Q_h was held constant and Q_v scanned up while Q_h was held constant.

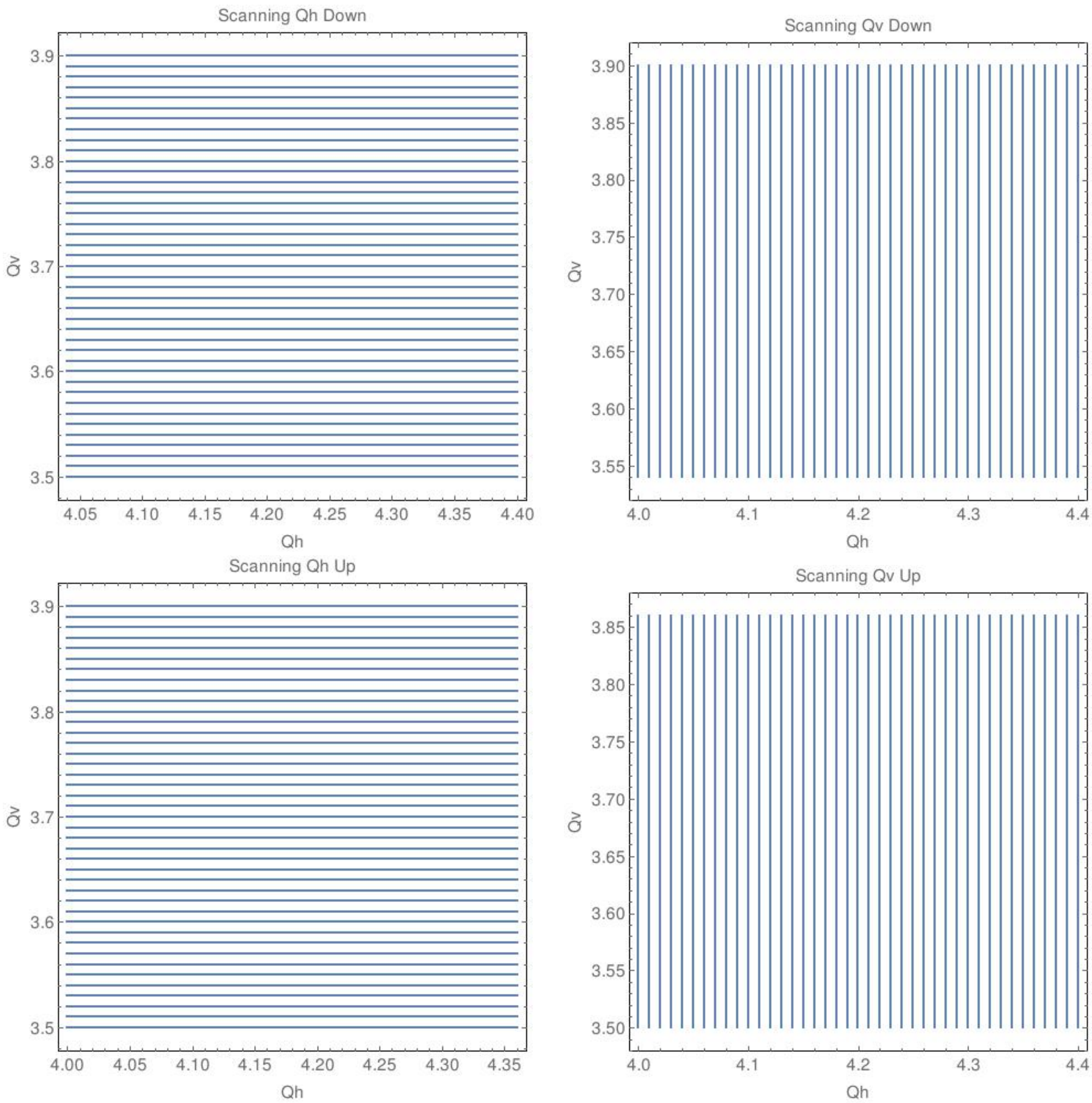

Figure 6.2: Diagrams indicating tune scan patterns and directions during measurements.

This method was used to investigate whether resonances were sensitive to the direction of the tune scan. The direction could be important as if beam is lost while passing through a resonance, that will reduce the intensity which will decrease the tune spread. If the tune is being scanned down, it is possible that more particles will be put onto the resonance. Alternatively if the beam is being scanned up through a resonance, beam loss will cause the particles to pass through the resonance more quickly.

The resulting diagrams are shown schematically in Figure 6.2. The tunes were ramped linearly in both planes over 2 ms to the start point of a measurement so as not to exceed the slew rate of the trim quadrupoles. Then the tune was ramped in one plane over 8 ms to its final value. In the other plane the tune was held fixed at a sequence of constant values. These different settings are illustrated in Figure 6.3 for the example where Q_h is being scanned down.

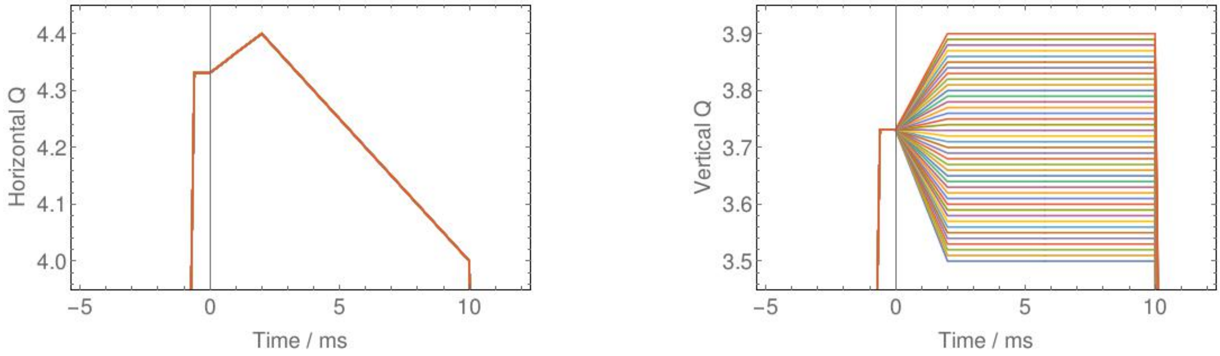

Figure 6.3: Betatron tune values used while scanning Q_h down, (left) Q_h values, (right) Q_v.

During each measurement beam intensity from R5IM and the combined beam loss from all of the ring beam loss monitors (the BLMSum signal) were captured on a scope using LabVIEW. A typical intensity monitor signal is shown on the left in Figure 6.4. During this measurement Q_h was scanned from 4.4 to 4.0 from 2 to 9 ms, while Q_v was held constant at 3.5. The signal is clearly quite noisy. Mathematica [42] was used to smooth and differentiate the signals. Mathematica includes a DerivativeFilter function which was used for this purpose. Output from this function was benchmarked against some test data using interpolation and standard differentiation of the signals. The filtered data is shown on the right in Figure 6.4. The BLM signals required less processing: they were simply smoothed and combined into a density plot. The time coordinate of each measurement was converted to a tune value.

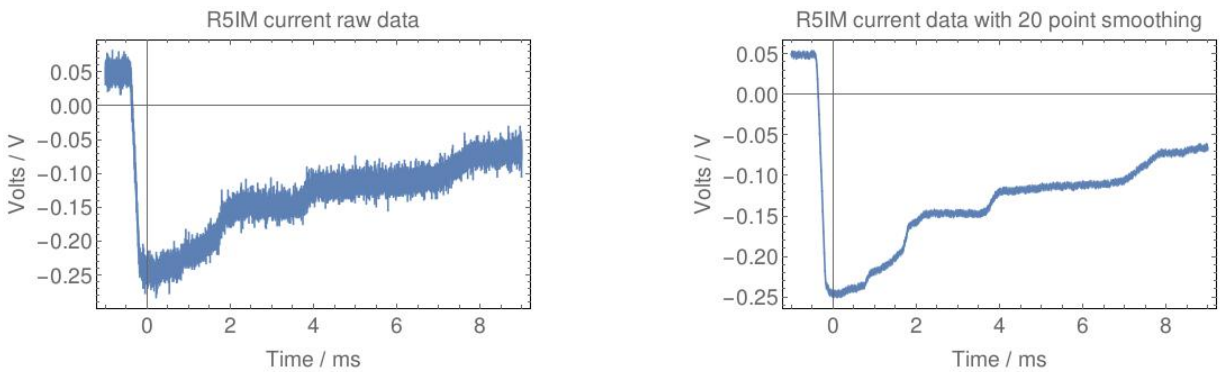

Figure 6.4: (Left) Example storage ring mode intensity monitor waveform, (right) smoothed intensity monitor signal.

A data acquisition error meant that the last millisecond of each scan was not recorded during the experiment and so the different scans all have a different edge missing, dependent on the scan direction and plane.

Results

The results of scanning the tune and recording changes to the beam intensity are shown in Figure 6.5 and beam loss in Figure 6.6. Colours tending to blue indicate a lower rate of beam loss, while those nearer red indicate a higher rate. The direction of the tune scan in each of these sets of plots corresponds to those defined in Figure 6.2.

Resonance lines are visible. These resonance lines are indications that there are magnet non-linearities, errors or misalignments which are interacting with the beam to cause emittance growth and loss. They have some width due to various effects including the strength of the driving term, space charge effects (even at low intensity) and chromatic tune spread. Some lines show up on all or several of the plots, while others are dependent on the plane and direction of the tune scan. For instance the horizontal resonance $3Q_h = 13$ shows up much more strongly when the tune is scanned horizontally, whilst the vertical resonances $3Q_v = 11$ and $4Q_v = 15$ show up more when the tune is scanned vertically. The sum resonance $Q_h + Q_v = 8$ shows up most strongly when the tune is scanned down vertically, while the difference resonance $Q_h - 2Q_v = -3$ is clear in all of the other diagrams.

The beam intensity results and beam loss results are very similar, showing the same beam loss structures. Resonance lines have been overlaid on the beam loss monitor data, Figure 6.7. The resonance lines have been offset by -0.05 in the vertical tune to account for discrepancies with the set tune.

The most prominent resonance lines present in the measurements are shown in Figure 6.8, and also summarised in Table 6.3. All of these lines indicate potential driving terms in the ISIS lattice, whether from higher order magnetic fields (there is a deliberate octupole field present in some of the main quadrupoles), magnet errors or misalignments.

Order	Resonance
Sextupole	$3Q_h = 13$
Sextupole	$3Q_v = 11$
Octupole	$4Q_v = 15$
2^{nd} order	$Q_h + Q_v = 8$
3^{rd} order	$Q_h - 2Q_v = -3$
3^{rd} order	$2Q_h - Q_v = 5$

Table 6.3: Resonances found during investigations.

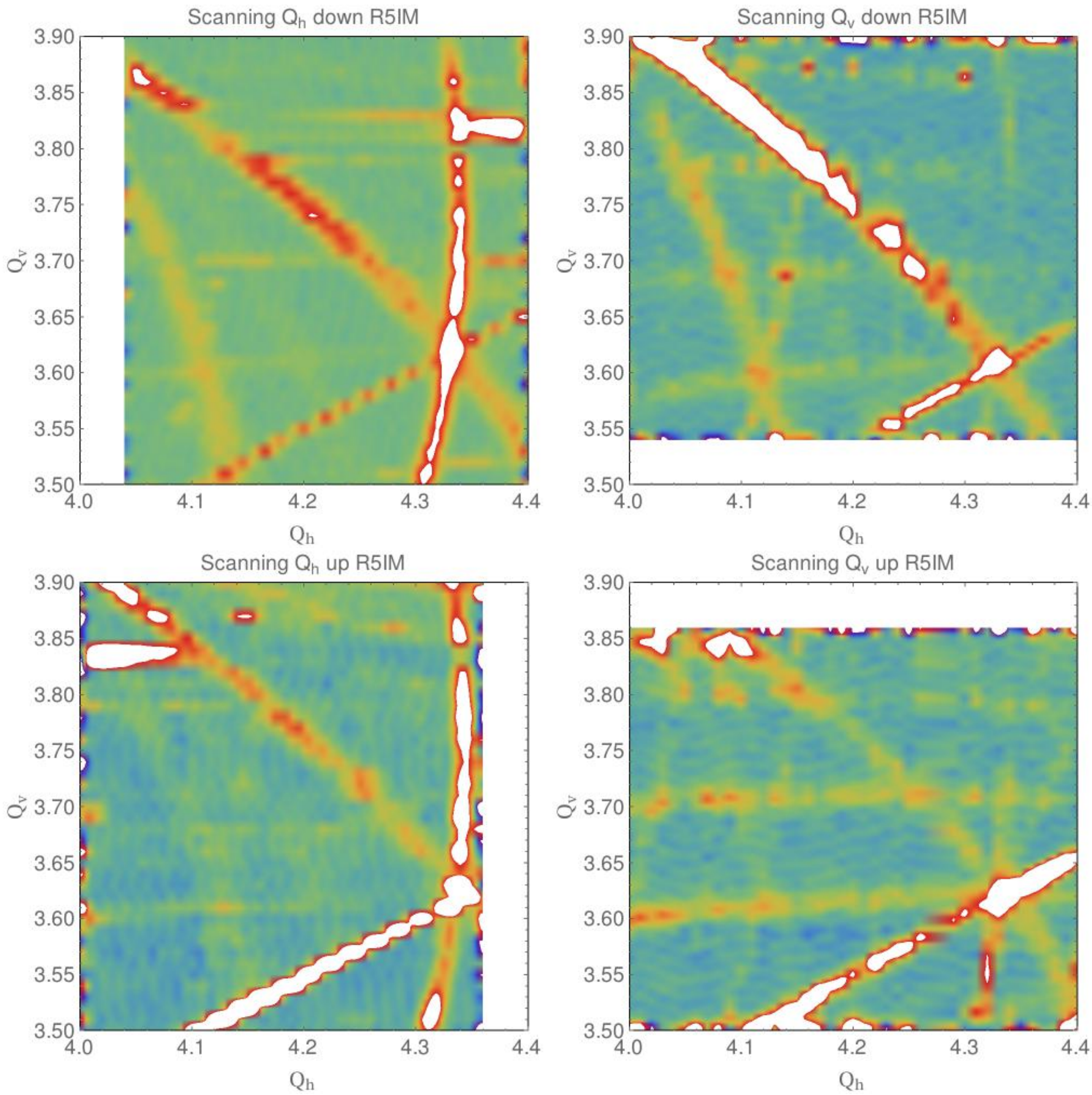

Figure 6.5: Beam loss vs. tune intensity monitor data, where red indicates increased rate of beam loss with tune change along the measurement direction. The pattern and direction of the measurements mirrors that shown in Figure 6.2.

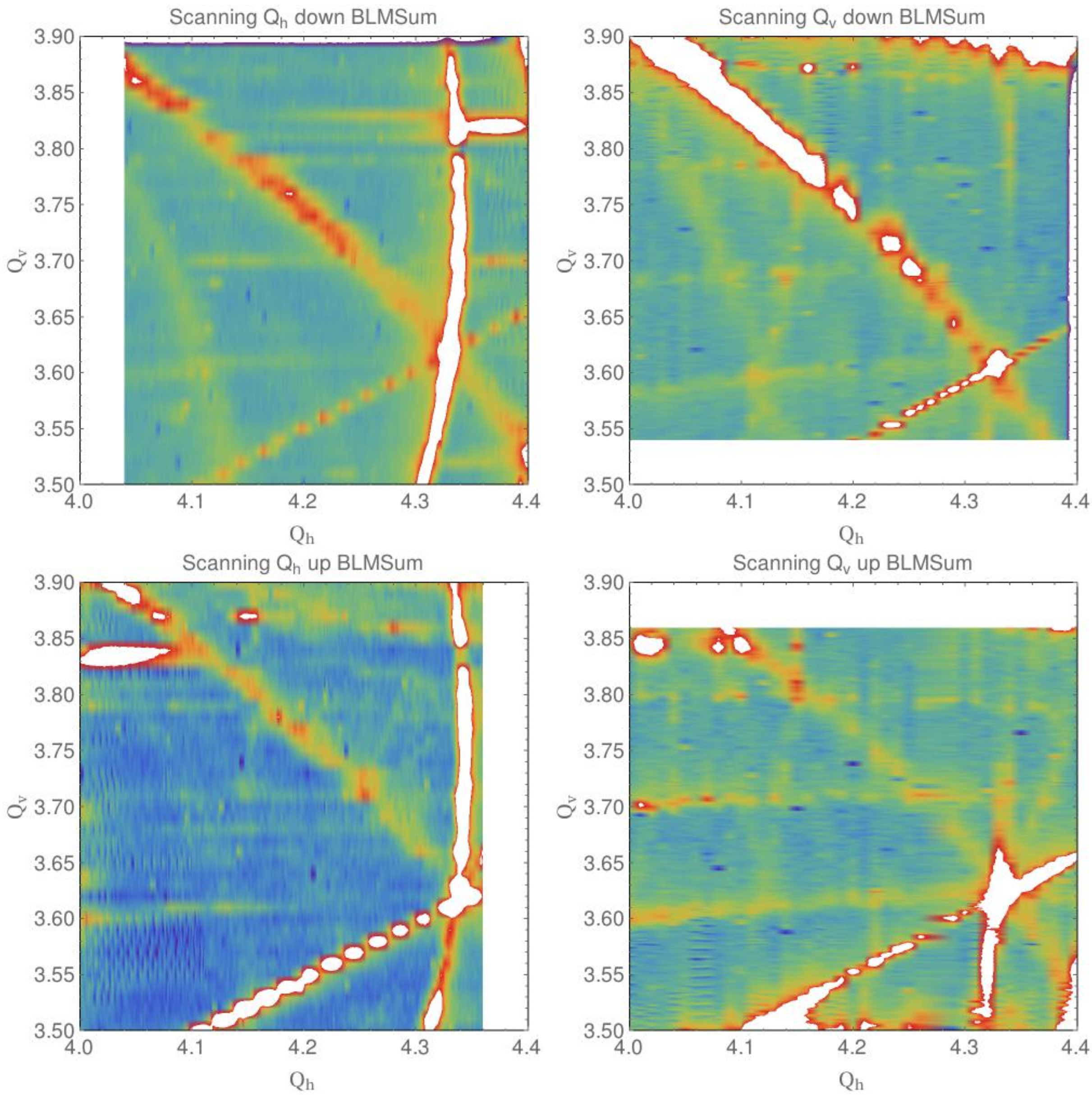

Figure 6.6: Beam loss vs. tune beam loss monitor data, where red indicates increased rate of beam loss with tune change along the measurement direction. The pattern and direction of the measurements mirrors that shown in Figure 6.2.

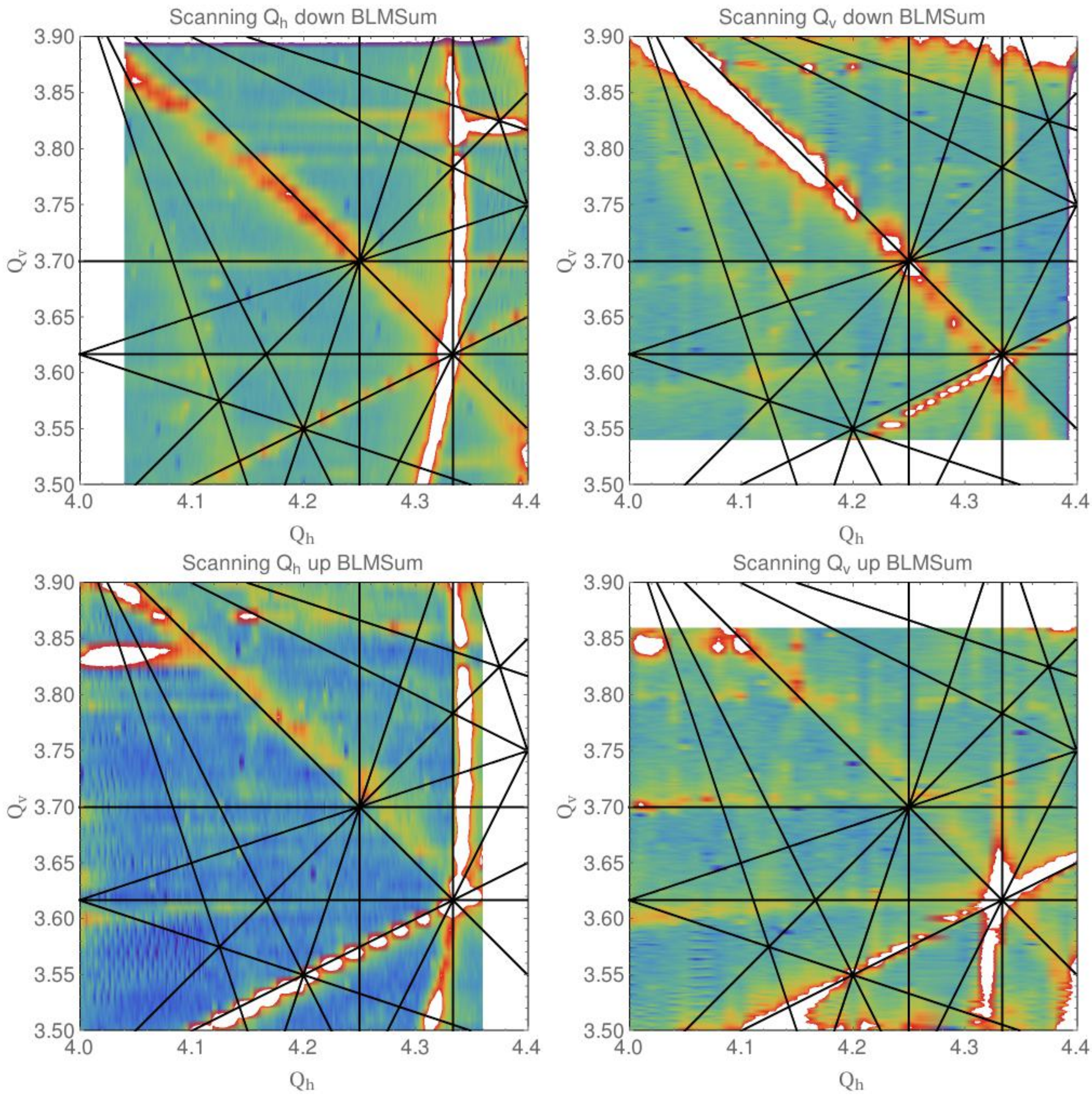

Figure 6.7: Beam loss vs. tune beam loss monitor data from Figure 6.6 with resonance lines overlaid but offset by -0.05 vertically. The pattern and direction of the measurements mirrors that shown in Figure 6.2.

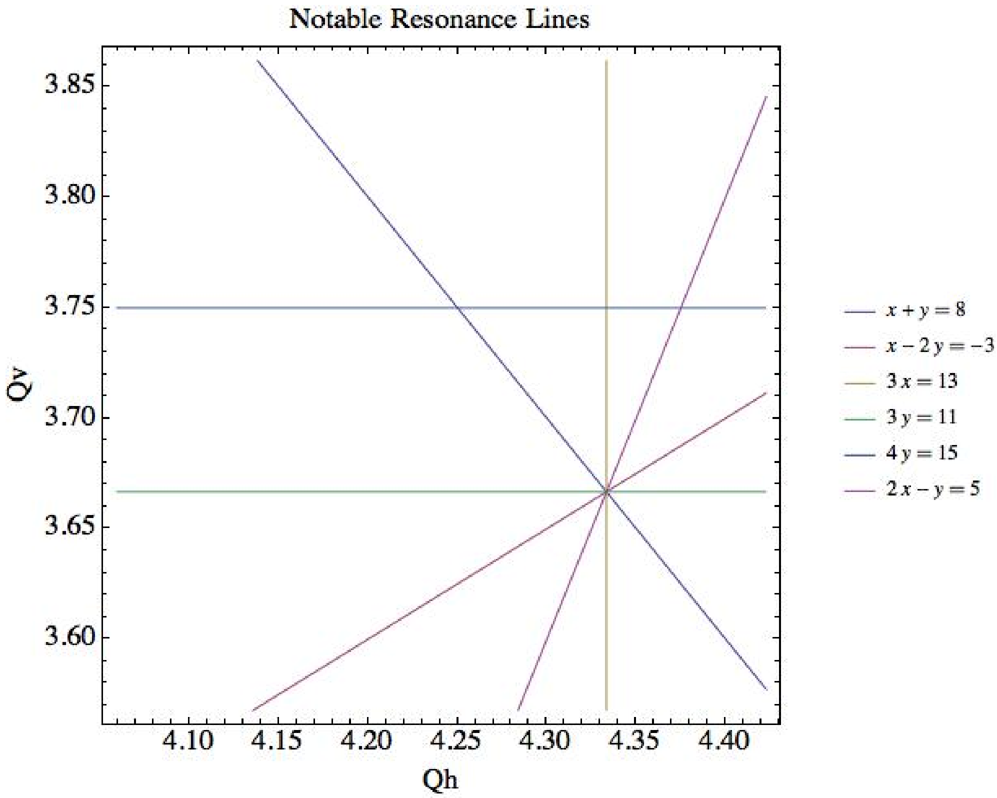

Figure 6.8: Prominent resonance lines in intensity monitor data.

Summary

New experiments have been performed on the ISIS synchrotron exploring the relationship between the betatron tune and beam loss when in storage ring mode.

These new studies have given the first detailed identification and verification of main driving terms present on the ISIS lattice, beyond the already known integer and half integer. This is essential information for advancing the understanding of high intensity behaviour of the machine. These measurements open up a method for investigating betatron resonances in more detail.

The measurements required a new configuration and experimental method for the machine (SRM and low intensity working point optimisation). Now that this method is established the low intensity driving terms can be explored in much more detail than was previously possible, and correction schemes investigated.

The effect of the resonances needs to be explored at both low and high intensities. Early results at high intensity indicate that resonance lines are modified as the intensity changes.

Further work will look at what effect these resonances might have on beam dynamics and beam loss by including them in particle tracking simulations. High order magnetic field components have been simulated and measured for the trim quadrupoles on ISIS [57], and more detailed models of the main dipoles and quadrupoles are in development. ISIS colleagues are working to compare the effects of driving terms these magnet models predict with the experimental data reported here.

Simulations including all new loss sources will ultimately be compared with the real machine in rapid cycling mode. The end result will be greater knowledge about the causes of beam loss at ISIS.

Chapter 7

An Assessment of Transverse Dynamics for the 180 MeV Injection Upgrade for ISIS

Introduction

This chapter takes the ideas discussed in the rest of the thesis and applies them to the problem of understanding transverse beam loss processes for the proposed 180 MeV Injection Upgrade, which was introduced in Chapter 2. Assessments are made for important aspects of transverse dynamics that could impose limitations on intensity. The work uses simplified models that include the essential features of transverse dynamics, and representative values of key parameters to test the feasibility of the upgrade ideas. The purpose of the work was to check effects and limits of basic loss mechanisms, before the more complete 3D models (which incorporated conclusions from this work) were used to study the 3D dynamics in detail.

Transverse dynamics are a major factor for any upgrade to the ISIS Synchrotron. For the proposed upgrade, replacing the existing 70 MeV injector with a new 180 MeV linac, the main benefit is the reduction in transverse space charge on injection into the synchrotron [25]. There are several other important factors. The linac is 50 years old, and can be updated with more reliable modern technology. The incorporation of a beam chopper into the new optimised 180 MeV injection system will reduce losses as the beam is trapped into bunches. An associated increase in the bunching factor will further reduce the effects of transverse space charge. Overall it is anticipated that these changes will enable an increase in the intensity in the synchrotron by almost a factor of 3, to 8×10^{13} protons per pulse (ppp), with a corresponding increase in beam power to 0.5 MW, while maintaining beam losses at manageable levels.

Transverse Dynamics for the Injection Upgrade

The transverse dynamics issues that result from higher energy injection into the ISIS rapid cycling synchrotron (RCS) were investigated. Issues were limited to those accessible with 2D transverse models and unbunched coasting beams.

The main motivation for increasing the injection energy is to reduce the effect of transverse space charge in the synchrotron. Simple analytical estimates of intensity limits imposed by space charge are presented in Section 7.3. Changes to the beam energy also have a significant effect on beam size or emittance at extraction and this is analysed in Section 7.4. Simple estimates, while being useful for comparisons, do not take in account the complex beam behaviour present in a real accelerator.

A better estimate is provided by a high intensity, self-consistent transverse beam model which included much of the relevant physics required to predict beam loss. The limitations in the simple treatment in Sections 7.3 and 7.4 are explained and use of simulation codes to give better assessments of expected losses is summarised in Section 7.5. Section 7.6 is an introduction to the simulation tool used to study transverse dynamics. In Section 7.7 extensive simulation tests are presented which give key indications of losses expected due to half integer errors. Section 7.8 takes the simulations from Section 7.7 and adds harmonic closed orbits to drive image terms. The combined effects are investigated.

A major source of loss on the upgraded machine could be the resistive wall head-tail instability [58]. In Section 7.9 the possibility of moving the working point to avoid the instability is analysed. Recent experimental results which explored moving the working point at low intensity and identified a number of non-linear driving terms are summarised in Section 7.10. Finally these results are summarised and further work is discussed.

Limits Calculated from Direct Space Charge Tune Shift

Following Hofmann again, [1], for a uniform, circular beam of radius a moving at velocity βc in the longitudinal direction with charge density λ, Equations 1.4 and 5.1 can be combined to give the equation of motion including linear space charge forces:

$$\frac{d^2y}{dt^2} + (Q\Omega)^2 y = \frac{e\lambda}{2\pi\epsilon_0 a^2 m_0 \gamma^3} y \tag{7.1}$$

where y is the transverse coordinate, t is time, Q is the betatron tune, Ω is the revolution frequency, e is the fundamental electric charge, ϵ_0 is the permittivity of free space, m_0 is the particle rest mass and β and γ are the usual relativistic factors. Including the space charge forces with the focusing forces gives

$$\frac{d^2y}{dt^2} + \left((Q\Omega)^2 - \frac{e\lambda}{2\pi\epsilon_0 a^2 m_0 \gamma^3}\right) y = 0. \tag{7.2}$$

For this example of a uniform beam with linear space charge forces Equation 7.2 can be re-written with a new tune incorporating the space charge forces

$$\frac{d^2y}{dt^2} + (Q_M\Omega)^2 y = 0 \tag{7.3}$$

where Q_M is the space charge modified tune and ΔQ is the modification due to space charge

$$Q_M = Q + \Delta Q. \tag{7.4}$$

If ΔQ is small with respect to Q, then the square can be expanded as

$$Q_M^2 \approx Q^2 + 2Q\Delta Q \tag{7.5}$$

Associating ΔQ with the space charge term in Equation 7.2 and using $\Omega = \beta c/\rho$ where ρ is the accelerator radius

$$\Delta Q = -\frac{e\lambda\rho^2}{4\pi\epsilon_0 m_0 c^2 a^2 Q\beta^2\gamma^3}. \tag{7.6}$$

Writing the charge density $\lambda = \frac{Ne}{2\pi\rho B_F}$, where N is the number of particles in the ring, B_F is the bunching factor and using the classical proton radius $r_0 = e^2/(4\pi\epsilon_0 m_0 c^2)$

$$\Delta Q = -\frac{r_0 N\rho}{2\pi a^2 Q\beta^2\gamma^3 B_F}. \tag{7.7}$$

Finally using $a = \sqrt{\beta_y\varepsilon}$, where β_y is the Twiss beta function and ε is the 100% emittance and the average value of the Twiss beta function, $\beta_y = \rho/Q$ leads to the incoherent tune shift formula:

$$\Delta Q = -\frac{r_0 N}{2\pi\beta^2\gamma^3\varepsilon B_F} \tag{7.8}$$

The incoherent tune shift is a useful figure of merit for directly comparing machines, though it does not take into account any coherent, self-consistent effects. While the ISIS beam is neither round nor uniform, ISIS and the upgrade can be expected to accelerate equivalent beams.

The intensity gain provided by upgrading injection comes mainly as a result of the reduction in space charge forces at injection, and the optimised chopped injection scheme. For the present unchopped injection scheme, protons are injected into an unbunched coasting beam, which is then bunched by the RF fields. Space charge peaks during the beam trapping process, when the beam is at an energy of $\sim 80\,\mathrm{MeV}$. At this point the bunch has formed, increasing the peak line density, but acceleration has not reduced transverse space charge effects very much. For the upgrade space charge peaks directly at the end of injection.

It is assumed that the RCS will be able to accelerate an intensity with equivalent space charge levels, i.e. with the same peak tune shift as for present operations. Emittances at injection will also remain unchanged. Therefore the possible intensity gains come from an increase in the energy, through $\beta^2\gamma^3$ and the increased bunching factor. However the beam will be at higher energy and therefore more activating, so that particle losses must be reduced to stay at the same activation levels. Therefore a conservative number for the intensity was chosen.

Table 7.1 contains these values calculated for the RCS at 80 MeV and 180 MeV with bunching factors provided from relevant longitudinal dynamics calculations [59]. These numbers suggest that the intensity can be increased by a factor of 3.71. ISIS routinely runs with an intensity of between 2.5 - 3 $\times 10^{13}$ ppp which is therefore increased to 9.3 - 11.1 $\times 10^{13}$ ppp. Allowing contingency for a number of possible loss mechanisms (and increased activation) the conservative figure of 8×10^{13} ppp has been chosen as a working intensity for the upgrade. In terms of beam power, this represents an increase from 192 kW to 512 kW.

Symbol	**Description**	**80 MeV**	**180 MeV**
β_0	Relativistic beta at peak ΔQ	0.3885	0.5440
γ_0	Relativistic gamma at peak ΔQ	1.085	1.192
ε_x, ε_y	100% emittance (π mm mrad)	300	
N_0	Number of injected particles	3×10^{13}	8×10^{13}
B_F	Bunching factor at peak ΔQ	0.35	0.5
R	Machine mean radius (m)	26.0	
C	Machine circumference (m)	163.36	
ρ	Dipole bend radius (m)	7.0028	
B_{AC}	Dipole AC field (T)	0.2606	0.2036
B_{DC}	Dipole DC field (T)	0.4364	0.4934
f_{rep}	Repetition frequency (Hz)	50.0	
Q_h, Q_v	Nominal betatron tune values	4.31, 3.83	

Table 7.1: Comparison of essential space charge parameters, for peak space charge levels with current injection scheme at $\sim$ 80 MeV and at the end of injection for the upgrade with 180 MeV energy.

Emittance Damping and Beam Size at Extraction

The transverse emittance of the beam decreases over acceleration via adiabatic damping. Damping of emittance ε is determined by the conservation of normalised emittance $\varepsilon^* = \beta\gamma\varepsilon$. Transverse beam size is proportional to the square root of the emittance. With 70 MeV injection and a 300 π mm mrad beam, the beam size damps by almost a factor of 2 over the course of acceleration. If 180 MeV injection is used instead with the same emittance the beam size is damped by a reduced factor of 1.5. As a result the beam is larger at extraction and an upgrade to the extraction line components will be required to accommodate the beam. The respective emittances are shown in Figure 7.1.

Determining Space Charge Limits in High Intensity Rings

As detailed in Chapters 5 and 6, the betatron tunes must be kept from rational numbers to avoid potential resonances. The picture is complicated by space charge which extends the

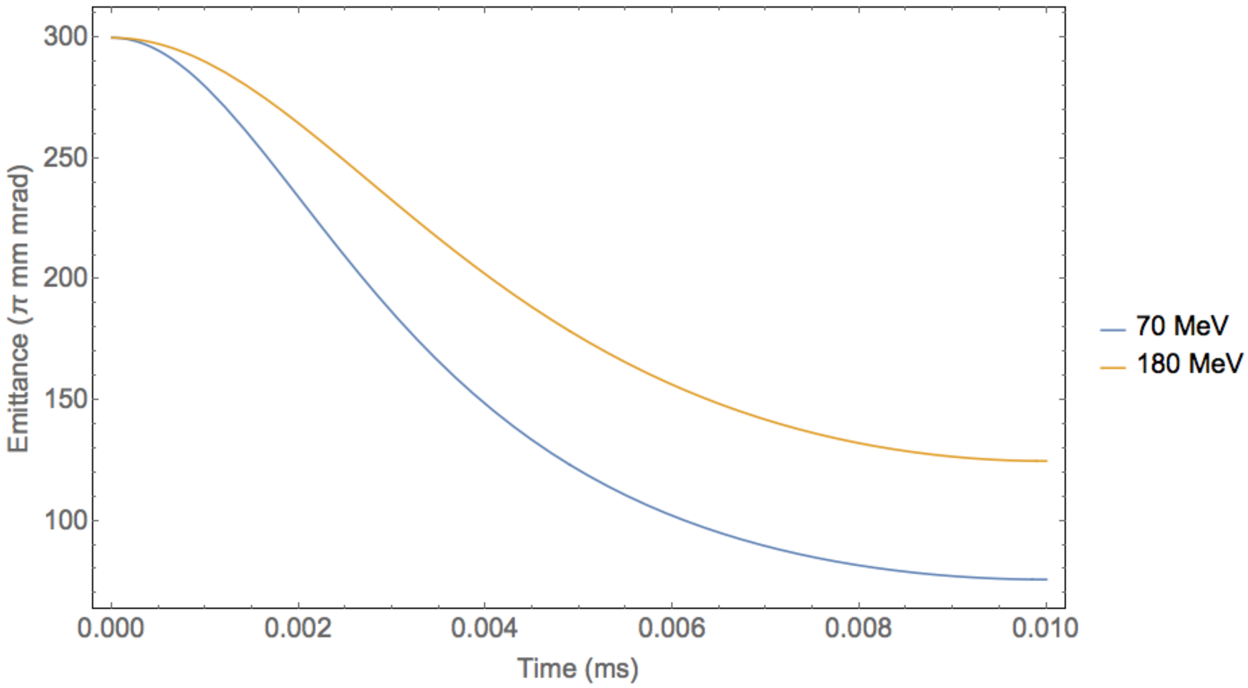

Figure 7.1: Emittance evolution against time for 70 MeV and 180 MeV injection with 300 π mm mrad injected emittance.

dangerous region by spreading out the individual particle tunes.

The space charge tune shift from Equation 7.8 is based on a simplified beam model, and intensity limits estimated from it are crude. The model does not take the self-consistent nature of the beam into account. When the beam is pushed in one way, it can redistribute to compensate, reducing the effective force (the coherent advantage, as explained in Chapter 5).

For this reason the ISIS working point is situated a little over 0.3 above the integer horizontally, and a similar amount over the half integer vertically which prevents the beam from reaching resonance, despite the full tune shift being greater than 0.5. In fact in a real beam neither the incoherent or coherent model is an exact description of the physics and intensity limits generally lie between the predictions of the two models [60]. The process is not fully understood and is the subject of R&D at ISIS and other high intensity machines.

Loss Models and Limits

For this study it was important to check that space charge would not lead to excessive losses at the proposed intensity. The best way to test this in such a complex problem was to use a computer model that included the relevant physics. Therefore details of the accelerator lattice and profiled vacuum vessel, tune control, self consistent space charge, images and likely driving terms all needed to be modelled together if the transverse plane was going to be simulated accurately. Magnetic images from the magnet poles were not included in the simulations, though they will be investigated in an update to this work. Momentum dependent dynamics including dispersion and chromaticity were also not included.

A complete description of space charge loss on a ring like ISIS, including injection, 3D bunching and the fast ramping of parameters during acceleration, is still work in progress and motivating much R&D. For this ISIS upgrade full 3D modelling was explored with the ORBIT code [32]. Even more complete models are being developed in a 3D extension to the in-house code Set, currently being tested. However, it should be noted that the 2D simulations presented here are an essential and fundamental step in showing that the space charge loss processes on ISIS are understood. They provide confidence that the required low loss levels can be achieved.

Simulations Using the Set Code

In this section details of the particle-in-cell simulations used to model important elements of the loss process and to ensure that space charge losses would be as expected are described. Extensive coasting beam simulations were carried out for the upgrade, at intensities up to 2×10^{14} ppp (equivalent to 1×10^{14} ppp bunched beam at the end of injection). These simulations were 2D, without injection, but included the image fields from the conformal rectangular vacuum vessels.

Simulations were performed using the in-house code Set, discussed in more detail in Chapter 3. The model consisted of a 2D waterbag beam distribution which was tracked through transfer matrices and space charge elements. The matrices were split with space charge kicks in the middle of each element. Beam distributions were matched to the first element of the lattice, or RMS matched using simulation results. During a simulation run particle information as well as beam moments, space charge potentials and forces and single particle tunes were all recorded for post-processing.

Intensity scans were carried out for a variety of scenarios: smooth focusing models to compare directly with simple theory; simulations that included the ISIS lattice and conformal vacuum vessel which explored the action of space charge and images; simulations that included half integer driving terms calculated to be representative of those measured on the machine; simulations which included representative harmonic closed orbits. Simulations that explored half integer resonance, harmonic closed orbits and the working point are reported in Sections 7.7, 7.8 and 7.9.

ISIS Lattice Model

The ISIS lattice was included in the simulations as detailed in Chapter 3. The design beam envelope and the conformal vacuum vessel width can be calculated from the beta functions of the machine, and these are shown again for reference in Figure 7.2. Envelope mismatch with the lattice can change the shape of the beam envelope inside the aperture, which will change the image fields from the space charge solver. If the quadrupole strength is changed, or a harmonic variation imposed on the quadrupoles, then the beam envelope will change relative to the ISIS vacuum vessel. In an extreme case the envelope can lie outside the aperture and beam is lost immediately at the start of simulations.

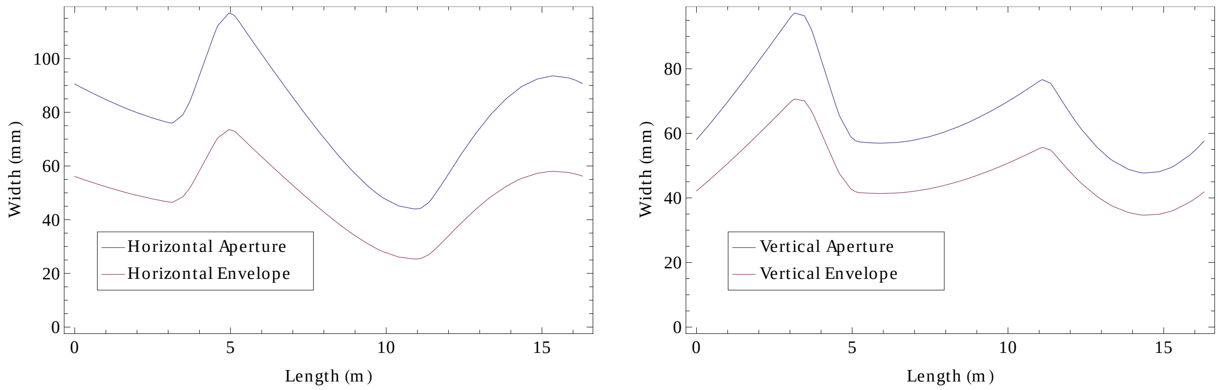

Figure 7.2: Apertures and envelopes for one super period of the ISIS RCS (a) horizontal, (b) vertical.

Space Charge Model

Space charge was calculated using a 2D FFT Poisson solver, which binned the macro-particles into a two dimensional mesh and then solved for the potential. Binning and force interpolation used a cloud-in-cell algorithm. There was a space charge kick for every lattice element - 880 per turn. Image forces were included automatically with application of suitable boundary conditions. The size of the transverse mesh scaled with the conformal boundary in both planes. Simulations used 50000 macro particles and were run for 100 turns. These numbers were chosen following convergence studies. Beams were created automatically using a waterbag distribution randomly generated for each run, and were RMS envelope matched to the lattice. Macro particles were considered lost when they crossed the aperture of the beam-pipe - there was no additional collimation.

Limits Due to Half Integer Gradient Errors

Half integer resonances are believed to be a major component of beam loss on the ISIS synchrotron, and have been the subject of intense study [61, 62, 63]. Harmonic errors with the same representative strength as those measured on ISIS have been included in the Set code, and used to drive resonances in simulations. They are applied with a perturbation to the trim quadrupoles in the lattice. The resulting frequency modulation can be observed in the Fourier transform of the second moment of the beam (beam width or envelope) as shown in Figure 7.3. The amplitude of the frequency signal grows as the 2$^{\text{nd}}$ moment nears the driving term and hence resonance.

The nearest half integer resonance lines to the working point of the synchrotron are $2Q_H = 8$ and $2Q_V = 7$. Simulations with both of these driving terms present were studied, and there was similar behaviour in each case. However, on the actual RCS, as the beam is

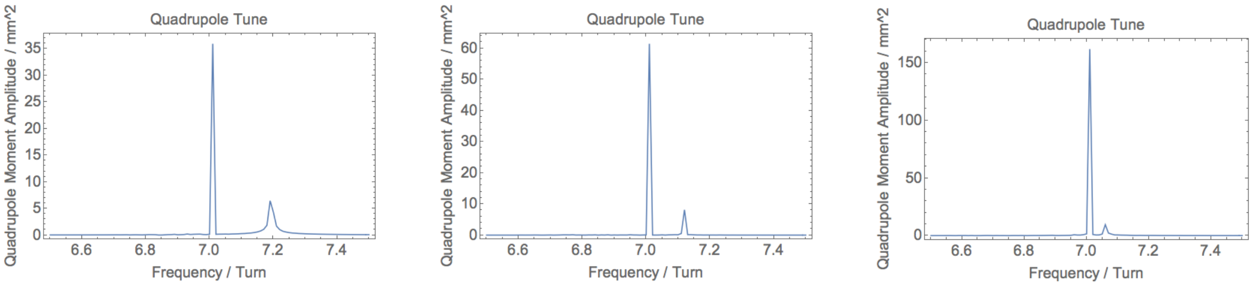

Figure 7.3: Vertical 2$^{\text{nd}}$ moment frequency at intensities of 1.5, 1.75 and 2×10^{14} ppp. The driving term at $2Q_H = 7$ is clearly visible. As the intensity increases the 2$^{\text{nd}}$ moment approaches the driving term.

smaller and there is no dispersion in the vertical plane, it is expected that half integer effects will be encountered first in the vertical. Therefore the simulations reported here contain only the vertical driving term and focus on the vertical plane.

Results with Half Integer Gradient Errors

A set of simulations was run in which the starting intensity was varied from 0 - 2×10^{14} ppp coasting beam. Figure 7.4 shows the results of these simulations. In the top plot, the second moment frequency (half integer or envelope) calculated from the macro-particle bunch was plotted against intensity. It can be seen from both this and the second plot looking at the amplitude of the second moment that the beam was disturbed as it approached the resonance at $2Q_V = 7$. There was a corresponding growth in beam loss at the highest intensity. Beam loss in this context was not a prediction of actual losses but an indication of when the intensity limit was reached.

Significant macro-particle loss (approaching 1%) occurred above coasting beam intensities of 1.75×10^{14} ppp - equivalent to 8.8×10^{13} ppp with the expected bunching factor of 0.5. This implies that space charge related losses should be at tolerable levels for the proposed upgrade though careful loss control will be required. Existing mechanisms such as control of the tune with trim quadrupoles and ability to apply harmonic error corrections will be required. There are additional programmes in place to improve these systems and diagnostic tools to measure the transverse dynamics of the beam and it is anticipated such features will be required for future high intensity operation [64].

At the highest intensity investigated, 2×10^{14} ppp, the development of half integer lobes was evident in the vertical phase space bunch structure, shown in Figure 7.5. For this example, the conformal vacuum vessel was moved out to twice its normal extent to allow the lobes to form without being lost against the aperture.

Gradient Error Summary

Beam behaviour was studied, with increases to intensity used to approach half integer resonance. It was expected that envelope oscillations would increase as the coherent resonance

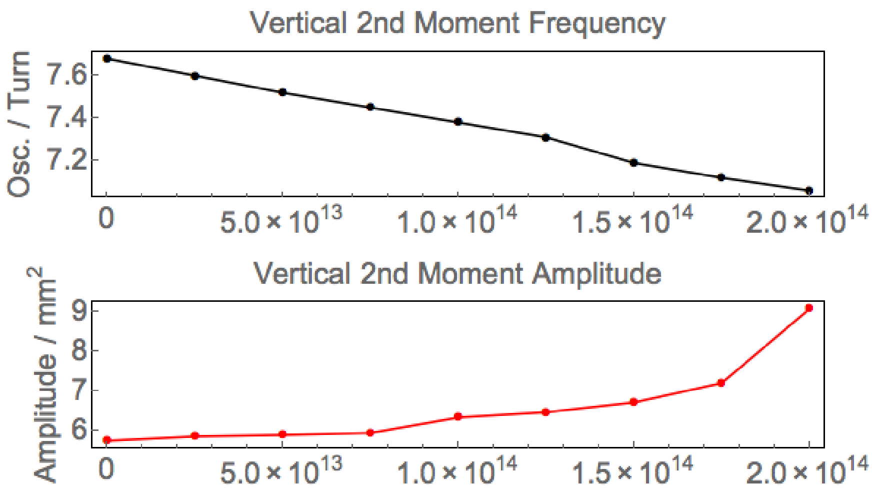

Figure 7.4: Results of set of simulations at different intensities including representative vertical half integer driving terms.

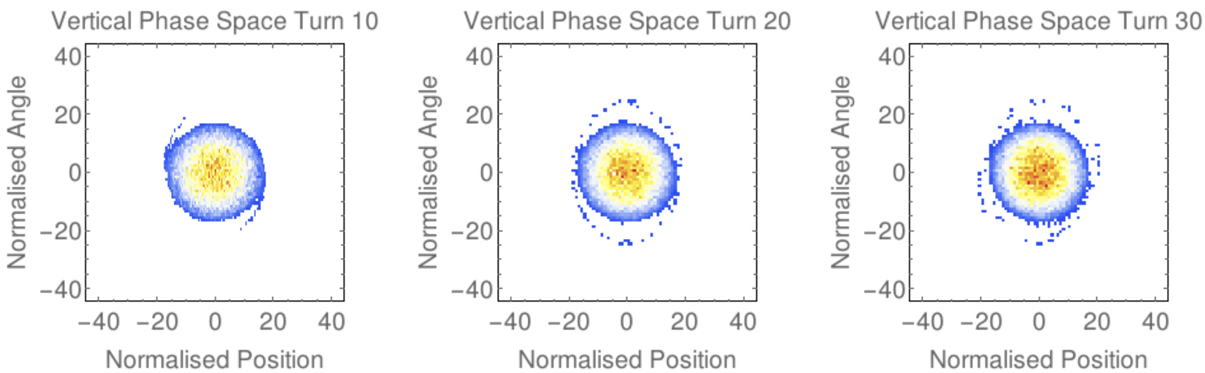

Figure 7.5: Normalised vertical phase space at 10, 20 and 30 turns for a bunch at coasting beam intensity 2×10^{14} ppp, clearly showing the development of half integer lobes. The conformal vacuum vessel has been moved out to twice the normal extent to allow the lobes to develop.

was approached and that was observed in the second moment amplitude. The coherent motion occupies more of the aperture and can itself lead to beam loss. As envelope oscillations became large, the beam redistributed, emittance increased, halo particles were generated and beam was lost. Whilst many details were not included in the model, the results indicated that half integer resonance should not generate large levels of loss within the design apertures until the intensity is significantly above the proposed running level.

Simulations Including Representative Harmonic Closed Orbits

Simulations were run to study the combined effect of half integer quadrupole errors along with horizontal and vertical harmonic closed orbits. All of the errors were roughly representative, though the closed orbits were a factor of two larger than ISIS runs with operationally.

In this section the simulations carried out in Section 7.7 were modified by the inclusion of harmonic closed orbits in both planes, in the same manner as in Chapter 5. For this section closed orbits were generated in both the horizontal and vertical planes. Kicks distributed around the lattice were used to drive 4^{th} harmonic closed orbits in both planes. As in Section 7.7, representative vertical quadrupole errors were also included, providing a half integer driving term at $2Q_V = 7$. The simulations included the conformal vacuum vessels. Preliminary simulations were run several times in order to find optimised values for the resulting closed orbit and Twiss parameters of the input beam, taking intensity into account. This information was then used to match the randomly generated waterbag distribution input beams.

The operational closed orbits at ISIS are corrected to less than 5 mm, and in most case better than 3 mm. However for these simulations a pessimistic value of ∼10 mm was used. An example at an intensity of 1.75×10^{14} ppp is shown in Figure 7.6. The orbit for every 10^{th} turn is overplotted showing the match. The 4^{th} harmonic structure, modulated by the beta functions, can clearly be seen.

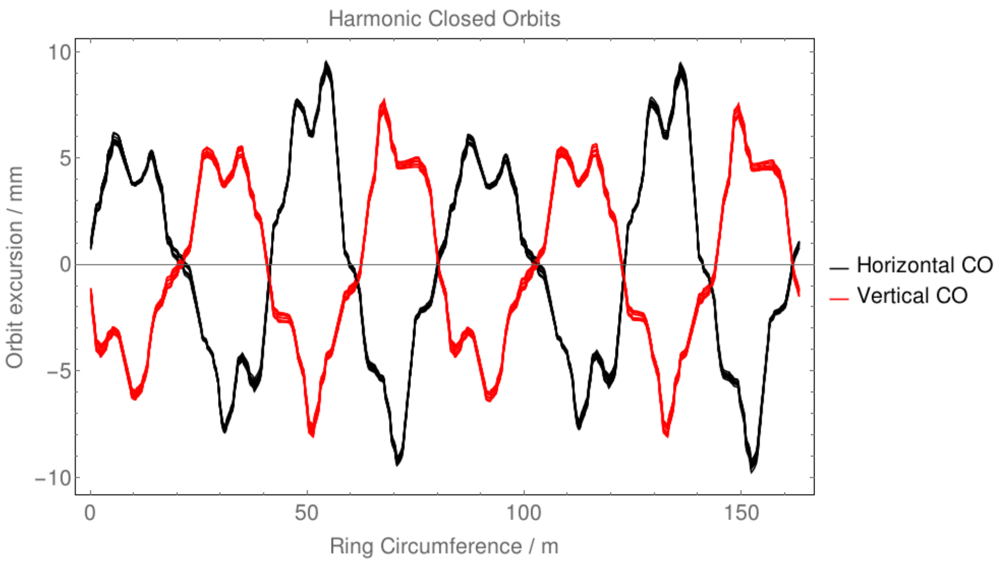

Figure 7.6: Matched 4^{th} harmonic closed orbits in both planes, with the orbits overplotted every 10 turns, at an intensity of 1.75×10^{14} ppp.

Two coasting beam intensities were simulated, one at 1.75×10^{14} and one at 2×10^{14} ppp. It should be noted that these intensities are slightly above the nominal proposed intensity for the upgrade. In both cases there was additional halo formation and beam loss beyond what was observed without the closed orbits, with beam loss approaching 10% at the higher intensity.

Figure 7.7 shows normalised horizontal and vertical phase space on turns 20, 30 and 40, at an intensity of 1.75×10^{14} ppp. The simulations included both representative half integer errors and matched closed orbits. In the horizontal plane, a first order resonance is visible, with the formation of a single lobe. Meanwhile in the vertical plane, half integer resonance is increased compared with the same intensity without closed orbits. Beam loss is enhanced over the simulations without closed orbits. A tune diagram for the simulation with intensity 2×10^{14} ppp is shown in Figure 7.8, showing where the single particle tunes lie over the $Q_H = 4$ integer and $2Q_V = 7$ half integer resonances.

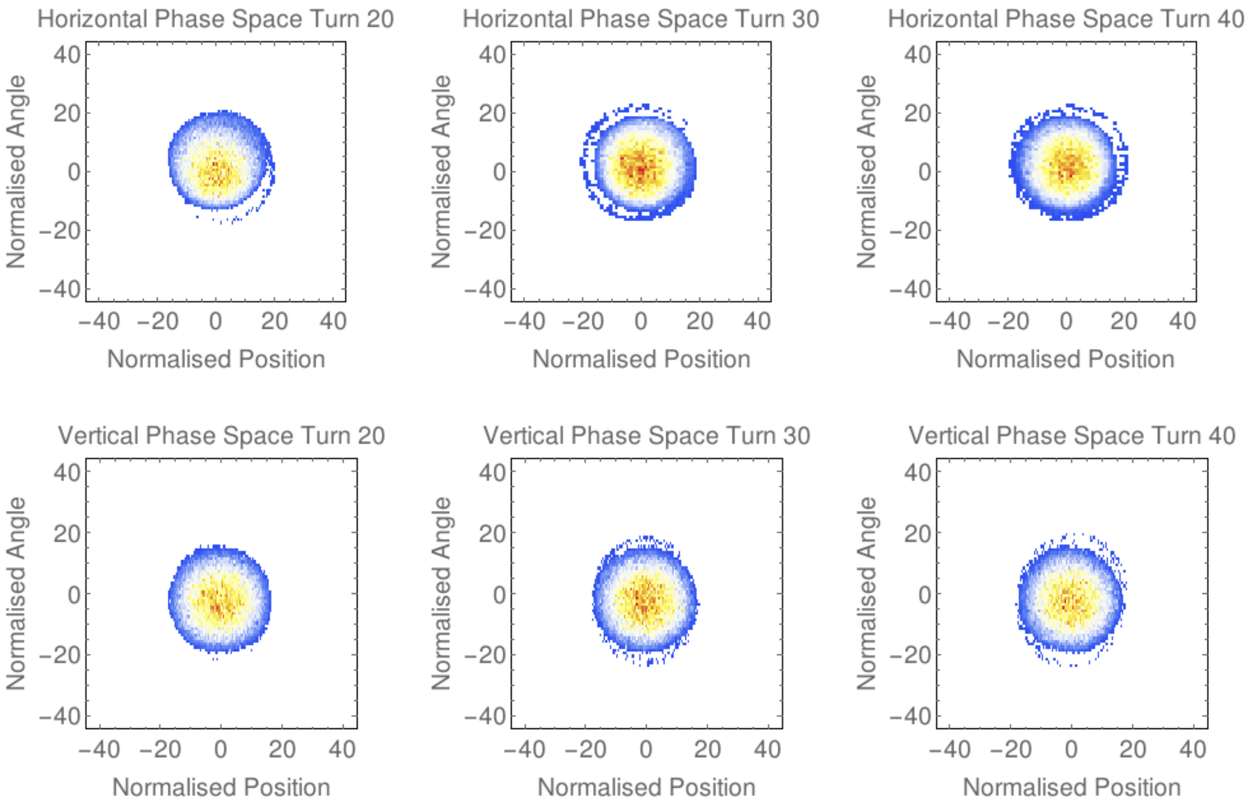

Figure 7.7: Normalised horizontal and vertical phase space on turns 20, 30 and 40, at an intensity of 1.75×10^{14} ppp. The simulations included both representative half integer errors and matched closed orbits.

Figure 7.9 shows the same phase space plots for an increased intensity of 2×10^{14} ppp. At this intensity loss is increased by a factor of 10, to almost 10% of the macroparticles, over 100 turns. The first order resonance in the horizontal plane and the second order resonance in the vertical plane are both clearly visible. Nearly all of the beam loss occurs in the vertical plane.

The precise cause of loss is difficult to determine as several effects are interacting. The beam is starting to resonate as the second moment approaches the half integer driving term, but image effects are enhancing the resonance and pushing more beam into the halo. The closed orbits are also reducing the effective available aperture of the machine and the envelope

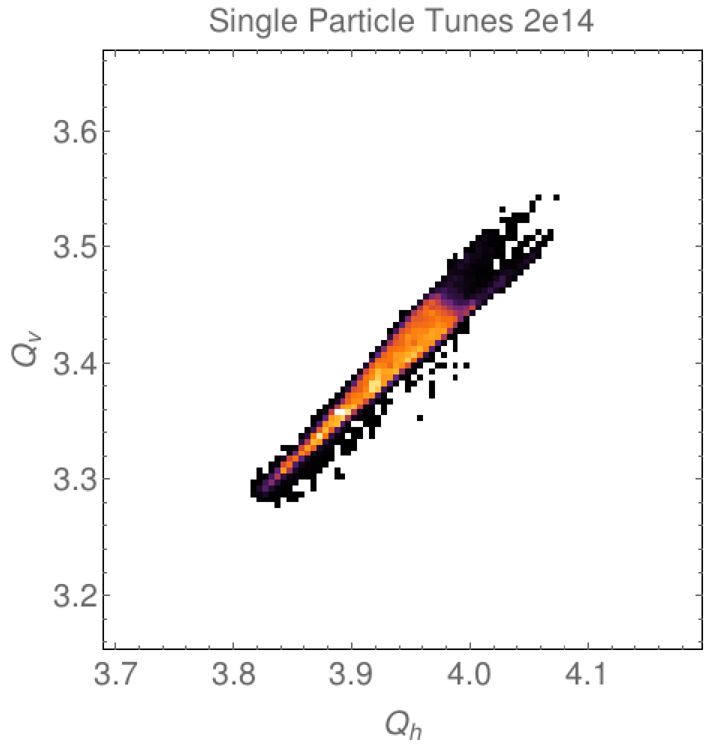

Figure 7.8: Tune diagram for simulation with both representative half integer errors and matched closed orbits at an intensity of 2×10^{14} ppp. The individual tunes of many particles lie over the $Q_H = 4$ integer and $2Q_V = 7$ half integer resonances.

is not matched to the conformal vacuum vessel. This is clearly a situation to be avoided operationally. This combined resonance structure may be the reason 4^{th} harmonic closed orbits must be carefully corrected at the highest intensities at ISIS, as reported by Rees and Prior [47].

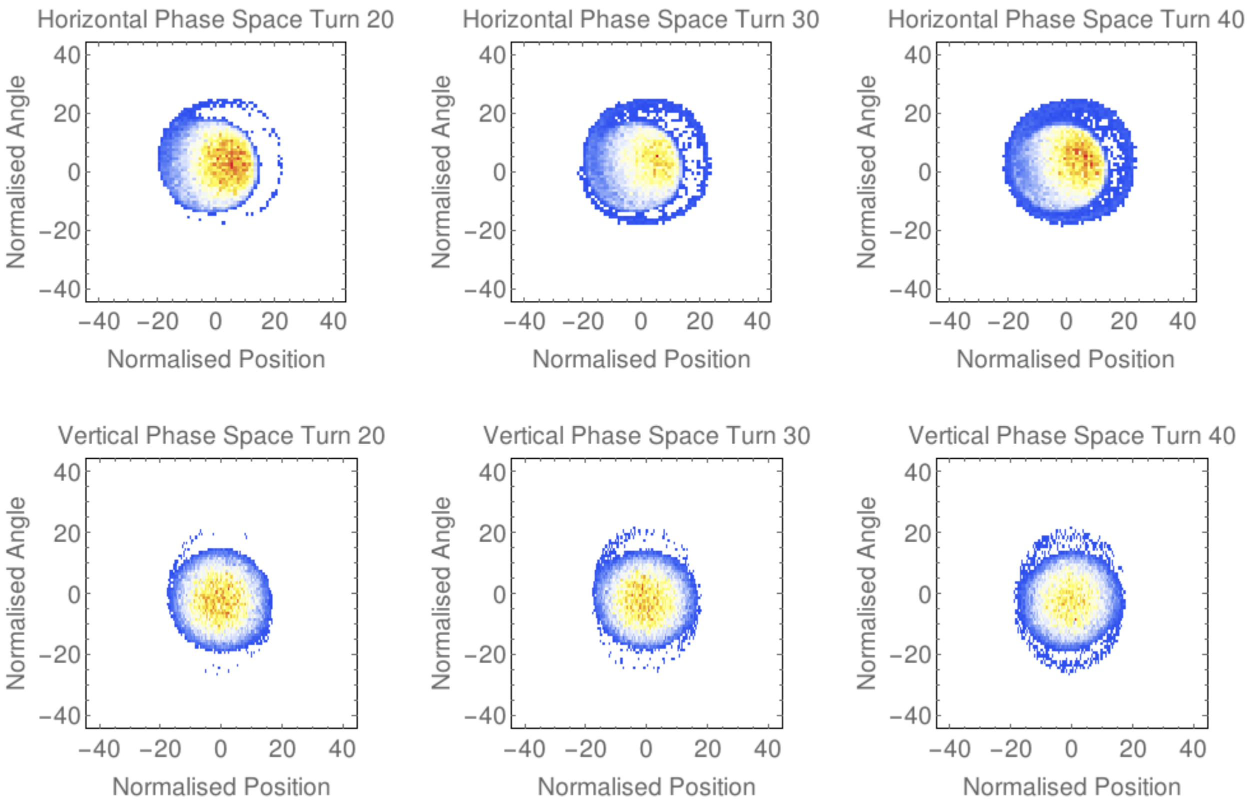

Figure 7.9: Normalised horizontal and vertical phase space on turns 20, 30 and 40, at an intensity of 2×10^{14} ppp. The simulations included both representative half integer errors and matched closed orbits.

Simulations Moving the Working Point

Simulations have been run which explored moving the vertical tune above the integer or below the half integer. A new working point might help mitigate concerns about instabilities for the upgrade. These simulations looked at the effect of the working point on envelope in the conformal aperture but also explored the role of space charge and resonances.

ISIS suffers from a resistive wall head-tail instability when the vertical tune is just below 4 which limits the intensity of the machine. On the existing machine the instability occurs after space charge has peaked between 1 and 2 ms. To avoid the instability the vertical tune is reduced. For the upgrade, peak space charge will coincide with the end of injection. Therefore it may prove difficult to move the tune at this time due to loss associated with the half integer resonance. One option being explored to alleviate the situation is to use an active damping system to control the instability [25]. Another is to move the working point of the machine away from the instability, which is explored below.

The working point must be kept far enough above linear (integer and half integer) resonances to avoid beam loss. In the vertical plane the nearest safe options are to move the tune below 3.5, or to above 4.3 and both of these points were investigated. There is a complication however. At ISIS the vacuum vessel aperture has been manufactured in the shape of the design beam envelope, along with compensation for dispersive and closed orbit effects. This was done to mitigate instabilities, but it also limits how far the working point can be changed before the beam envelope moves too close to the vacuum vessel. The design envelope functions were shown in Figure 7.2.

Two alternatives to the design working point were investigated. One option moved $\mathrm{Q_v}$ below the half integer, and the other moved it above 4.3. For both points the impact on the beam envelope was assessed.

Working Point 1: $(\mathrm{Q_h}, \mathrm{Q_v}) = (4.31, 3.49)$

Adjustments to the trim quadrupoles were made to move the vertical tune to 3.49 while leaving the horizontal tune unchanged. The effect on the beam envelope can be seen in Figure 7.10 (a). The available aperture was reduced in the second half of the super period which may cause issues with beam loss, or demand challenging control of the beam orbit. The reduced aperture was of significant concern, potentially increasing images forces and losses. Further simulation results showed that the lattice was not stable at this value of the tune. The third moment of the beam was also located much nearer to the image driven resonance at $3Q_v = 10$, previously observed in Chapter 5, which would have been passed through during injection of the beam. For these reasons this working point was rejected as a suitable candidate for the upgrade.

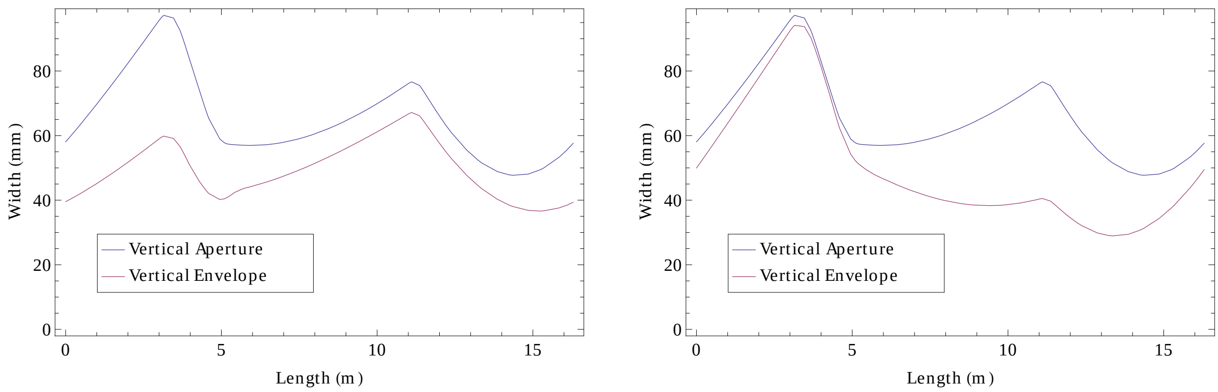

Figure 7.10: Vertical envelope and aperture for (a) $(\mathrm{Q_h}, \mathrm{Q_v}) = (4.31, 3.49)$ and (b) $(\mathrm{Q_h}, \mathrm{Q_v}) = (4.31, 4.36)$.

Working Point 2: $(\mathrm{Q_h}, \mathrm{Q_v}) = (4.31, 4.36)$

When the vertical tune was moved above 4.3, in this case to 4.36, the situation was quite different. As can be seen from Figure 7.10 (b), the envelope of the test beam was now tightly constrained by the aperture. Even at zero space charge some of the beam was clipped by the aperture. In addition simulation studies showed that at this working point there was coupling between the horizontal and vertical planes. As the aperture was narrower in the vertical plane, image effects caused the vertical tune and higher moments of the beam to drop faster than the horizontal. When the vertical tune passed through the horizontal the beam was disturbed by emittance exchange which showed up in a characteristic rippling on the emittances. More simulations were run to show that if, in addition, the horizontal tune was raised above the new vertical value this emittance exchange could be eliminated. However due to the overlap of beam envelope and beam pipe this working point was also discarded.

Working Point Summary

The simulations used to study the beam envelope change within the conformal vacuum vessel could be improved with further iterations also allowing the main quadrupoles to vary. Further studies may show improvements over the results here. However at a basic level, if the tune is modified it changes the beta function, which will always modify the envelope compared to the ISIS vacuum vessel. Unless the vacuum vessel were also modified, it is suggested that the design tune numbers be kept.

Non-Linear Driving Terms Measured During Low Intensity Experiments

The main space charge loss mechanisms on the ISIS ring are expected to be related to the half integer limit, image terms and possibly space charge driven structure terms. However new and detailed experimental investigations (Chapter 6) of resonance lines at low intensity have shown that some significant non-linear driving terms are present in the ISIS lattice, Figure 6.8. Although these probably have a small effect compared with the terms described above, some further simulation studies will be undertaken to see if these terms have any effects on beam loss levels. These could have important implications for optimisation of the machine.

New simulations and measurements of the ISIS trim quadrupoles have been made [57] and higher order field components are present in the fields. It is also planned to simulate and measure the main ring dipoles and quadrupoles in more detail. In the future simulations will include these more accurate field components and compare them with the experimental observations.

Summary

Transverse dynamics considerations are a crucial part of the argument for an upgrade of the ISIS injector to 180 MeV.

The reduction in space charge forces is a key motivation for the upgrade, and is achieved by a combination of the higher energy and an increase in peak bunching factor due to optimised injection. Application of analytical scaling laws suggests that ISIS intensity could be increased by more than a factor of 3. This indicates that beam powers of 0.5 MW should be possible maintaining allowable losses due to space charge.

Changes to injection energy and therefore a reduction in the total energy ramp reduce the adiabatic damping of emittance and therefore will require an upgrade to the extraction channel to accommodate the larger 800 MeV beam.

Extensive and detailed 2D simulations that include details of the lattice, self-consistent space charge, images, realistic apertures, space charge driven resonances and half integer driving terms indicate losses should be as predicted and within allowable limits. These simulations are at the nominal working point and assume instabilities are controlled.

Simulations incorporating both half integer driving terms as well as harmonic closed orbits suggest that, if the upgrade is pushed to higher intensities, there will need to be a careful optimisation of closed orbits to minimise the effect of image driving terms interacting with the beam.

Simulations at alternative working points, designed to avoid the head-tail resistive-wall instability, indicate high intensity effects may introduce difficulties with higher order resonances, but that these are probably manageable. However the key finding was that the changes in beam envelope with respect to the conformal ISIS vacuum vessels, associated with the tune changes, lead to an effective reduction in usable machine apertures that make these options unworkable. Replacement of machine vacuum vessels and RF shields could be one solution: damper systems for the instability are the more obvious solution.

Future work will continue to develop in-house simulations with the inclusion of full injection and longitudinal motion, which will allow the simulation results discussed here to be put into their proper context. Simulations will be extended with both the measured non-linear resonance driving terms from Section 7.11 and new measurements of ISIS magnets. These additions to the simulations will allow the most accurate models of the synchrotron so far.

Chapter 8

Conclusion

The main achievements of the thesis are reported here, along with short sections outlining ideas for future work.

ISIS and the Proposed 180 MeV Injection Upgrade

A detailed overview of ISIS and the 180 MeV Injection Upgrade was provided, with particular emphasis on the transverse plane.

Simulations for Image Field Analysis and Investigation of 2D Beams in Smooth Focusing and Alternating Gradient Lattices

Thesis Achievements

The Set code was introduced. An overview of its components was given, including space charge solvers and lattice algorithms. The space charge solvers were benchmarked against commercially available algorithms. The ability to customise and modify the code so that it could be focused on a particular task was invaluable for the rest of the thesis.

Future Work

Investigation should be carried out into methods to solve for the space charge and image fields separately, so that the correct boundary conditions can be applied to each. Magnetic image terms can then also be included.

A parallel 3D extension to Set is under development, which includes dispersion, injection and acceleration.

Further development of the FEA solver will allow the inclusion of different geometry boundaries (circular, elliptic) as well as a fast matrix solution, making it much more competitive with the FFT solver for beam tracking simulations.

Image Field Terms for Uniform Beams in Rectangular Geometry

Thesis Achievements

Analysis for 1D image fields from pencil beams in parallel plate geometry, and for centred beams in rectangular geometry was summarised. Image field coefficients to third order in y and $\bar{y}$ were defined.

The image coefficients were compared with the output of 2D simulations with round, uniform beams in rectangular geometry. For centred beams the analysis was a good fit. For off-centred beams the image coefficients were plotted for different values of beam offset and aspect ratio. A table of values for coefficients in square and aspect ratio 3 rectangular geometry was produced. Where these coefficients are larger than their parallel plate values, they indicate a larger driving term which may lead to enhanced beam loss.

Values for the image coefficients in the orthogonal plane were found to be non-zero in some cases, and for these cases the coefficients were also plotted. An overview of how 2D image potentials might be constructed was given.

Future Work

It seems possible that a solution for the full 2D beam image could be represented in terms of an expansion of the magnetic vector potential. This solution will be investigated using the tools of conformal mapping and elliptic functions, which have been used successfully to obtain image coefficients. A solution, if it exists, will enable fast and simple estimation of image coefficients and provide access to coupling terms which are otherwise difficult to calculate.

Beam Response to Image Terms

Thesis Achievements

Solutions were derived for closed orbits at low intensity. The effect of intensity and images on those orbits was discussed. Numerical solutions were shown to exist for closed orbits at high intensity.

Assuming the existence of a stable closed orbit, the image coefficients derived in Chapter

4 were then included in the equation of motion. Image coefficients were tabulated in terms of order, coordinate dependence and closed orbit harmonic.

A Hamiltonian was then constructed, with the image coefficients included in potential form, with the dynamics analysed with respect to the closed orbit. The Hamiltonian was transformed to action-angle coordinates. For examples thought to be relevant to ISIS, the image coefficients were expanded in terms of the transformed coordinates and the equation for the closed orbit. Expected resonant conditions were identified. The expected effects of coherent motion on the results was discussed.

2D simulations were carried out for a range of conditions. A smooth focusing lattice and KV beam was the simplest possible arrangement and could be conveniently compared with theory. Image driven resonances identified in the preceding analysis were located and explored. Some unanticipated behaviour was identified, including new resonances that were not predicted by the theory. More sophisticated simulations including waterbag beams, an alternating gradient lattice and conformal vacuum vessels were carried out. Image resonances were identified for each parameter arrangement. Implications for ISIS were discussed.

Future Work

The effect of additional coefficients should be studied, including dynamics of centred beams and coupling terms. A theoretical framework for image driving terms that arise from modulation of the vacuum vessel should be investigated. More sophisticated simulations including 3D dynamics, momentum dependent effects, injection and acceleration should be run as they become available.

Experimental Studies Investigating Betatron Resonances on the ISIS Synchrotron

Thesis Achievements

New experiments have measured beam loss and intensity with low intensity coasting beams at the ISIS Synchrotron, as a function of betatron tune. The results clearly show resonance lines which indicate magnet non-linearities, errors or misalignments present in the machine. These measurements are the most detailed of their kind carried out at ISIS.

The experiments required configuring into ISIS a special running state, storage ring mode, and performing careful, systematic measurements. The experiments have been repeated several times with different settings, with the best measurements recorded in the thesis. The method will be re-used for future experiments.

These measurements are essential for understanding future, high intensity experiments including measurements of space charge and image induced beam loss, where the low intensity driving terms must be treated as a background.

Future Work

The new measurements will be compared with models of ISIS magnets including higher order fields to see whether some of the driving terms can be identified in the nominal ISIS lattice. It may be possible to determine the origin of other driving terms through the use of particle tracking simulations.

Future simulation studies of ISIS will incorporate the driving terms to better represent the lattice environment.

More experiments are planned looking at tune vs loss at higher intensities and also with bunched, coasting beams. Individual resonance lines will be investigated. An important long term goal is the identification of beam loss due to image driving terms created with harmonic closed orbits.

An Assessment of Transverse Dynamics for the 180 MeV Injection Upgrade for ISIS

Thesis Achievements

Important transverse dynamics topics, related to high intensity space charge and images, for the 180 MeV Injection Upgrade for ISIS were surveyed.

The incoherent space charge tune shift was derived and calculated, leading to a working value for the intensity obtainable with the upgrade. The higher energy injection of the upgrade modifies how emittance scales during acceleration. The implications for extraction from the upgraded ring were discussed.

PIC simulations used to study the upgrade were introduced, and then detailed studies carried out in areas of concern. Simulations including half integer gradient errors suggested that beam re-distribution due to the half integer resonance was not likely to be a concern, as it occurred above the proposed intensity level.

Simulations including both gradient errors and harmonic closed orbits showed that image effects could lead to new resonant effects and exacerbate beam re-distribution. The closed orbits used in the simulations were large and targeted a specific harmonic, so such image contributions are expected to be small. The intensity was also higher than the proposed intensity.

Modification of the working point to avoid a vertical instability was found to reduce the available aperture due to the change to the beam envelope. Unless the vacuum vessels were also altered such changes were not desirable and other options for mitigating the instability should be pursued for the upgrade.

Overall it was found that the upgrade should be feasible, from the studies of transverse dynamics made so far.

Future Work

Simulations should be extended to include resonances identified in the experiments in Chapter 6, associated with measured magnet error fields or otherwise. As more sophisticated simulation tools including injection, acceleration and momentum dependent effects become available the results included here will be updated.

As better models for images and image resonances are developed they will be incorporated into the upgrade studies. The effect of the conformal vacuum vessel needs to be quantified, including relevant longitudinal dynamics costs and benefits. Conformal vacuum vessels in general, including rectangular and other geometries, should be assessed for use in future high intensity accelerators.

Appendix A

Poisson Solver Benchmarking

Uniform Beam Offset by 25 mm Horizontally

Simulation results for a 50 mm radius, uniform beam, with the beam offset by 25 mm horizontally, in an aperture of $\pm$ 100 mm in both planes are demonstrated. The charge distribution is shown in Figure A.1. The mesh is a 200×200 cell grid for the FFT solver, with similar resolution for the FEA solver. The resulting potential distribution is shown as a contour plot and 3D plot in Figure A.2 (a) and (b) respectively.

The error between the solvers, and an equivalent case calculated using Mathematica, is shown in Figures A.3 and A.4. Figure A.3 (a) is a comparison between the values of the two potentials along a centre line through the grid, while (b) shows the relative error as a 3D plot, with an overall accuracy greater than 0.03%. Figure A.4 shows the same values for the FEA solver, with an overall error less than 0.1%.

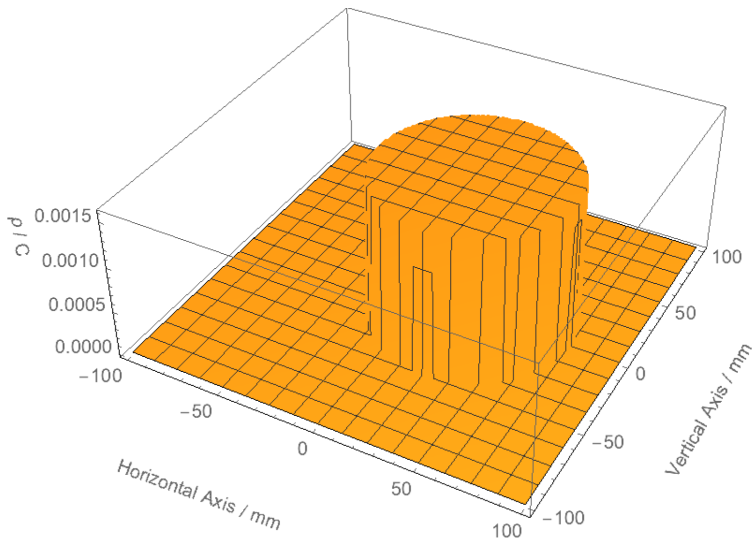

Figure A.1: Circular, uniform density 4π charge distribution offset by 25 mm horizontally used in Mathematica model.

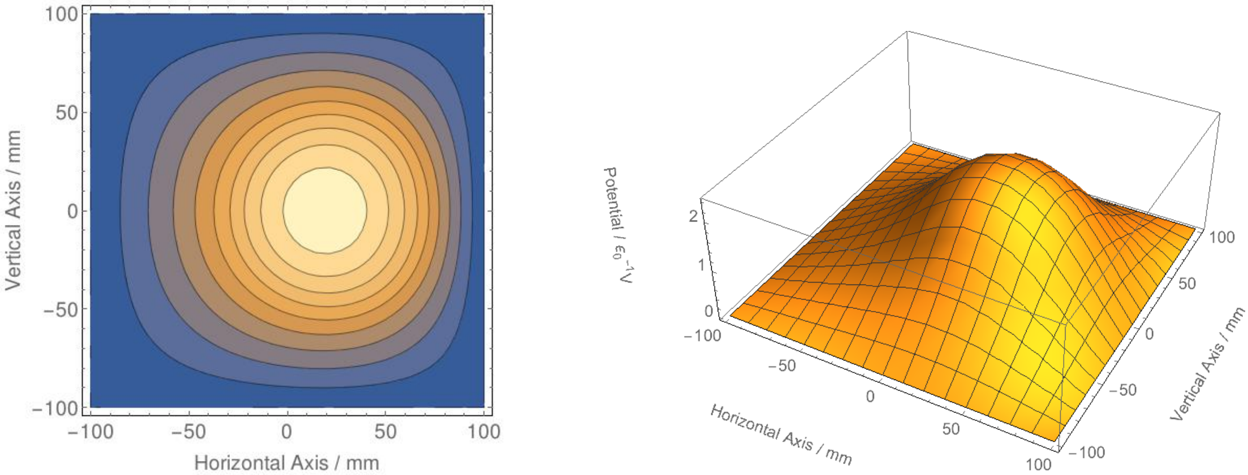

Figure A.2: Contour plot (a) and 3D plot of potential produced in Mathematica model, with beam offset by 25 mm horizontally.

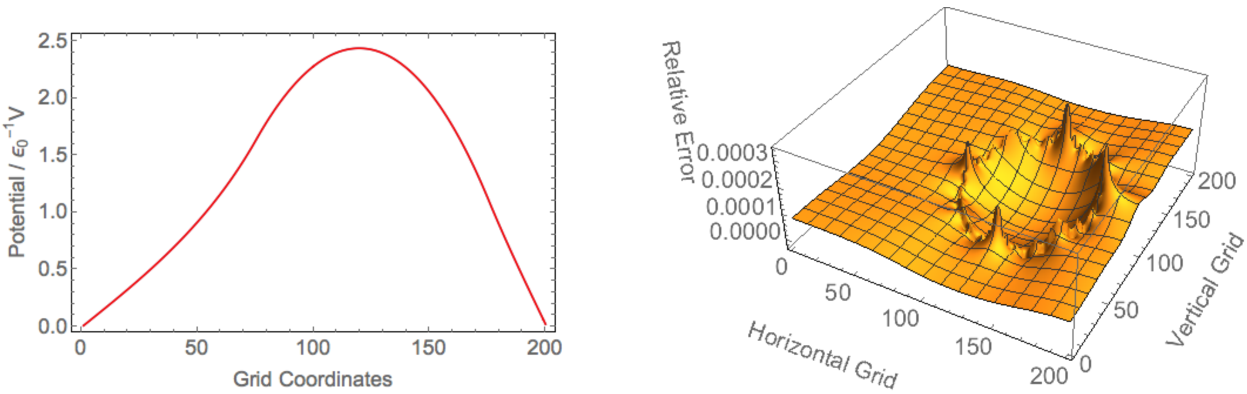

Figure A.3: FFT Poisson Solver with uniform beam compared to Mathematica solution, with beam offset by 25 mm horizontally (a) comparison of centre line, (b) 3D plot of relative error.

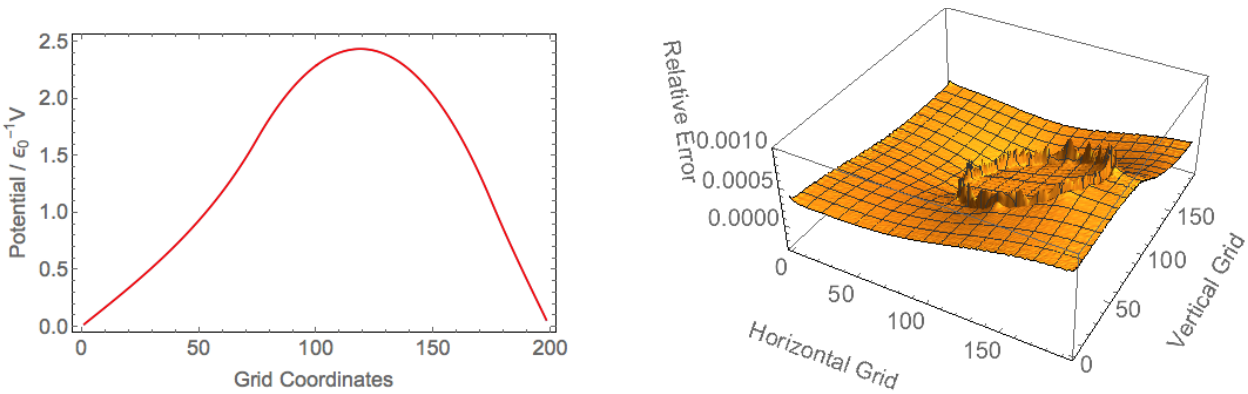

Figure A.4: FEA Poisson Solver with uniform beam compared to Mathematica solution, with beam offset by 25 mm horizontally (a) comparison of centre line, (b) 3D plot of relative error.

Uniform Beam Offset by 25 mm Horizontally and Vertically

Simulation results for a 50 mm radius, uniform beam, with the beam offset by 25 mm horizontally and vertically, in an aperture of $\pm$ 100 mm in both planes are demonstrated. The charge distribution is shown in Figure A.5. The mesh is a 200×200 cell grid for the FFT solver, with similar resolution for the FEA solver. The resulting potential distribution is shown as a contour plot and 3D plot in Figure A.6 (a) and (b) respectively.

The error between the solvers, and an equivalent case calculated using Mathematica, is shown in Figures A.7 and A.8. Figure A.7 (a) is a comparison between the values of the two potentials along a centre line through the grid, while (b) shows the relative error as a 3D plot, with an overall accuracy greater than 0.03%. Figure A.4 shows the same values for the FEA solver, with an overall error less than 0.1%.

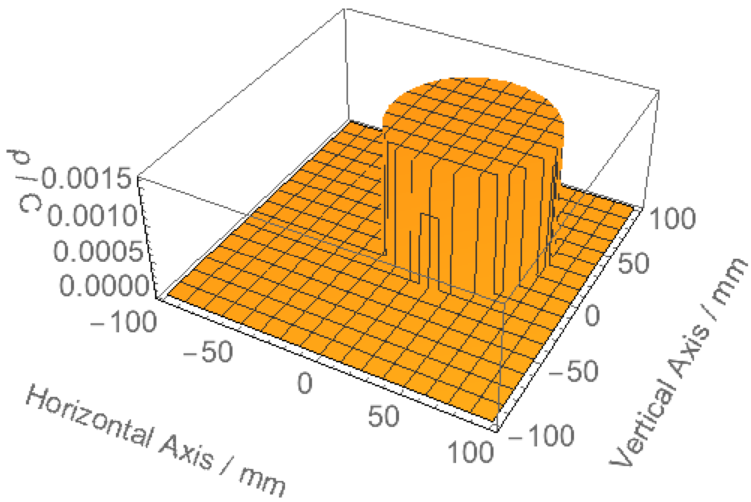

Figure A.5: Circular, uniform density 4π charge distribution offset by 25 mm horizontally and vertically used in Mathematica model.

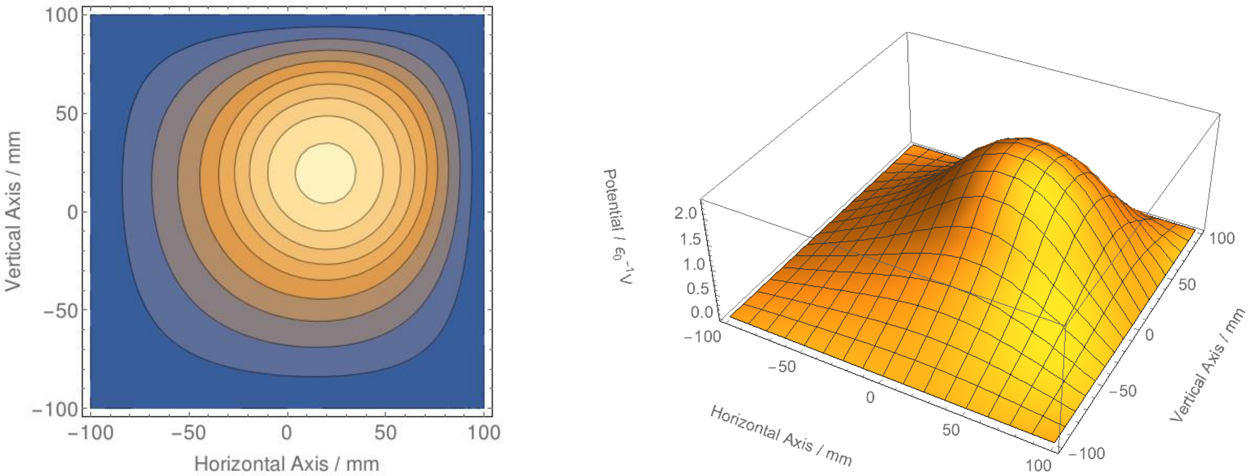

Figure A.6: Contour plot (a) and 3D plot of potential produced in Mathematica model, with beam offset by 25 mm horizontally and vertically.

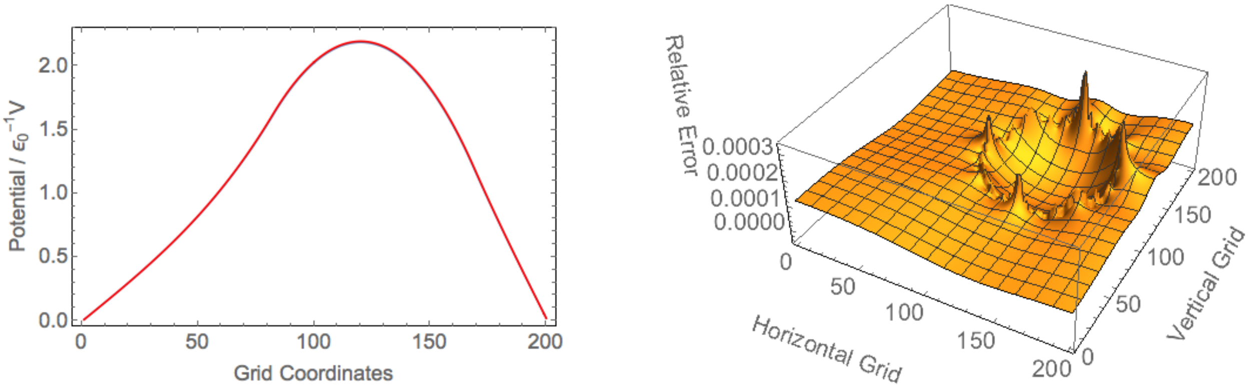

Figure A.7: FFT Poisson Solver with uniform beam compared to Mathematica solution, with beam offset by 25 mm horizontally and vertically (a) comparison of centre line, (b) 3D plot of relative error.

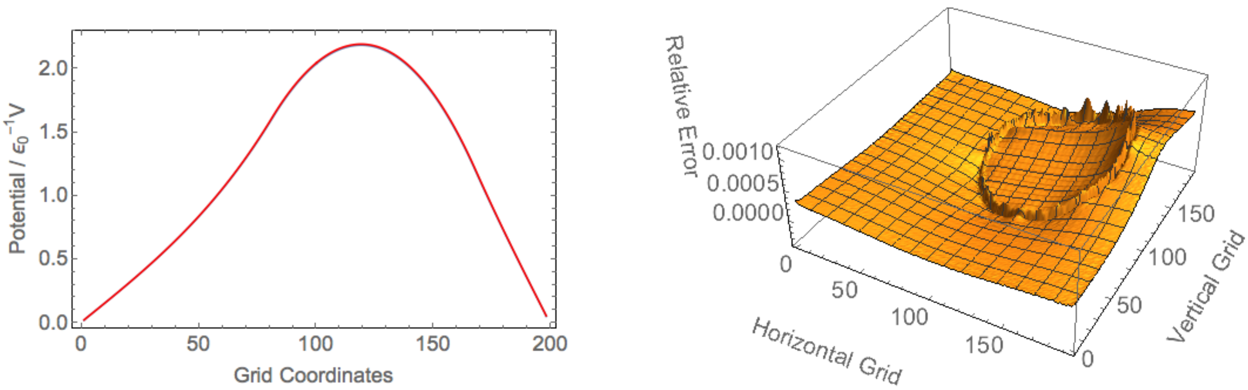

Figure A.8: FEA Poisson Solver with uniform beam compared to Mathematica solution, with beam offset by 25 mm horizontally and vertically (a) comparison of centre line, (b) 3D plot of relative error.

Small Uniform Beam

Simulation results for a 10 mm radius, uniform beam, in an aperture of $\pm$ 100 mm in both planes are demonstrated. The charge distribution is shown in Figure A.9. The mesh is a 200×200 cell grid for the FFT solver, with similar resolution for the FEA solver. The resulting potential distribution is shown as a contour plot and 3D plot in Figure A.10 (a) and (b) respectively.

The error between the solvers, and an equivalent case calculated using Mathematica, is shown in Figures A.11 and A.12. Figure A.11 (a) is a comparison between the values of the two potentials along a centre line through the grid, while (b) shows the relative error as a 3D plot, with an overall accuracy greater than 0.4%. Figure A.12 shows the same values for the FEA solver, with an overall error less than 0.6%.

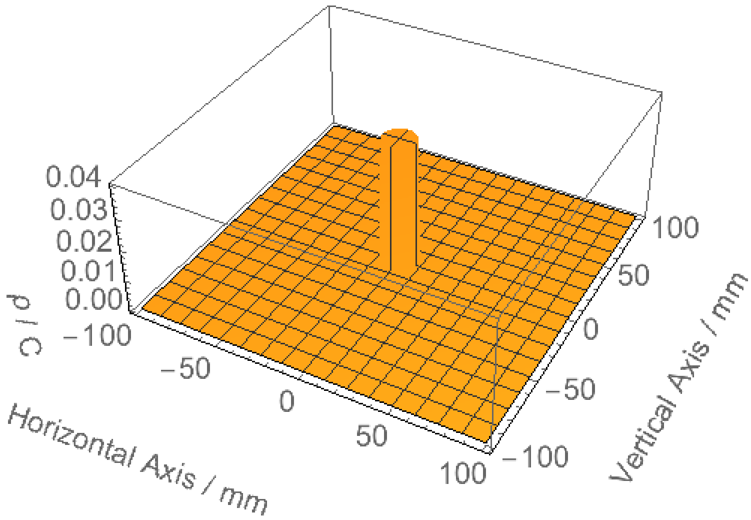

Figure A.9: Small, circular, uniform density 4π charge distribution used in Mathematica model.

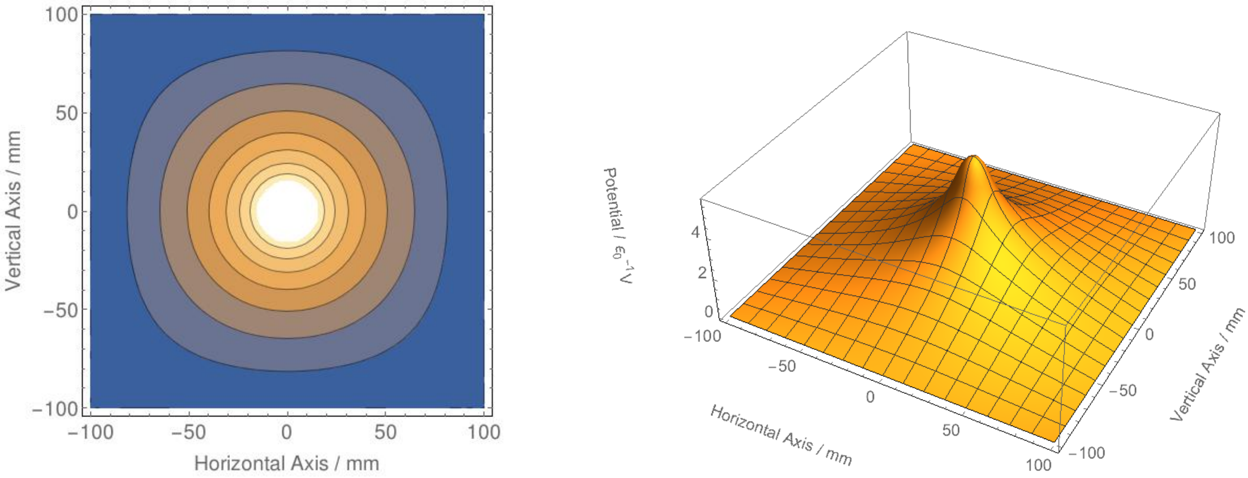

Figure A.10: Contour plot (a) and 3D plot of potential produced in Mathematica model, with small beam.

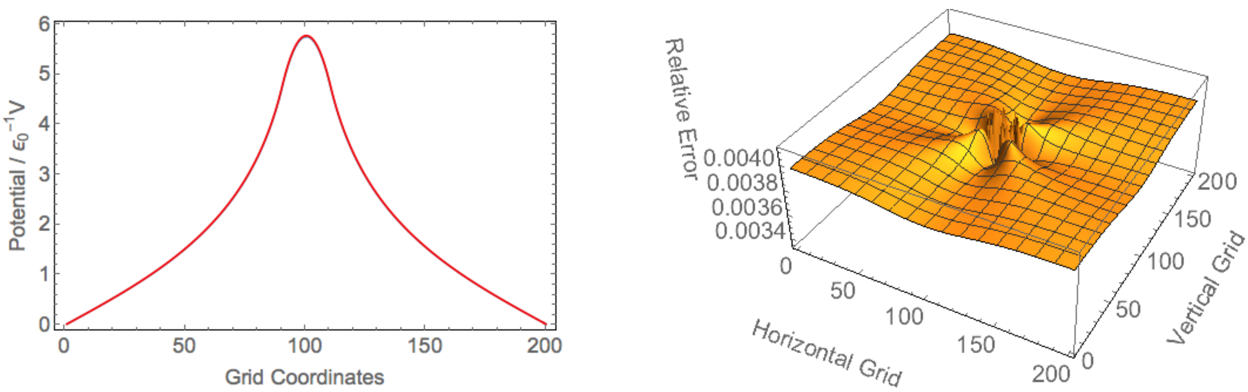

Figure A.11: FFT Poisson Solver with uniform beam compared to Mathematica solution, with small beam (a) comparison of centre line, (b) 3D plot of relative error.

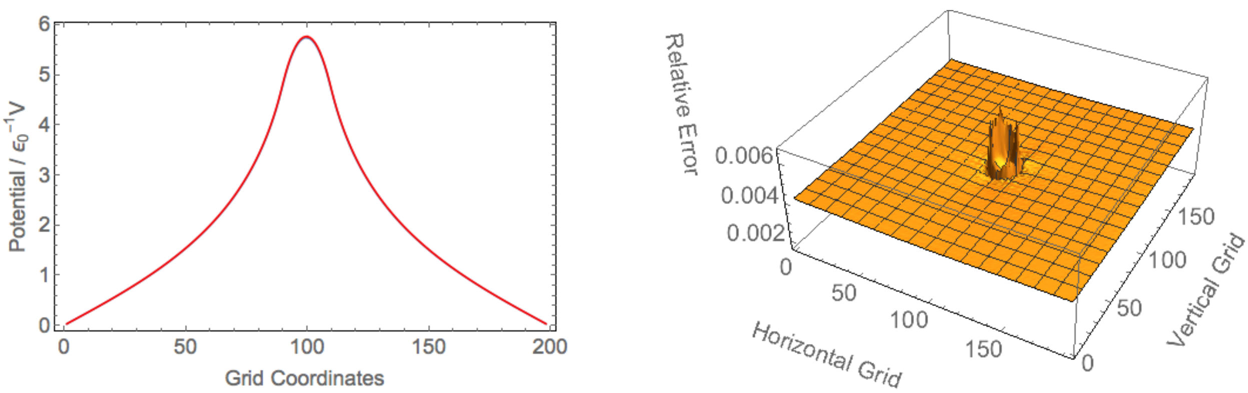

Figure A.12: FEA Poisson Solver with uniform beam compared to Mathematica solution, with small beam (a) comparison of centre line, (b) 3D plot of relative error.

Small Uniform Beam Offset by 25 mm Horizontally and Vertically

Simulation results for a 10 mm radius, uniform beam, with the beam offset by 25 mm horizontally and vertically, in an aperture of ± 100 mm in both planes are demonstrated. The charge distribution is shown in Figure A.13. The mesh is a 200 × 200 cell grid for the FFT solver, with similar resolution for the FEA solver. The resulting potential distribution is shown as a contour plot and 3D plot in Figure A.14 (a) and (b) respectively.

The error between the solvers, and an equivalent case calculated using Mathematica, is shown in Figures A.15 and A.16. Figure A.15 (a) is a comparison between the values of the two potentials along a centre line through the grid, while (b) shows the relative error as a 3D plot, with an overall accuracy greater than 0.04%. Figure A.16 shows the same values for the FEA solver, with an overall error less than 0.2%.

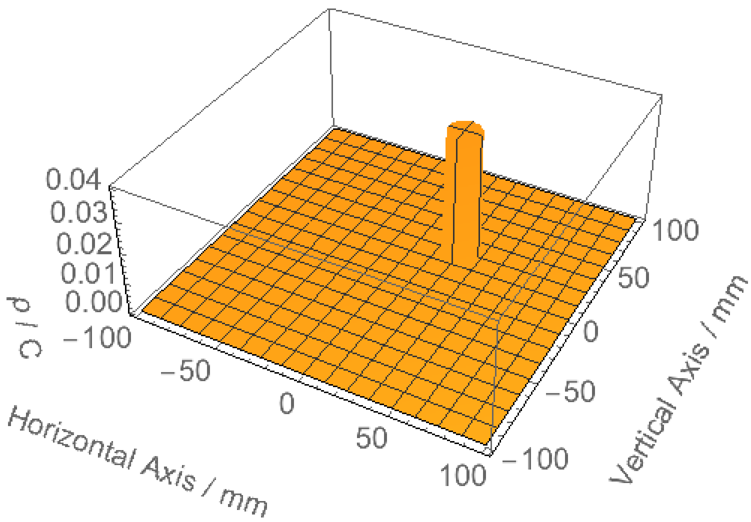

Figure A.13: Small, circular, uniform density 4π charge distribution offset by 25 mm horizontally and vertically used in Mathematica model.

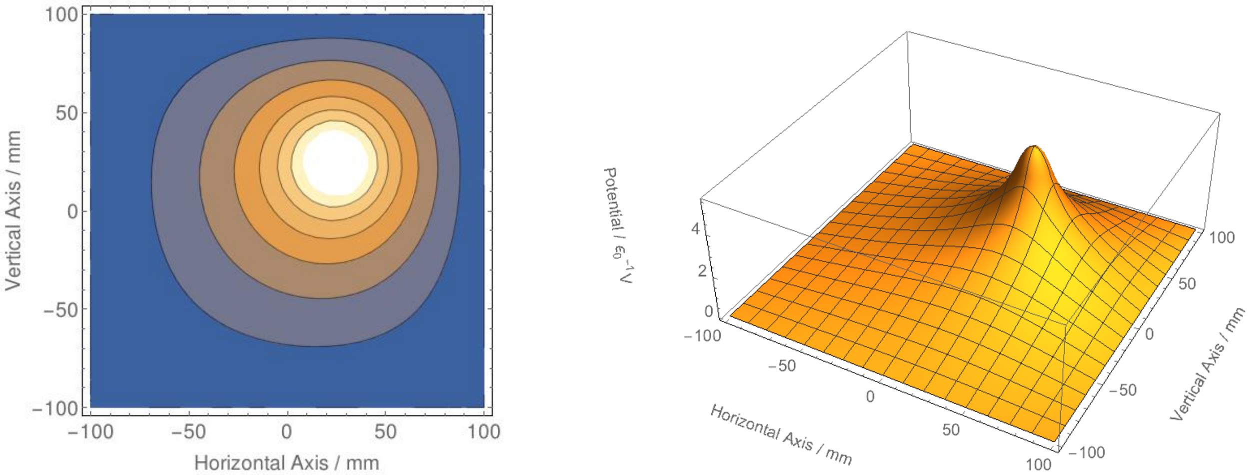

Figure A.14: Contour plot (a) and 3D plot of potential produced in Mathematica model, with small beam offset by 25 mm horizontally and vertically.

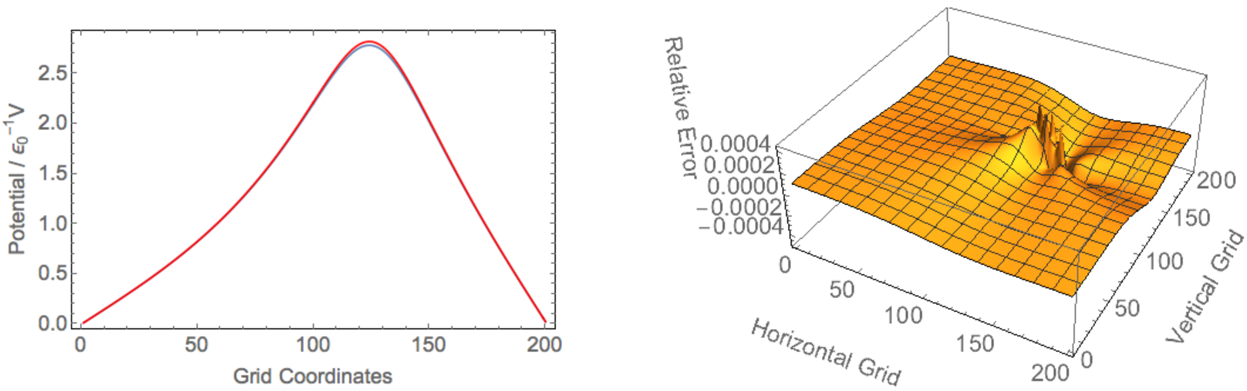

Figure A.15: FFT Poisson Solver with uniform beam compared to Mathematica solution, with small beam offset by 25 mm horizontally and vertically (a) comparison of centre line, (b) 3D plot of relative error.

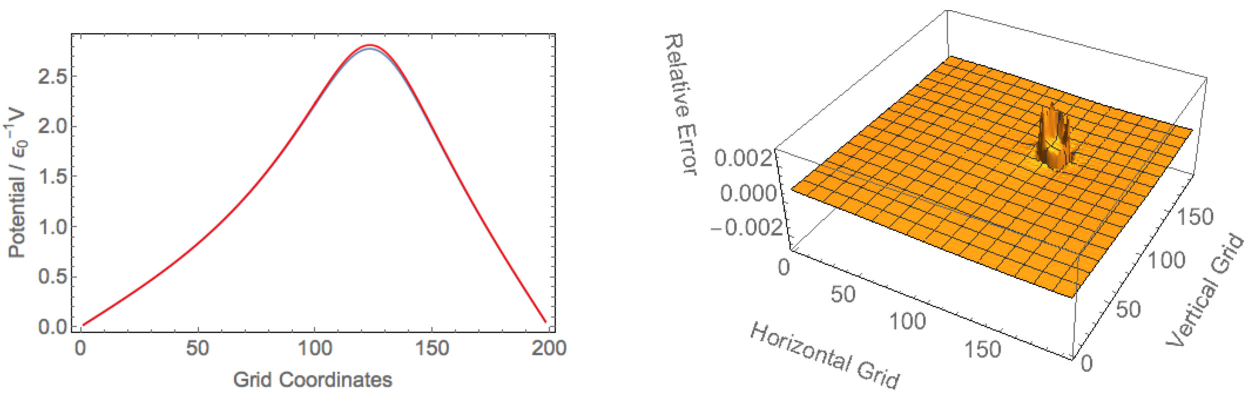

Figure A.16: FEA Poisson Solver with uniform beam compared to Mathematica solution, with small beam offset by 25 mm horizontally and vertically (a) comparison of centre line, (b) 3D plot of relative error.

Uniform Beam in a 300 by 100 Half Aperture Geometry

Simulation results for a 50 mm radius, uniform beam, in an aperture of $\pm$ 300 mm horizontally and $\pm$ 100 mm vertically are demonstrated. The charge distribution is shown in Figure A.17. The mesh is a 200×200 cell grid for the FFT solver, with similar resolution for the FEA solver. The resulting potential distribution is shown as a contour plot and 3D plot in Figure A.18 (a) and (b) respectively.

The error between the solvers, and an equivalent case calculated using Mathematica, is shown in Figures A.19 and A.20. Figure A.19 (a) is a comparison between the values of the two potentials along a centre line through the grid, while (b) shows the relative error as a 3D plot, with an overall accuracy greater than 0.02%. Figure A.20 shows the same values for the FEA solver, with an overall error less than 0.3%.

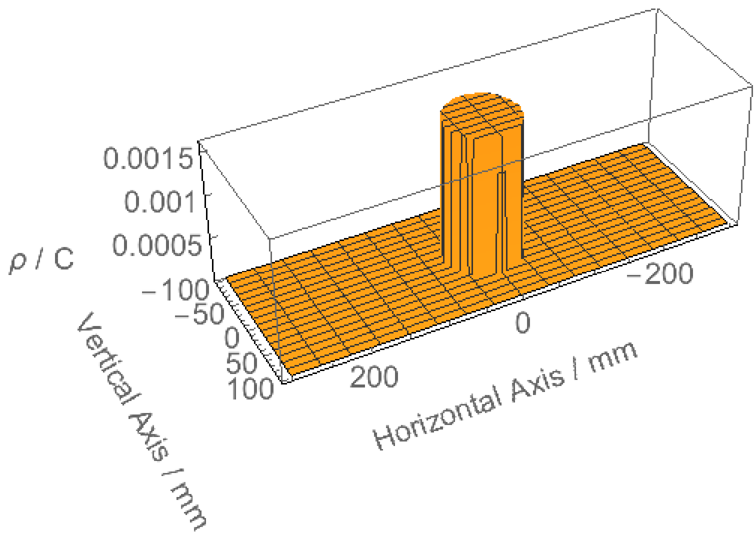

Figure A.17: Circular, uniform density 4π charge distribution in rectangular geometry used in Mathematica model.

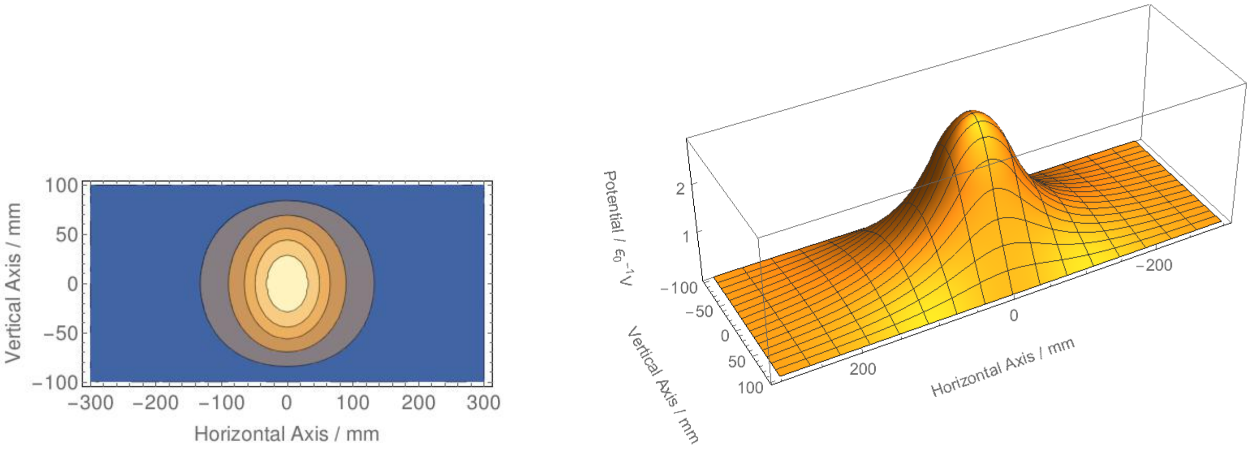

Figure A.18: Contour plot (a) and 3D plot of potential produced in Mathematica model, in rectangular geometry.

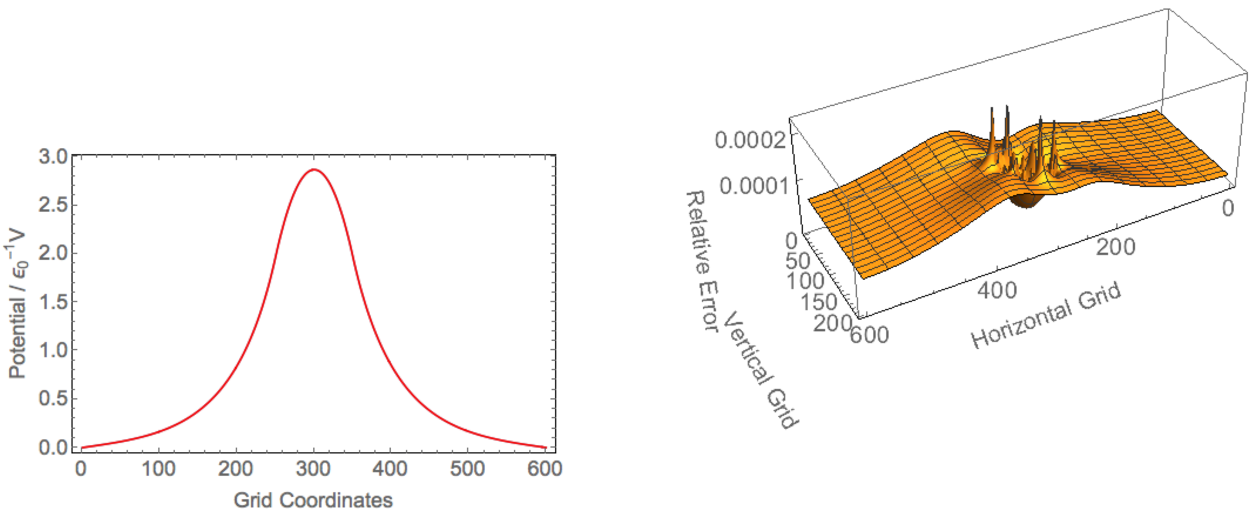

Figure A.19: FFT Poisson Solver with uniform beam compared to Mathematica solution, in rectangular geometry (a) comparison of centre line, (b) 3D plot of relative error.

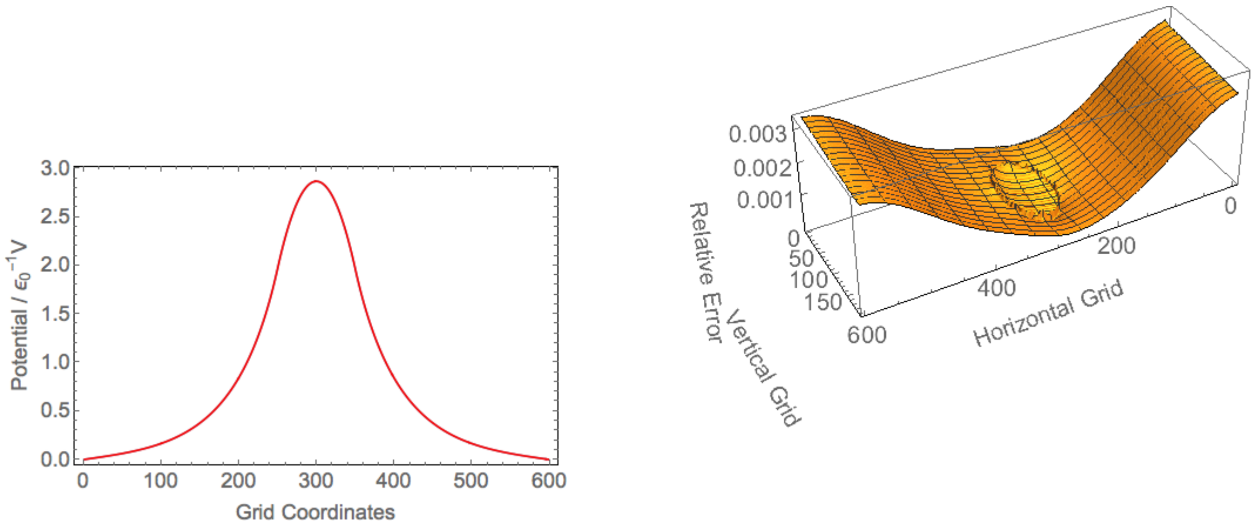

Figure A.20: FEA Poisson Solver with uniform beam compared to Mathematica solution, in rectangular geometry (a) comparison of centre line, (b) 3D plot of relative error.

Bibliography

[1] A Hofmann. "Tune Shifts From Self-Fields and Images". In "Proceedings of Cern Accelerator School", Finland (1992).

[2] `www.isis.stfc.ac.uk`.

[3] DJ Adams *et al.* "Operational Experience and Future Plans at ISIS". In "Proceedings of ICFA Advanced Beam Dynamics Workshop on High-Intensity and High-Brightness Hadron Beams", (2016).

[4] `http://neutrons.ornl.gov/facilities/SNS`.

[5] SM Cousineau. "A Fifteen Year Perspective on the Design and Performance of the SNS Accelerator". In "Proceedings of ICFA Advanced Beam Dynamics Workshop on High-Intensity and High-Brightness Hadron Beams", (2016).

[6] `http://j-parc.jp/index-e.html`.

[7] H Hotchi. "Lessons from 1-MW Proton RCS Beam Tuning". In "Proceedings of ICFA Advanced Beam Dynamics Workshop on High-Intensity and High-Brightness Hadron Beams", (2014).

[8] H Hotchi *et al.* "The Path to 1 MW: Beam Loss Control in the J-PARC 3-GeV RCS". In "Proceedings of ICFA Advanced Beam Dynamics Workshop on High-Intensity and High-Brightness Hadron Beams", (2016).

[9] `http://csns.ihep.ac.cn`.

[10] `http://europeanspallationsource.se`.

[11] `http://home.web.cern.ch`.

[12] `https://www.psi.ch/sinq/`.

[13] CR Prior. "Studies of High Intensity Proton FFAGs at RAL". In "Proceedings of ICFA Advanced Beam Dynamics Workshop on High-Intensity and High-Brightness Hadron Beams", (2016).

[14] B Boardman. "Spallation Neutron Source: Description of Accelerator and Target". Technical Report RL-82-006, Rutherford Appleton Laboratory (1982).

[15] DC Faircloth *et al.* "Understanding Extraction and Beam Transport in the ISIS Penning Surface Plasma Ion Source", *Rev. Sci. Instrum.*, **79**.

[16] AP Letchford *et al.* "Measured Performance of the ISIS RFQ". In "Proceedings of European Particle Accelerator Conference", Paris, France (2002).

[17] `http://mice.iit.edu/`.

[18] JRJ Bennett *et al.* "ESS Technical Report Volume III". Technical report, ESS Council (2002).

[19] ISK Gardner. "Ferrite Dominated Cavities". In "RF Engineering for Particle Accelerators Vol. 2", Geneva, Switzerland (1992).

[20] A Seville *et al.* "Progress on Dual Harmonic Acceleration on the ISIS Synchrotron". In "Proceedings of International Particle Accelerator Conference", Albuquerque, New Mexico, USA (2007).

[21] SA Whitehead *et al.* "Multi-Channeltron Based Profile Monitor at the ISIS Proton Synchrotron". In "Proceedings of Beam Instrumentation Workshop", (2010).

[22] CM Warsop. "Special Diagnostic Methods and Beam Loss Control on the High Intensity Proton Synchrotrons and Storage Rings". Ph.D. thesis, University of Sheffield (2002).

[23] SJ Payne. "Strip Line Monitor Design for the ISIS Proton Synchrotron using the FEA Program HFSS". In "Proceedings of International Beam Instrumentation Conference", Oxford, UK (2013).

[24] C Plostinar *et al.* "Review of Linac Upgrade Options for the ISIS Spallation Neutron Source". In "Proceedings of International Particle Accelerator Conference", Richmond, VA, USA (2015).

[25] JWG Thomason *et al.* "A 180 MeV Injection Upgrade Design for the ISIS Synchrotron". In "Proceedings of International Particle Accelerator Conference", Shanghai, China (2013).

[26] High intensity Proton Accelerator Project Team. "Accelerator Technical Design Report for High-intensity Proton Accelerator Facility Project, J-PARC". Technical Report KEK Report 2002-13, JPARC (2003).

[27] B Jones *et al.* "Progress on Designs for 180 MeV Injection into the ISIS Synchrotron". In "Proceedings of ICFA Advanced Beam Dynamics Workshop on High-Intensity and High-Brightness Hadron Beams", Lansing, MI, USA (2014).

[28] `www.cobham.com`.

[29] HV Smith *et al.* "Stripping Foil Simulations for ISIS Injection Upgrades". In "Proceedings of International Particle Accelerator Conference", San Sebastuan, Spain (2011).

[30] RE Williamson *et al.* “High Intensity Longitudinal Dynamics Studies for an ISIS Injection Upgrade”. In “Proceedings of ICFA Advanced Beam Dynamics Workshop on High-Intensity and High-Brightness Hadron Beams”, Beijing, China (2012).

[31] DJ Adams *et al.* “Ring Simulation and Beam Dynamics Studies for ISIS Upgrades 0.5 to 10 MW”. In “Proceedings of ICFA Advanced Beam Dynamics Workshop on High-Intensity and High-Brightness Hadron Beams”, Lansing, Michigan, USA (2014).

[32] JA Holmes *et al.* “ORBIT: Beam Dynamics Calculations for High Intensity Rings”. In “Proceedings of European Particle Accelerator Conference”, Paris, France (2002).

[33] RE Williamson *et al.* “Development of Physics Models of the ISIS Head-Tail Instability”. In “Proceedings of ICFA Advanced Beam Dynamics Workshop on High-Intensity and High-Brightness Hadron Beams”, (2016).

[34] `www.thalesgroup.com`.

[35] “`http://mad.web.cern.ch/mad/`”.

[36] “`www.fftw.org`”.

[37] WH Press *et al.* “Numerical Recipes in C++, Second Edition”. Cambridge University Press (2005).

[38] SY Lee. “Accelerator Physics”. World Scientific (1999).

[39] CK Birdsall & AB Langdon. “Plasma Physics Via Computer Simulation”. Institute of Physics (2005).

[40] S Humphries Jr. “Field Solutions on Computers”. CRC Press (1997).

[41] J Rossbach *et al.* “Basic Course on Accelerator Optics”. In “Proceedings of Cern Accelerator School”, Finland (1992).

[42] `www.wolfram.com`.

[43] LJ Laslett. “On the Intensity Limitations Imposed by Transverse Space Charge Effects in Circular Accelerators”. In “Proc. 1963 Summer Study on Storage Rings, Accelerators and Experimentation at Super-High Energies”, (1963).

[44] R Baartman. “Betatron Resonances with Space Charge”. In “Proceedings of Workshop in High Intensity Hadron Rings”, (1998).

[45] KY Ng. “Exact Solutions for the Longitudinal and Transverse Impedances of an Off-Centred Beam in a Rectangular Beampipe”, *Particle Accelerators*, **16**.

[46] KY Ng. “Physics of Intensity Dependent Beam Instabilities”. World Scientific (2006).

[47] GH Rees & CR Prior. “Image Effects on Crossing an Integer Resonance”, *Particle Accelerators*, **48**.

[48] `https://en.wikipedia.org/wiki/Jacobi_elliptic_functions`.

[49] E Wilson. “Transverse Beam Dynamics”. In “Proceedings of Cern Accelerator School”, (1992).

[50] C Warsop. “Hamiltonian Dynamics, Oxford Physics Lecture Notes”.

[51] IM Kapchinskij & VV Vladimirskij. “Limitations of Proton Beam Current in a Strong Focusing Linear Accelerator Associated with the Beam Space Charge”. In “Int. Conf. on High Energy Acc.”, (1958).

[52] F Sacherer. “Transverse Space Charge Effects in Circular Accelerators”. Ph.D. thesis, University of California (1968).

[53] I Hoffman. “Stability of Anisotropic Beams with Space Charge”, *Phys. Rev. E*, **57**.

[54] S Machida. “Space Charge Effects in Low-Energy Proton Synchrotrons”. In “Nuclear Instruments and Methods in Physics Research”, volume 309 (1991).

[55] BG Pine & B Jones. “Measurements of Beam Loss and Intensity against Betatron Tunes”. Technical Report IADM/MPS/1.1/12, Rutherford Appleton Laboratory (2012).

[56] CM Warsop. “Private correspondence”. ISIS Facility.

[57] S Jago. “Private correspondence”. ISIS Facility.

[58] CM Warsop *et al.* “High Intensity Studies on the ISIS Synchrotron, Including Key Factors for Upgrades and the Effects of Half Integer Resonance”. In “Proceedings of ICFA Advanced Beam Dynamics Workshop on High-Intensity and High-Brightness Hadron Beams”, (2010).

[59] RE Williamson. “Private correspondence”. ISIS Facility.

[60] CM Warsop. “Studies of Space Charge Loss Mechanisms Associated with Half Integer Resonance on the ISIS RCS”. In “Proceedings of Particle Accelerator Conference”, (2009).

[61] CM Warsop et al. “Simulation and Measurement of Half Integer Resonance in Coasting Beams in the ISIS Ring”. In “Proceedings of ICFA Advanced Beam Dynamics Workshop on High-Intensity and High-Brightness Hadron Beams”, (2012).

[62] CM Warsop *et al.* “Studies of Loss Mechanisms Associated with the Half Integer Limit on the ISIS Ring”. In “Proceedings of ICFA Advanced Beam Dynamics Workshop on High-Intensity and High-Brightness Hadron Beams”, (2014).

[63] CM Warsop *et al.* “Simple Models for Beam Loss Near the Half Integer Resonance with Space Charge”. In “Proceedings of ICFA Advanced Beam Dynamics Workshop on High-Intensity and High-Brightness Hadron Beams”, (2016).

[64] B Jones *et al.* “Progress on Beam Measurement and Control Systems for the ISIS Synchrotron”. In “Proceedings of International Particle Acclerator Conference”, (2014).